MAGNETOSTATICS AND THE MICROMAGNETICS OF IRON WHISKERS

by

Dan S. Bloomberg

B.A., University of California, Berkeley, 1967

A THESIS SUBMITTED IN PARTIAL FULFILLMENT OF

THE REQUIREMENTS FOR THE DEGREE OF

DOCTOR OF PHILOSOPHY

in the Department

of

Physics

SIMON FRASER UNIVERSITY

March 1973

APPROVAL

Name: Dan S. Bloomberg

Degree: Doctor of Philosophy

Title of Thesis: Magnetostatics and the Micromagnetics of Iron Whiskers

Examining Committee:

Chairman: K.E. Rieckhoff

A.S. Arrott
Senior Supervisor

B.L. Jones

J.C. Irwin

K.S. Viswanathan

W.F. Brown, Jr.
External Examiner
Professor of Electrical Engineering
University of Minnesota
Minneapolis, Minnesota

Date Approved: March 22, 1973

Title of Thesis/Dissertation:

"Magnetostatics and the micromagnetic theory of iron whiskers"

Author:

(signature)

Dan S. Bloomberg

(name)

April 20, 1973

(date)

ABSTRACT

The response of an iron whisker to longitudinal applied fields is studied theoretically and experimentally. Long-range magnetostatic interactions are found to play the dominant role in the magnetization process. The micromagnetic equations are solved for the transverse magnetization of the long domains in the Landau configuration and we find (i) the volume charge is always negligible for any crystalline anisotropy, (ii) the 180° wall charge depends on anisotropy and for iron never exceeds 2.3 percent of the total magnetic charge, (iii) most of the charge is on the surface and a close analogy exists between the whisker and a bar of infinite intrinsic magnetic susceptibility. This analogy is used to find the longitudinal magnetization of the whisker in an arbitrary applied magnetic field. Maxwell's equations are solved self-consistently over the length of the bar and the procedure is extended to finite intrinsic susceptibility. In addition, approximate calculations of the demagnetizing energy are used to compute the susceptibility.

In a series of experiments a whisker is used as a transformer core with various d.c. bias fields. The magnetization in a cross-section at different positions along the whisker is determined for several length to width ratios. The results are in excellent agreement with theory.

To our knowledge, this is the first time the micromagnetic equations have been solved for the magnetization in a 3-dimensional multidomain specimen in an applied field H_o. As a

result of these studies, we have been able to construct a picture of the spatial variation of magnetization in an iron whisker during the magnetization process.

We must expect posterity
to view with some asperity
    the marvels and the wonders
        we're passing on to it;
but it should change its attitude
to one of heartfelt gratitude
    when thinking of the blunders
        we didn't quite commit.

--Piet Hein

TABLE OF CONTENTS

LIST OF TABLES

LIST OF FIGURES

Figure		Page

LIST OF SYMBOLS

a	lattice constant; semi-major axis
b	semi-minor axis
c	speed of light
d	whisker width (square cross-section)
h^o	magnitude of applied differential a.c. field
h_i, h_o, h'	internal, external, and demag. differential a.c. fields
$\mathscr{h}, \mathscr{h}^L$	generalized driving field: homogeneous (3.15) and local (3.31)
ℓ	characteristic length of finite suscept. medium (6.30)
m	differential a.c. magnetization; m^2 grids in a quadrant (p.86); 2m divisions along length (p.128)
p	fraction of charge on surface
q	fraction of charge on wall
r, r_c	radius of cylinder, pickup coil
t	wall thickness (zero anisotropy) (6.17)
u	arbitrary irrotational vector
v	arbitrary solenoidal vector
w	ratio d/L of whisker
x_T	180° wall displacement at center
x_1, x_2	displacement due to bowing, tie-point motion
w_K	anisotropy energy density
w_{ex}	exchange energy density
A_c, A_p, A_s	area of calibrating coil, pick-up coil, whisker cross-section
$\vec{B}_o, \vec{B}_i, \vec{B}'$	applied, internal, demag. magnetic induction (magnetic flux density)

C	exchange constant (1.14)
$\underset{\approx}{C}$	matrix relating fields to sources
C_w, C_{ex}, C_K, C_d	wall, domain exchange (4.10b), domain anisotropy (4.13b), and demag. (4.14b) energy constants
D_b, D_m	ballistic and magnetometric demag. factors
D^{4s}, D^c, D^{ell}	ballistic demag. factors when charges are on 4 surfaces of whisker (5.16), equivalent cylinder (5.17), and ellipse (5.18)
E_d, E_d', E_d''	demag. energy of 180° wall, end spring, interaction
E_m, E_m'	magnetizing energy of 180° wall, end spring
E_T, E, E'	magnetic energy: total, 180° wall, end spring
E_c, E_c^L	demag. energy of poles on equivalent cylinder: homogeneous and local driving
E_o, E_w, E_{4s}	demag. energy: zero anisotropy, poles on wall, poles on 4 surfaces
E_1^{int}, E_2^{int}	interaction energy between charge sheets on opposite and adjacent whisker surfaces
E_a, E_{int}, E_{ex}	anisotropy energy for poles on surface; interaction energy between poles on wall and surface; exchange energy in domain (4.10a)
$\Delta E_{mag}, \Delta E_a$	increase in magnetic (4.18) and anisotropy (4.17) energy when anisotropy is turned on
F	temperature-independent exchange energy parameter
$\vec{H}_o, \vec{H}_i, \vec{H}'$	applied, internal, demag. fields (magnetic field intensity)

$\vec{H}_{loc}, \vec{H}'_{loc}$	Lorentz local field: with and without fields from external sources
$\overline{H}$	integrated strength of local driving field
H_d	departure field
$\vec{H}_K, \vec{H}_{ex}, \vec{H}_T$	anisotropy, exchange, total (effective) fields
H_A	magnitude of anisotropy field along easy axis
$\underset{\approx}{I}$	unit matrix
I,K	indexes x position of field, source points
J,L	indexes y position of field, source points
J	exchange integral
$\vec{J}_f, \vec{J}_a$	free, amperian current densities
J(z)	kernel giving field due to unit end charge
K(z,z')	kernel giving field due to unit ring charge at z'
K_x, K_y	Green functions for unit infinite line charge
K_1, K_2	anisotropy energy constants (1.12)
K_1, K_2, K_3	Spring constants (homog. driving) for 180° wall, end springs, interaction
K_1^L	spring constant (local driving) for 180° wall
L	whisker length
$\vec{M}, M_s$	magnetization vector and magnitude
$\mathcal{M}$	magnetic moment
N	number of atoms in a 180° wall
N_c	calibration coil turns
N_p	pick-up coil turns
P	demagnetizing field constant (6.28a)
$\underset{\sim}{P}$	vector relating fields to sources

Q	magnetic charge
Q_v, Q_T	volume and total charge in length Δz (6.8)
Q_e	charge on end of whisker from displacement of tie points
R	anisotropy parameter
S	spin of iron atom
T, T_c	temperature, Curie temperature
U, U_m	scalar magnetic potential, magnetization potential
U_d, U_{ex}	magnetostatic (6.13) and exchange (6.16) energies in curling pattern
W_{ex}	exchange energy between adjacent atoms
α	"stiffness" of wall (3.12)
α, β, γ	direction cosines of magnetization, referred to cubic axes
γ, γ^L	local model 180° wall demag. energy constants: homogeneous and local driving
$\gamma_w, \gamma_{2s}, \gamma_{4s}, \gamma_c, \gamma_c^L$	non-local 180° wall energy constants in homog. driving (wall, 2-surface, 4-surface, equivalent cylinder charge distributions (3.38)), local driving (3.47)
$\gamma_1, \gamma_2, \gamma_3$	non-local energy constants in homogeneous driving: 180° wall, end springs, interaction energy
δ	fraction of whisker width (used to avoid singularity)
$\varepsilon_p, \varepsilon_c$	EMF from pick-up, calibrating coils

η	end-spring energy constant (3.17)
Θ	wall angle
λ	arbitrary constant
μ_i	magnetic moment of atom i
ξ_w	Bloch wall energy/unit area
ρ	ratio cylinder diameter/length
$\rho, \rho_x(\rho_1), \rho_y(\rho_2)$	volume charge density, charge density from x and y variations of magnetization
ρ_ℓ	charge/unit length
σ	surface charge density
σ_o, σ_o^c	surface density at end of 180° wall for whisker, equivalent cylinder
σ_{end}	surface density on end of rod
$\sigma_w, \sigma_2, \sigma_3$	surface charge density on wall, two surfaces
$d\tau$	element of volume
ϕ	magnetic flux; angle of magnetization with z-axis
Φ	magnetization angle with z-axis as fraction of wall angle
Φ_x, Φ_y	ratios of x and y transverse magnetization to $M_s\Theta$
Φ_w	value of Φ_x at wall
χ, χ', χ''	intrinsic, small-coil (in-and out-phase) susceptibilities
χ_b', χ_m'	ballistic and magnetometric small-coil susceptibilities

$\chi'_w, \chi'_{2s}, \chi'_{4s}, \chi'_c$	small-coil susceptibilities for charge on wall, 2-surfaces, 4-surfaces, equivalent cylinder
χ'_{theo}	theoretical small-coil susceptibility for non-zero H_A (6.10)
ψ	angle between adjacent spins

ACKNOWLEDGMENTS

My special thanks goes to my supervisor, Professor Anthony Arrott, who recognized the important problems and supplied the time, energy, insight, and confidence needed to solve them. His unbridled enthusiasm, continually fertile imagination, and sense of humor were a great source of inspiration for me, and verified the possibility of being both a scientist and a human being.

Special thanks also goes to Dr. Bratislav Heinrich, with whom I had many hours of exciting discussions, and whose expertise in all phases of the experiment were of invaluable assistance.

I wish to thank the external examiner, Dr. W. F. Brown, Jr., for his many helpful suggestions and criticisms of the text. I also appreciate the efforts of Drs. J. C. Irwin, B. L. Jones, and K. S. Viswanathan, members of my committee, to make the thesis readable. Any remaining obscurities are due to my stubbornness alone.

I am grateful to Gilbert Lonzarich for generously supplying the whiskers, Reo Audette for writing computer plot routines, Pierre deTrey for helping with translations of journal papers, and Murray Press and Terry Templeton for many helpful discussions.

I appreciate the help of Barbara McKellar, Georgina Carlson, Jenny Clemente, and Margaret Linquist in typing the thesis. I gratefully acknowledge three years of financial support in the form of a scholarship from the NRC, and the support of the Physics Department in Teaching Assistantships, which I consider an important part of my learning experiences at Simon Fraser University.

CHAPTER 1

INTRODUCTION

1.1 The Micromagnetic Approach

One can approach ferromagnetic materials from many different levels, from the most basic (quantum mechanical) problems of the interaction of neighboring atoms to produce alignment of adjacent magnetic moments, to studies of hysteresis curves and permeability. In micromagnetics an intermediate approach is taken. A spontaneous magnetization $\vec{M}$, whose magnitude depends on temperature but not appreciably on applied field, is assumed to exist by virtue of the quantum mechanical exchange forces. Fluctuations whose wavelength is comparable to the lattice spacing are averaged out. The magnetization is taken to be continuous over the specimen and of magnitude M_s; only its direction varies. Domains may or may not be postulated, depending on the purity of approach and the questions being asked.

There are contributions to the free energy of the specimen from the magnetic energy (dipole-dipole) of magnetization, interaction with the applied field, interaction of the magnetization with the lattice (anisotropy and magnetostriction), and exchange interaction (short-range forces tending to align neighboring atomic moments). The crystal symmetry and common sense are used to find the form of the significant terms, and the material constants are extracted from experiments rather than calculated from first-principles. The magnetization is varied to minimize the total free energy.

A principal goal of this thesis is an approximate solution of the equations of micromagnetics for the case of a finite ferromagnetic body. The results of the calculation are compared to experimental results for oriented single crystals of iron, commonly referred to as whiskers.

In this chapter the micromagnetic equations are summarized, their previous uses reviewed, and their relation to the magnetization processes in iron whiskers is formulated.

1.1.1 Defining Equations and Fields

From Maxwell's equations one sees that the magnetic induction $\vec{B}$ is a solenoidal vector

$$\vec{\nabla}\cdot\vec{B} = 0, \tag{1.1a}$$

and that the sources of $\vec{B}$ are current densities $\vec{J}$:

$$\vec{\nabla} \times \vec{B} = 4\pi\frac{\vec{J}}{c} \tag{1.1b}$$

In magnetostatics there are two types of contribution to the current. One is from currents in wires or electrons in motion, and is called free currents, $\vec{J}_f$. The other type is fictitious or Amperian currents, $\vec{J}_a$, associated with a magnetic moment/unit volume in material bodies. These currents are expressed in terms of a new field which is called the magnetization $\vec{M}$:

$$\vec{\nabla} \times \vec{M} \equiv \frac{\vec{J}_a}{c} . \tag{1.2}$$

Maxwell's source equations can be rewritten as

$$\vec{\nabla} \times \vec{B} = 4\pi\frac{\vec{J}_f}{c} + 4\pi\vec{\nabla} \times \vec{M}$$

which reflects the source character of $\vec{M}$, or as

$$\vec{\nabla} \times (\vec{B} - 4\pi\vec{M}) = 4\pi\frac{\vec{J}_f}{c}$$

which reflects the field character of $\vec{M}$ and permits the definition of a new field $\vec{H}$, where

$$\vec{H} \equiv \vec{B} - 4\pi\vec{M}. \tag{1.3}$$

If one further defines a fictitious magnetic charge or "pole" density

$$\rho \equiv -\vec{\nabla}\cdot\vec{M}, \tag{1.4}$$

Maxwell's equations of magnetostatics become

$$\vec{\nabla} \times \vec{H} = 4\pi\frac{\vec{J}_f}{c} \tag{1.5}$$

$$\vec{\nabla} \cdot \vec{H} = - 4\pi\vec{\nabla}\cdot\vec{M} = 4\pi\rho . \tag{1.6}$$

In the absence of free currents

$$\vec{\nabla} \times \vec{H} = 0, \tag{1.7}$$

and one can write the magnetic field $\vec{H}$ as the gradient of a scalar potential. Because scalar potentials are usually more tractable than vector potentials, there is often a preference for discussing magnetostatics in terms of $\vec{H}$ and ρ rather than $\vec{B}$ and $\vec{J}_a$.

$\vec{H}$ is composed of two parts; the applied field $\vec{H}_o$ ($\vec{\nabla}\cdot H_o = 0$ in the region of interest) and the field from the poles, $\vec{H}'$. Similarly, $\vec{B}$ is the sum of the applied field $\vec{B}_o = \vec{H}_o$ and the field $\vec{B}'$ from the amperian currents. The poles and currents give identical "fields" outside the material ($\vec{B}' = \vec{H}'$); inside, the fields differ by $4\pi\vec{M}$.

The local field $\vec{H}_{loc}$ acting on an atom (or magnetic dipole) within the material is the Lorentz local field (Brown, Magnetostatic Principles of Ferromagnetism, p. 38 ff):

$$\vec{H}_{loc} = \vec{H}_o + \vec{H}' + \frac{4}{3}\pi\vec{M} + \vec{H}''$$

$$\equiv \vec{H}_o + \vec{H}'_{loc} , \qquad (1.8)$$

where $\vec{H}''$ is the field acting on a dipole at the center of a small sphere due to the other dipoles within it. For a cubic lattice with equal vector point magnetic dipole moments on the lattice sites, $\vec{H}'' = 0$.

1.1.2 Contributions to the Free Energy

The four major contributions to the free energy incorporate the material constants of iron. The important magnetic constants at room temperature are given in Table 1.1. For our purposes,

Table 1.1

Properties of Iron at Room Temperature

Name or Defining Equation	Symbol	Value
Saturation Magnetization	M_s	1700 gauss
Curie Temperature	T_c	1043° K
Lattice Constant	a	2.86×10^{-8} cm
Spin of Iron Atom (units of $\hbar$)	S	1
Exchange Constant	J	2.16×10^{-14} erg
$J = FM_s^2$	F	$.75 \times 10^{-20}$ cm^3
Anisotropy Field	H_A	500 gauss
Anisotropy Energy/unit volume $K = M_s H_A/2$	K	4.2×10^5 erg/cm^3
180° Wall Energy	ξ_w	1.1 erg/cm^2

all thermal fluctuations are unimportant at T = 300°K. For example, $M_s(T = 300°K) \approx .99\ M_s(T = 0°K)$. Thus, we will essentially study the magnetic properties of iron at T = 0°K.

A. Internal Magnetic Energy (Demagnetizing Energy).

We consider the magnetic material as a cubic lattice of point dipoles with moments $\vec{\mu}_i$. The interaction energy of the dipoles is

$$E_d = -\tfrac{1}{2} \sum_i \vec{\mu}_i \cdot \vec{H}'_{loc_i} = -\tfrac{1}{2}\int \vec{M} \cdot \left(\vec{H}' + \frac{4}{3}\pi \vec{M}\right) d\tau\ , \tag{1.9}$$

where $\vec{H}'_{loc_i}$ is the local field at moment i due to all the other dipoles. The fields are assumed to vary only slightly over a distance large compared to the lattice spacing but small compared to the sample dimensions. The constant term $-\frac{2}{3}\pi M_s^2$ is independent of the direction of $\vec{M}$, and can be neglected in variational calculations where only the direction of $\vec{M}$ changes. Then

$$E_d = -\tfrac{1}{2}\int \vec{M} \cdot \vec{H}'\ d\tau\ . \tag{1.10}$$

B. External Magnetic Energy (Magnetizing Energy)

In an applied field $\vec{H}_o$ there is an additional magnetic energy

$$E_m = -\sum_i \vec{\mu}_i \cdot \vec{H}_o = -\int \vec{M} \cdot \vec{H}_o\ d\tau\ . \tag{1.11}$$

C. Crystalline-Anisotropy and Magnetostrictive Energies

By symmetry, the anisotropy energy/unit volume to lowest order in a cubic crystal is

$$w_K = K_1(\alpha^2\beta^2 + \alpha^2\gamma^2 + \beta^2\gamma^2) + K_2\alpha^2\beta^2\gamma^2 \tag{1.12}$$

where (α, β, γ) are direction cosines of the magnetization, referred to the cubic axes:

$$\vec{M} = M_s\hat{M} = M_s(\alpha\hat{x} + \beta\hat{y} + \gamma\hat{z}). \tag{1.13}$$

In an unstressed crystal there is a strain on the lattice due to the magnetization itself. This gives a term of the same form as the crystalline anisotropy and is included there. With the exception of the closure domains (Sec. 4.2) and diamond domains (Sec. 6.1.2), we need not be concerned with magnetostriction.

D. Exchange Energy

For a non-uniform magnetization the contribution to the energy/unit volume from atomic forces which align neighboring spins is

$$w_{ex} = \tfrac{1}{2}\, C\left[(\vec{\nabla}\alpha)^2 + (\vec{\nabla}\beta)^2 + (\vec{\nabla}\gamma)^2\right]. \tag{1.14}$$

1.1.3 The Micromagnetic Equations

The total energy is minimized with respect to variations in the magnetization (Brown, Micromagnetics, Ch. 4) and the result is that $\vec{M}$ satisfies

$$\vec{M} \times \vec{H}_T = 0 \tag{1.15}$$

everywhere within the material, where

$$\vec{H}_T = \vec{H}_o + \vec{H}' + \vec{H}_k + \vec{H}_{ex} ,$$

$$\vec{H}_k = - \frac{\partial w_K}{\partial \vec{M}} ,$$

$$\vec{H}_{ex} = \frac{C}{M_s^2} \nabla^2 \vec{M} ,$$

and

$$\frac{\partial}{\partial \vec{M}} = \frac{1}{M_s} \frac{\partial}{\partial \hat{M}} = \frac{1}{M_s} \left(\frac{\partial}{\partial \alpha} \hat{x} + \frac{\partial}{\partial \beta} \hat{y} + \frac{\partial}{\partial \gamma} \hat{z} \right).$$

The meaning of (1.15) is that if there is a torque on $\vec{M}$ due to the effective field $\vec{H}_T$, $\vec{M}$ will rotate (usually changing $\vec{H}_T$ in the process) until the torque is zero everywhere. The "field" $\vec{H}_T$ is indeterminate by a vector $\lambda\vec{M}$ (λ any constant), since $\vec{M}\times\vec{M} = 0$. This is the reason the Lorentz local field correction $\frac{4}{3}\pi \vec{M}$ causes no problems, and the convenient choice of $\vec{H}'$ (rather than $\vec{B}' = \vec{H}' + 4\pi\vec{M}$) is sufficient for the dipole-dipole fields.

To solve (1.15) it is necessary to attack the potential problem contained therein:

$$\vec{H}' = -\vec{\nabla}U,$$

where U satisfies

$$\nabla^2 U = \begin{cases} 4\pi\vec{\nabla}\cdot\vec{M} & \text{inside} \\ 0 & \text{outside} \quad (\text{large } r,\ U \sim \frac{1}{r^2}), \end{cases} \qquad (1.16)$$

and on the surface U is continuous with a discontinuity in its normal derivative equal to $4\pi\vec{M}\cdot\hat{n}$. And in this lies the basic difficulty.

1.2 Previous Use of the Micromagnetic Equations

The history of micromagnetics prior to 1963 is covered in Brown's monograph (Micromagnetics, 1963) and in reviews by Shtrikman and Treves (Sh-63R) and Aharoni (Ah-62R). Advances in the last ten years are summarized in 3 review articles of Aharoni (Ah-66R, Ah-71aR, Ah-71bR). Domain theory is reviewed by Kittel (Ki-49) and Kittel and Galt (Ki-56). I want to give here only a brief outline of previous applications of the micromagnetic equations.

These equations were written down in 1940 by Brown (Br-40) and first applied in the linearized regime near saturation. Applications of micromagnetics have been to the properties of both fine-particle (single-domain) ferromagnets and of larger (bulk or thin film) specimens which are not necessarily single-domain.

For fine particles, the basic problem is the establishment of existence conditions for single domains (Br-68, Br-69): for what sizes and internal parameters is a (nearly) uniform magnetization more stable than a highly non-uniform one. For very small particles the exchange and anisotropy energies associated with a highly non-uniform magnetization would be greater than the demagnetizing energy of a uniform magnetization, and the particle is single-domain (Br-60). Micromagnetics is used to determine the response of single-domain particles to applied fields. An attempt is made to explain both the mode of magnetization reversal and the resulting hysteresis curve (St-48, Ah-59). Hysteresis in those real materials composed of collections of fine particles is complicated due to magnetic (dipole-dipole) interactions between different particles, and only highly simplified models have been used (Ne-47, Ah-59).

For a large enough particle the magnetostatic energy, which scales with the volume if the relative dimensions are unchanged, forces a non-uniform magnetization pattern which avoids surface and volume poles. This is generally called a curling pattern. With a finite crystalline anisotropy, the magnetization in any region tends to point along one of the easy directions in the crystal. Regions of rather uniform magnetization ("domains") result and the boundaries between them sharpen into thin "walls" (Br-59R).

For large crystals micromagnetic calculations have been used to describe the structure of the walls between domains and nucleation of deviations from uniform magnetization in the presence of a reversed internal magnetic field. These calculations have all been essentially one or two dimensional. The existence of domains has not been shown rigorously from the micromagnetic equations, although plausibility arguments can be made (Br-70R). In wall calculations, the domains (or similar boundary conditions) are assumed to exist. The classic calculations for bulk crystals are one-dimensional (La-35), whereas the best calculations for thin films are 2-dimensional (La-69, Ah-67a, Ah-72, Hu-69, Hu-70). In the nucleation field applications, the specimen is either an ellipsoid of revolution, a cylinder (Br-57, Fr-57) or prism (Br-62, Br-64) infinite in one dimension, or a thin plate (Br-61, Mu-67, Fo-68, Ah-68). It is initially uniformly magnetized in a high applied field which is then decreased. An instability develops and the initial mode of reversal can be studied. In the simplest cases (e.g. infinite cylinder) the uniform magnetization does not give rise to a demagnetizing field, and it is shown (Ah-58, Br-59) that only a uniform magnetization is stable. The magnetization reverses direction irreversibly without the formation of stable (multi-domain) states. In a finite specimen domains are presumably formed. However, this has never been shown micromagnetically because the equations are non-linear and the magnetization cannot be tracked beyond the initial instability.

1.3 Micromagnetics of Iron Whiskers

The non-linear equations of micromagnetics admit many solutions. This makes possible the phenomenon of hysteresis. These equations are so complicated that there is no calculation, to date, for a specimen of any geometry in which a domain structure is formed, without artificial constraints (e.g. St-69) and starting from either a random or uniform initial magnetization. Further, to our knowledge the micromagnetic equations have not been solved for the magnetization within a postulated domain for any 3-dimensional multi-domain specimen in an applied field $\vec{H}_o$*. This problem is solved here for the long domains in an iron whisker of square cross-section d^2 in the Landau configuration (Fig.1.1). We consider long whiskers where $d/L \ll 1$ and where d is much larger than the theoretical wall width ($\sim 10^{-6}$ cm.).

In the absence of an applied field, we assume for simplicity that the magnetization is in the Landau structure. Certainly the whisker will have a domain configuration similar to this. The closure domains are necessary to prevent a large magnetostatic energy due to free poles. A simple calculation of wall and magnetostrictive energies predicts that one 180° wall will be lower in energy than two or more, for crystals of width

---

*The magnetization is found trivially for the picture-frame specimen (Wi-49), which is essentially two-dimensional and has no demagnetizing energy. Without imperfections (and neglecting the change in length of the 180° walls), it would have infinite measured susceptibility. Reversal of $\vec{M}$ would occur as in an infinite square ferromagnetic prism (Br-64), and no domains could exist.

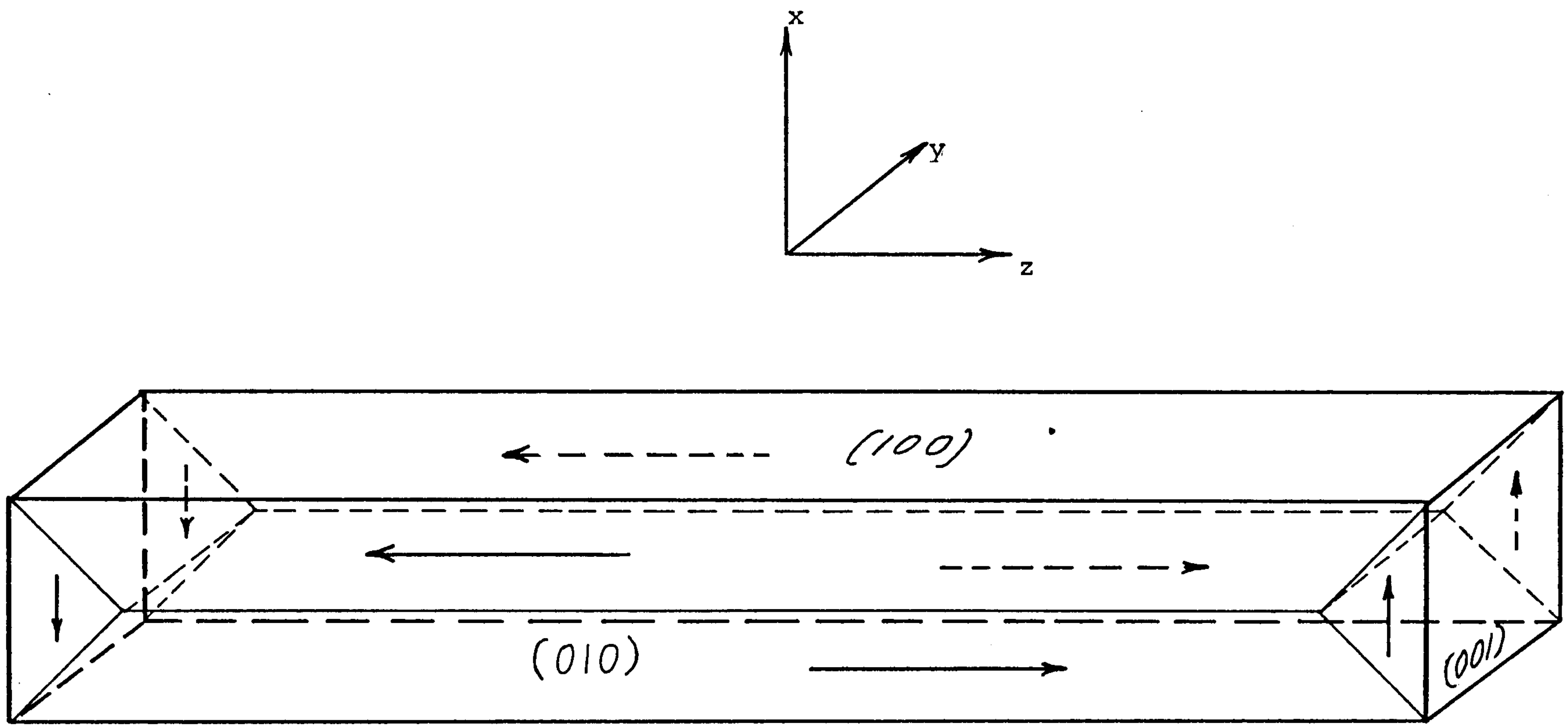

Fig. 1.1. Landau configuration for magnetization in oriented iron whisker in zero applied field. Actual whiskers have a much larger length/width ratio. The magnetization direction at the front surface is indicated by solid arrows, and at the rear surface by dotted arrows. There are two long and two short domains, and within each the magnetization is uniform.

$d \lesssim 700\mu$. In fact, domain patterns observed on iron whiskers (Co-57, Co-58) all showed only one 180° wall.

We now apply a longitudinal field $H_o\hat{z}$. The wall energy is negligible compared to anisotropy and magnetostatic energies, so the change in the wall energy, due to increase in length, can be easily ignored (Sec. 4.2.1). We assume (to be verified later) the magnetization changes slowly enough within the domains that the exchange energy can be neglected there, and we solve for $\vec{M}$ within the domains by micromagnetics. That is, we consider the anisotropy energy, magnetizing energy (interaction of the whisker magnetization with the external field), and the demagnetizing energy (self-energy of the poles), and find $\vec{M}(\vec{r})$ which minimizes the total energy.

In the long domains we expect the magnetization to be nearly uniform, so α, $\beta << 1$. Then $\gamma \cong 1 - \frac{1}{2}(\alpha^2 + \beta^2)$, because $\vec{M} \cdot \vec{M} = M_s^2$. The anisotropy energy is then

$$w_K \cong K_1(\alpha^2 + \beta^2)$$

where the terms in $\alpha^2\beta^2$ are neglected. This leads to

$$\vec{H}_K \cong - H_A(\alpha\hat{x} + \beta\hat{y}) \qquad (1.17)$$

where $H_A = \frac{2K_1}{M_s}$.

The anisotropy energy can equivalently be written $w_K = K_1(1-\gamma^2)$, which leads to

$$\vec{H}_K = H_A \gamma \hat{z} \simeq H_A \hat{z} \ . \tag{1.18}$$

This differs from the previous expression (1.17) by $\lambda\vec{M}$, where $\lambda = \frac{H_A}{M_s}$, so it exerts the same torque.

For α, β << 1, $\vec{M} \times \vec{H}_T = 0$ is linearized to

$$\left(H_T\right)_x = \alpha \left(H_T\right)_z$$

$$\left(H_T\right)_y = \beta \left(H_T\right)_z \ .$$

Using (1.18) for $\vec{H}_K$,

$$(H_o + H_z' + H_A)\ \alpha = H_x' = -\frac{\partial U}{\partial x}$$

$$(H_o + H_z' + H_A)\ \beta = H_y' = -\frac{\partial U}{\partial y} \ . \tag{1.19}$$

Because α, β << 1, they are nearly equal to the respective angles of $\vec{M}$ with the z-axis, and (1.19) can be represented vectorially :

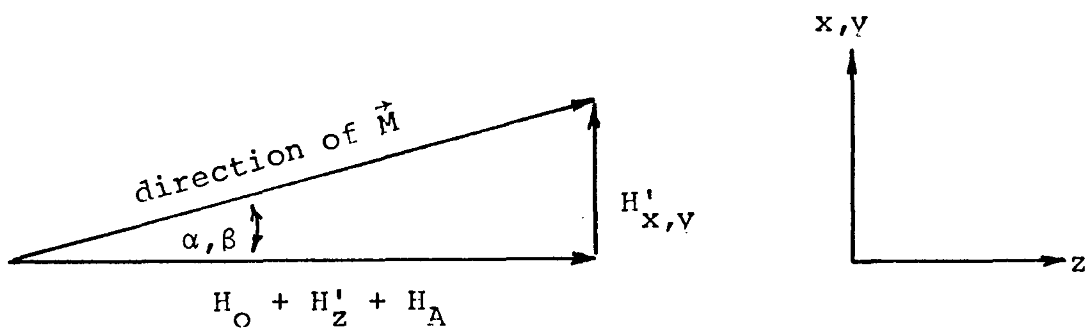

Using (1.17) for H_K,

$$(H_o + H_z') \alpha = H_x' - \alpha H_A$$

$$(H_o + H_z') \beta = H_y' - \beta H_A . \tag{1.20}$$

It is clear that (1.19) and (1.20) are identical.

These equations will be solved numerically in Chapter 4 for the transverse magnetization (given by α, β) throughout a cross-section of the whisker. In Chapter 6 they will be used to show that the volume charge is completely negligible.

1.4 Outline of the Thesis

In Chapter 2 an experiment is described that has been performed to measure the longitudinal magnetization of the whisker in response to both uniform and localized a.c. magnetic fields, in the presence of a uniform d.c. magnetic field. A model is presented in Chapter 3 to account for the observed magnetization by treating the long-range dipole fields locally, and is refined by a quantitative treatment of the demagnetizing energy. In Chapter 4 the transverse magnetization in the whisker is found by expressing the demagnetizing fields in integral form and evaluating the self-consistency conditions numerically as a set of simultaneous linear equations. In this way, no iteration is necessary. The longitudinal magnetization is found numerically in Chapter 5 for different applied fields by treating the whisker as a linear medium of infinite susceptibility and solving Maxwell's equations for the cylindrical boundary conditions. For purposes of general interest (such as above T_c) solutions for finite susceptibility are also given. We discuss iron single crystals more generally in Chapter 6, and Chapter 7 is a short summary of our results.

CHAPTER 2

MEASUREMENT OF MAGNETIZATION

Iron whiskers grown in the [100] direction are ideal for interpreting the results of magnetic measurements. They are perfect single crystals (except for a dislocation line down the center) and can be grown with square cross-section and negligible taper. They can be cleaved transversely without damage, permitting experiments on portions of the same whisker with different length/width ratios. Good specimens are observed (Co-57, Co-58, Sc-57, De-58a,b) to have simple domain structures, such as the type predicted by Landau and Lifshitz (La-35).

Some whiskers have been observed (Ha-70, Ar-71, He-72) to have a very simple magnetization curve. When the measured magnetization is an average in the cross-section at the center of the whisker, the M vs. H curve is linear until saturation is approached, when it flattens rapidly. When the sample is in the Landau configuration, the curve is linear and reversible. Hysteresis is only found near the transition from linear to saturated response. This transition was interpreted (He-72, Ar-71) as occurring at the departure field H_d, when the freely-bowing 180° wall touches the surface.

In the experiments to be described here, the whisker was situated in a longitudinal d.c. bias field of variable strength. In addition, a small longitudinal low-frequency a.c. field was applied in two ways: either homogeneously or highly localized (~ .5 mm) at the center of the whisker. By low frequency, we mean that the out-phase response (due to eddy current damping) is much less than the in-phase susceptibility. We used frequencies from 500 to 2500 Hz where the damping is negligible. The susceptibility measured was then essentially the d.c. response of the magnetization. All measurements were taken at room temperature.

2.1 Apparatus

Two "boats" of whiskers were obtained from Mr. Gilbert Lonzarich at the University of British Columbia. The whiskers are grown by placing $FeCl_2$ crystals in a pure iron trough and heating to 720°C for about 15 hours. Hydrogen gas is passed through, reducing the iron to a Fe° vapor which condenses into long single crystals with a screw dislocation down the center. Suitable crystals must have a minimum of impurities, be square in cross-section, and have no taper. The whisker selected was originally 14.68 mm × .14 mm × .14 mm, with a taper of less than .01 mm along its length. From experiments on similar whiskers, Lonzarich concludes that the residual resistivity ratio was probably greater than 1000, which indicates rather high purity.

The whisker was placed in a (fine) quartz capillary tube (o.d. ~ .3 mm), which was epoxy cemented to a lucite cube (~ 5 mm on a side) mounted on a thin lucite plate. Different specimen holders were used for each type of driving. For homogeneous driving (by an electromagnet), a 10-turn pick-up coil was wound around the tube and the leads were twisted and cemented to the plate before being attached to a BNC connector one cm. away. For local driving an additional 2-turn driving coil was placed around the center of the whisker. The leads were connected to another BNC, also mounted on the plate, and an 11-turn pick-up coil was used.

The plate was mounted with nylon screws on the flattened end of a lucite rod. The other end of the rod was put in a clamp mounted on a two-way micrometer traverse, placing the whisker between the pole-faces of an electromagnet with its axis perpendicular to them. The pole-faces were 10 cm. in diameter and the gap was 3.6 cm., providing a quite homogeneous field. The specimen was illuminated from below and observed from above through a Wild binocular microscope. Using cross-hairs in one eyepiece and the scale on the micrometer, the position of the pick-up coil along the whisker could be measured to within .01 mm.

A Kepco bipolar power supply was used to facilitate continuous field reversals. For homogeneous driving, an a.c. field was also produced in the electromagnet by amplification through the power supply of the signal from a Hewlett-Packard 200CD signal generator. The a.c. signal from the pick-up coil was amplified by a PAR Model 124 lock-in amplifier with digital readout. For local driving the a.c. field was produced directly by the signal generator, with a 1200 Ω resistor in series with the 2-turn driving coil (see Fig. 2.1).

There was always a background signal from the direct linkage of the pick-up coil by the applied a.c. field. This background was found by nearly saturating the whisker with a large d.c. bias field ($\sim$ 500 gauss). The phase was adjusted at the same time, because the background signal was in phase with the applied field.

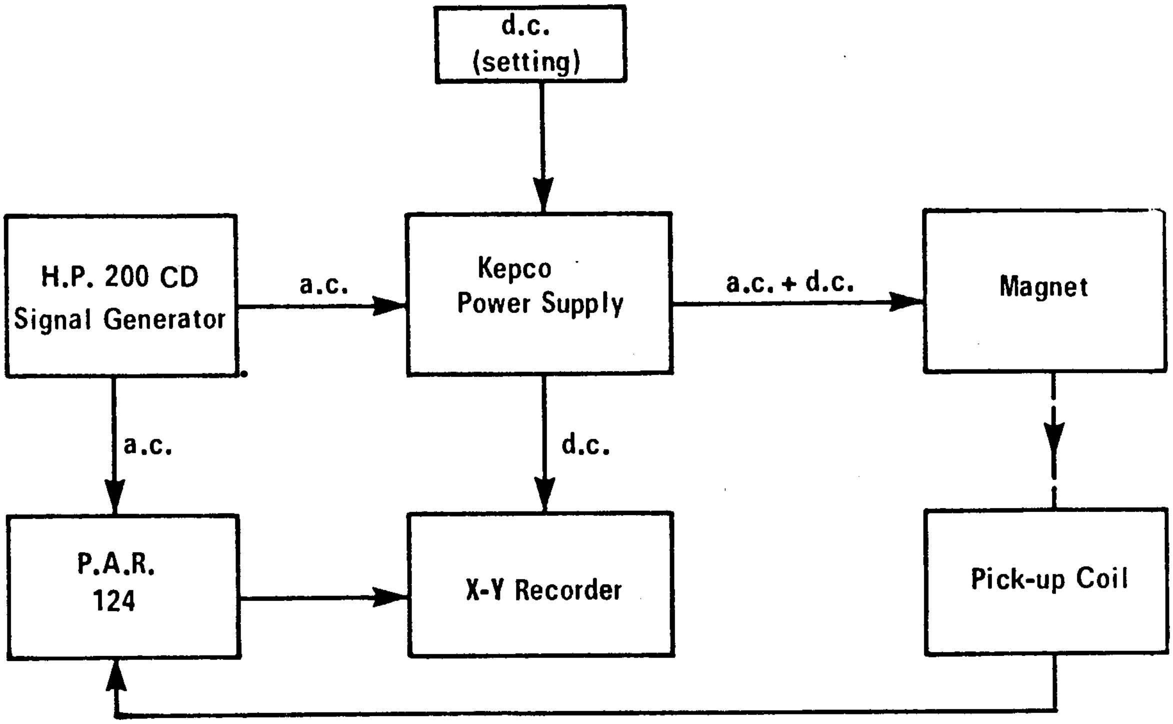

(a)

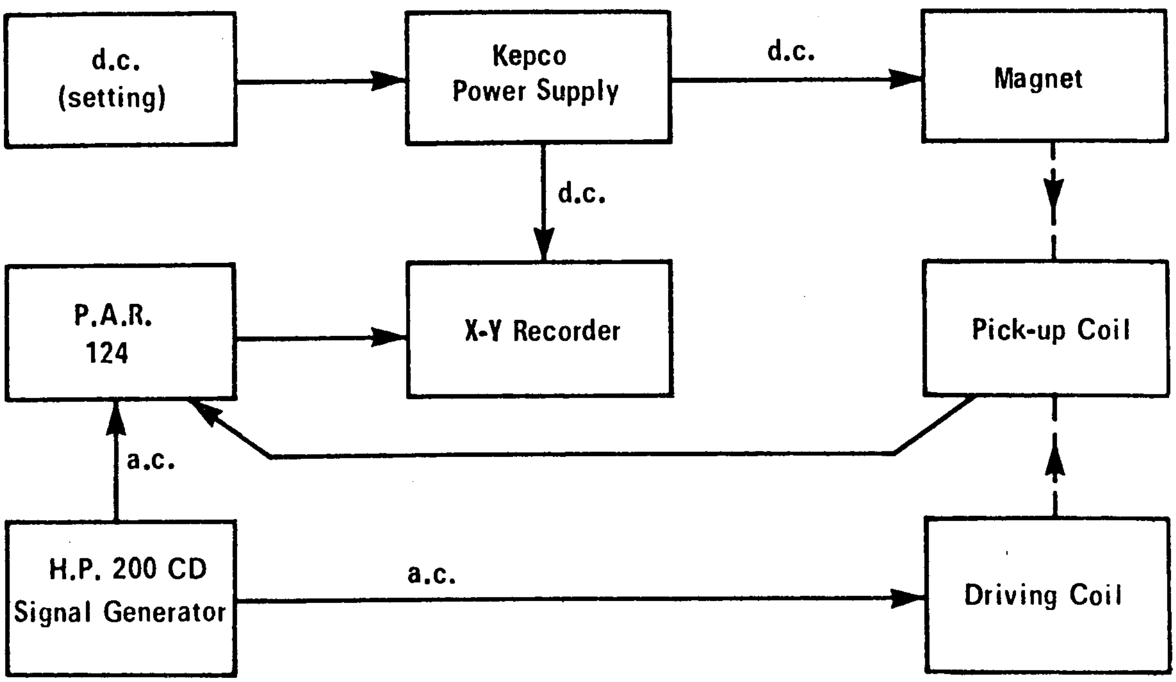

(b)

Fig. 2.1. Circuits for susceptibility measurements in (a) homogeneous driving and (b) local driving fields.

2.2 Interpretation of the Measured Voltages

We apply an arbitrarily small spatially homogeneous a.c. driving field $h^o e^{i\omega t}$ (small letters will be used to denote differential quantities). Our "measured" flux will be the difference in pick-up coil voltage when the sample is present (large susceptibility) and absent (zero susceptibility). The latter (background flux) is conveniently measured by saturating the whisker. We ask how the measured flux is related to the average magnetization in the cross-section of whisker at the pick-up coil.

Let the area of a very short N_p turn pick-up coil be A_p and the whisker cross-section be $A_s = d^2$. Brackets < > will be used throughout to denote an average over the whisker cross-section. The amplitude of the measured in-phase voltage is

$$|\varepsilon_p| = \frac{1}{c}\frac{\partial\phi}{\partial t}\Big|_{\substack{\text{large}\\ \text{susceptiblity}}} - \frac{1}{c}\frac{\partial\phi}{\partial t}\Big|_{\text{saturated}}$$

$$= \frac{\omega}{c} N_p \left[(\langle h_i\rangle + 4\pi\langle m\rangle)A_s + \int_{A_p - A_s} h_o dA - h^o A_p\right]. \tag{2.1}$$

The only important field components here are longitudinal, parallel to the long axis of the whisker. Here h_i is the internal field, h_o is the field outside the whisker ($h_i = h_o$ at the surface), $\langle m\rangle$ is the change in magnetization (due to motion of the walls) averaged over the cross-section, and the integral is over the area inside the pick-up coil but outside the whisker. The magnitude of the demagnetizing field h' is defined from

$$h_i \equiv h^o + h', \quad h' < 0, \tag{2.2}$$

where h' is nearly uniform within the whisker cross-section and near the whisker (out to a distance still much less than L, the whisker length). h' is taken as positive in the direction from positive to negative poles. We define the intrinsic and measured susceptibilities, χ and χ', by

$$\langle m\rangle \equiv \chi\langle h_i\rangle \equiv \chi' h^o , \tag{2.3}$$

and the position-dependent demagnetizing factor D by

$$\langle h'\rangle \equiv -4\pi D\langle m\rangle. \tag{2.4}$$

Equations (2.2), (2.3), and (2.4) give the useful relation

$$\frac{1}{\chi'} - \frac{1}{\chi} = 4\pi D . \tag{2.5}$$

We will show in Chapter 5 that $\chi \gg \chi'$ when the walls are highly mobile (far from saturation), and only the whisker shape determines the response:

$$\frac{1}{\chi'} = 4\pi D . \tag{2.6}$$

Then $h_i \cong 0$, and

$$h' \cong -h^o . \tag{2.7}$$

For a close-wound pick-up coil, $h_o = h_i = 0$ within the winding.

Then (2.1) becomes

$$\varepsilon_p = \frac{\omega N_p}{c}\left[4\pi\chi' A_s - A_p\right]h^o$$

$$= \frac{\omega N_p}{c}\left[\frac{A_s}{D} - A_p\right]h^o. \qquad (2.8)$$

Neglect of the second term is justified if

$$\frac{A_p}{4\pi\chi' A_s} << 1 .$$

In this experiment it gives an error of about 1 to 3 percent, depending on the whisker length, and we ignore it.

In summary, we find that for sufficiently high intrinsic susceptibility and for a long whisker with a tightly-wound pick-up coil, h' cancels h^o within the coil, and no subtraction of background should be made. In the experiment, we had an additional, larger component of the background from flux linking the pick-up coil leads where they attached to the BNC, and subtraction of this was necessary. In principle the background flux could have been measured by reversing the direction of the coil with respect to the lead wires. As this was inconvenient and the error was small this was not done.

For homogeneous driving, an absolute calibration of the signal was made. The signal from an N_c (=50) turn, 2.2 mm diameter calibrating coil placed in a field $h^o\ e^{i\omega t}$ is

$$\varepsilon_c = \frac{\omega}{c} N_c A_c h^o, \qquad (2.9)$$

where $A_c = 3.8\ mm^2$ is the area of the calibrating coil. From (2.4, 2.7, 2.8), the signal from the whisker is

$$\varepsilon_p \cong 4\pi N_p \frac{\omega}{c} \langle m \rangle d^2, \tag{2.10}$$

and the measured susceptibility is

$$\chi' = \frac{\langle m \rangle}{h^o} = \frac{\varepsilon_p}{\varepsilon_c} \frac{N_c A_c}{4\pi N_p d^2} \quad . \tag{2.11}$$

It is not necessary to know either the frequency or the magnitude of the small a.c. field. For the low frequencies used, the magnetization is in phase with h^o.

The largest experimental uncertainty in this susceptibility comes from the measurement of d, which is known within about 5 percent. However, the quantity $\chi' d^2$ can be determined much more accurately from experiment (2.11) and this is the quantity calculated from theories of Chapters 3 and 5. We will find it more convenient to compare the dimensionless quantities χ' and $\chi' \frac{d}{L}$, but it should be kept in mind that the uncertainty in d will not appreciably affect these comparisons.

2.3 Experimental Results

2.3.1 Homogeneous Driving

The whisker was cut successively from the same end to five different lengths and the following quantities were measured for each length:

i) The departure field H_d

ii) The magnitude of χ' at the center

iii) The magnetization process: relative values of $\chi'(H_o)$ and $\chi''(H_o)$, the out-phase component

iv) $\chi'(z)$, or equivalently $M(z)$.

Figs. 2.2a and 2.2b show typical curves for χ' and χ'' vs. H_o, when the pick-up coil is at $z = 0$ (center of the whisker) and at $z = .3\left(\frac{L}{2}\right)$ respectively. Similar curves for a more perfect whisker are discussed in (Ar-71, He-72). χ'' depends on the number, size, and position of the moving walls. In general, the eddy current damping is reduced when the walls are large in area and near the surfaces.

The magnetization process can be followed by considering χ'' in Fig. 2.2a. Start at (1) with the whisker nearly saturated in a reversed field. Between (2) and (3) it is possible that nucleation occurs of a Coleman-type structure (Co-58) with perhaps two parallel (110) walls. As the field is increased through zero to (4), the walls become larger and move toward each other, decreasing χ''. At (4) there is an abrupt change to the Landau structure, which

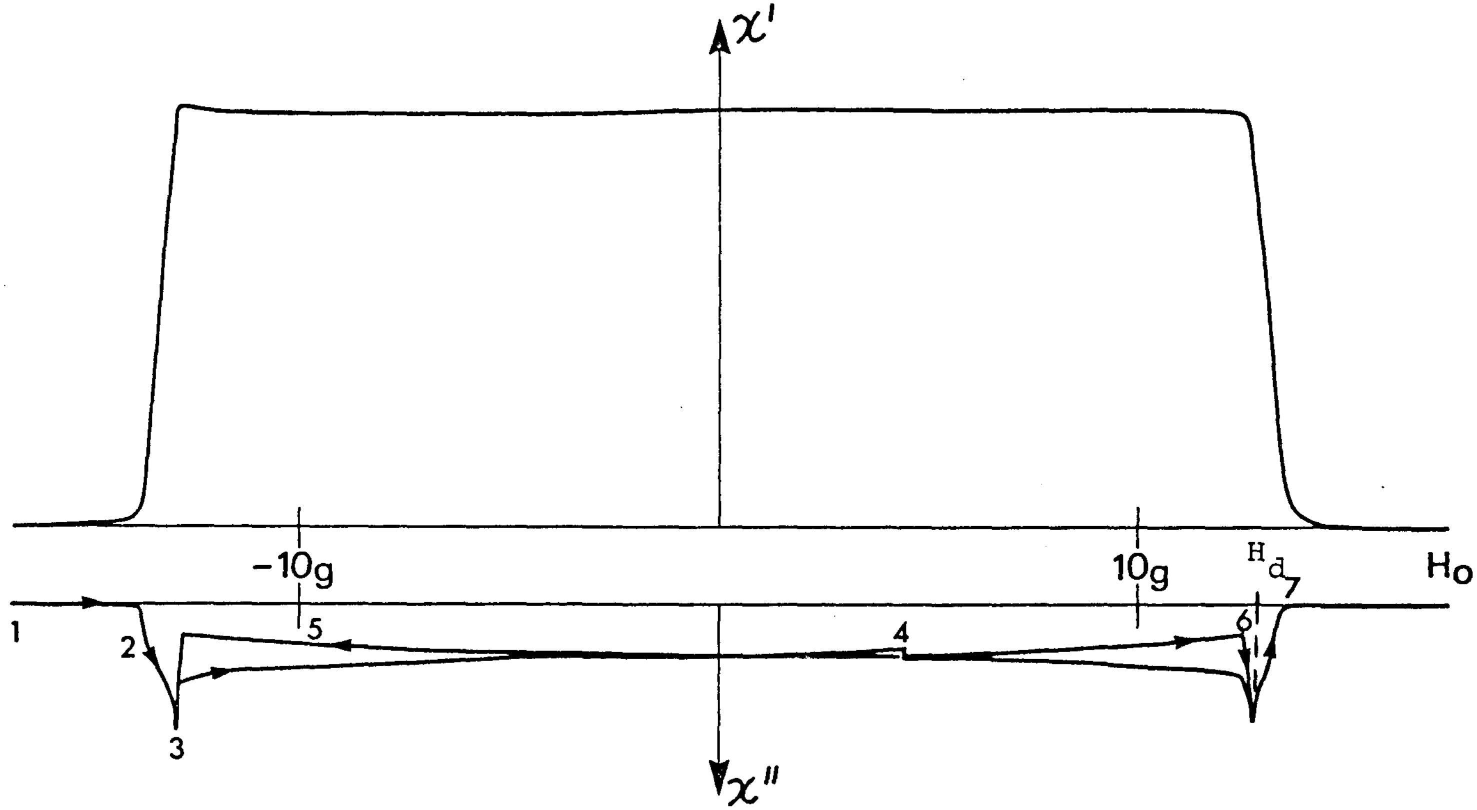

Fig. 2.2a. In- and out-phase differential susceptibility in homogeneous applied field. L=1.047 cm., d/L=.0139, H_d=12.9 gauss, ν=500 Hz. Pick-up coil is at center (z=0), showing rapid saturation after $H_o > H_d$.

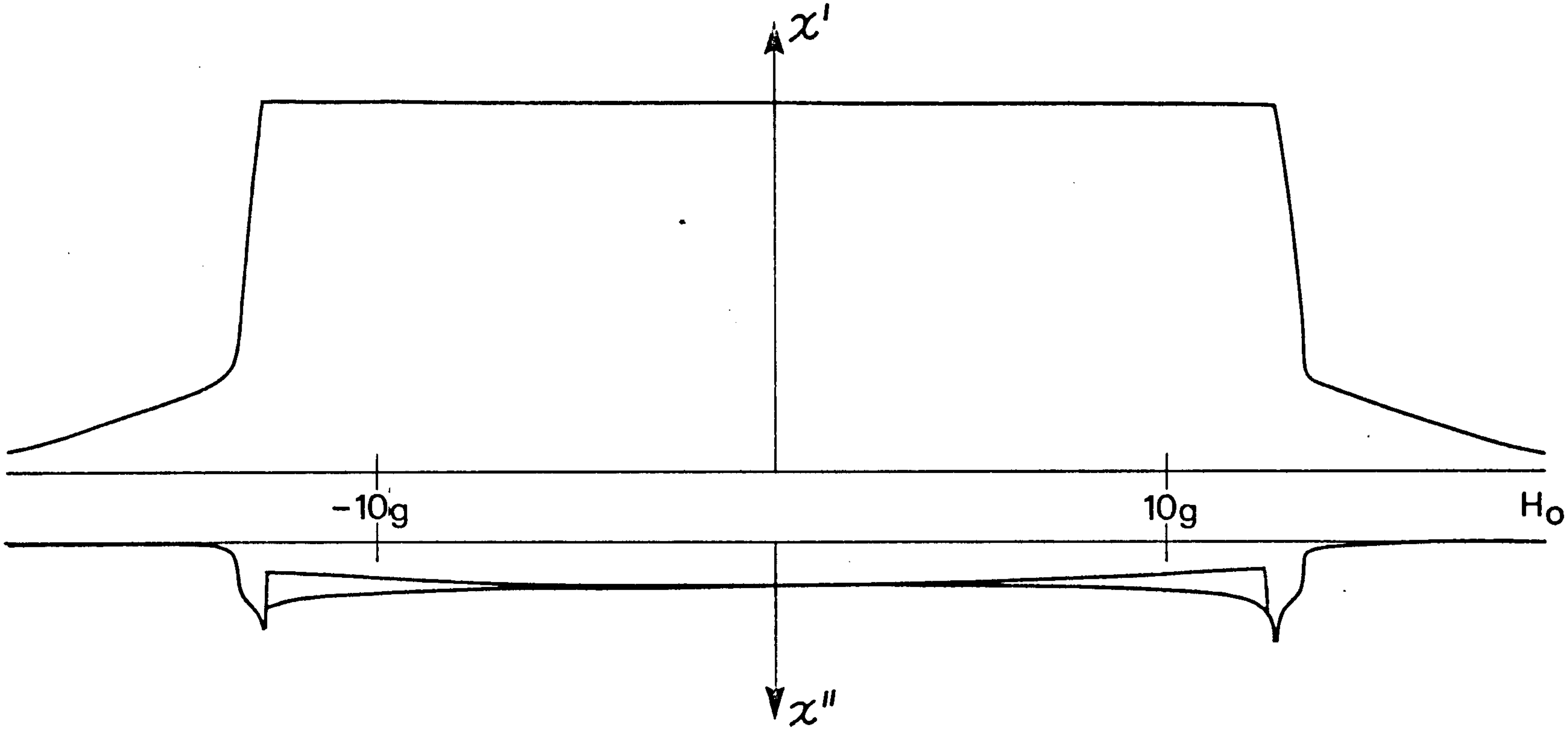

Fig 2.2b. Same as (a) except pick-up coil is at .3(L/2) from center.

is stable in fields $|H_o| < H_d$ (e.g. (5)). The Landau structure departs (before saturation) at H_d (6) to a more complicated domain structure, and the magnetization saturates quickly (7) at the center of the whisker. However, when measurements are made away from the center (Fig. 2.2b), we see a long tail in χ', showing the slower approach to saturation there.

The most important conclusion is that χ' is quite constant for $H_o < H_d$, and does not depend on the domain structure. (The slight deviation from constancy is due to damping. It disappears as $\omega \to 0$.) Because $\chi' = \frac{<m>}{h^o} = \frac{\partial <M>}{\partial H_o}$ is constant with applied field in this region,

$$<M(z)> = \chi'(z) H_o \quad , \tag{2.12}$$

where $<M(z)>$ is the average magnetization in the cross-section. By placing the pick-up coil at different positions, $\frac{<M(z)>}{H_o}$ can be measured. For a whisker in the Landau configuration, $<M(z)>$ tracks the shape of the 180° wall.

In Figs. 2.3a, b, c, d, e the measured $<M(z)>$ is plotted for the five different lengths, along with the theoretical curve for infinite susceptibility and the least square quadratic fit to the results of the theory (Chapter 5). The wall bows nearly quadratically in agreement with the prediction of the local model of Chapter 3. In Fig. 2.3a (which is the most accurate because the whisker is longest), the deviation of the experimental points from a quadratic shape is seen to

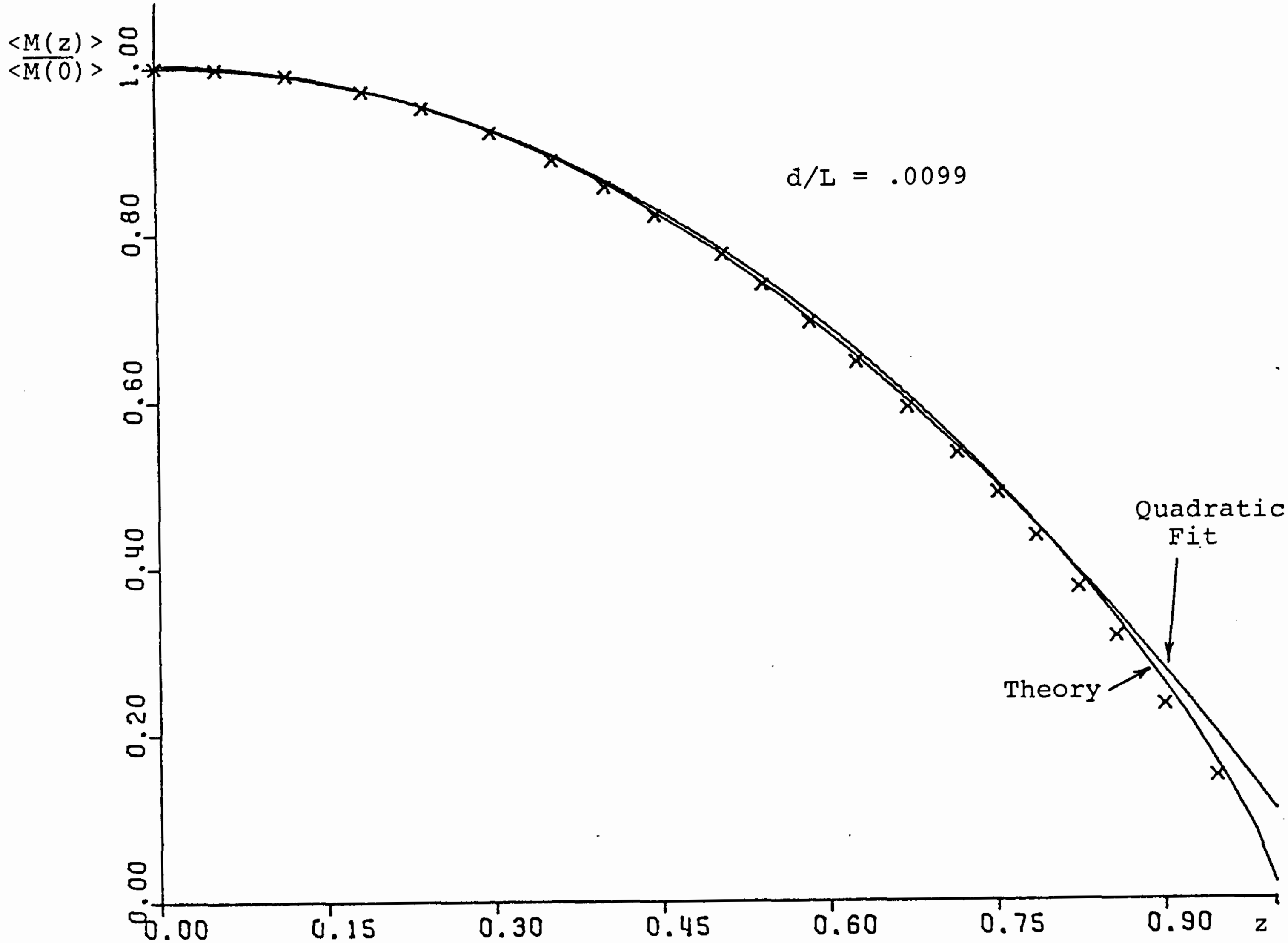

Fig. 2.3a. Homogeneous Driving. Average Magnetization in Whisker Cross-section. Points are experimental; curves are from theory of Chapter 5 (m=50) for infinite susceptibility. Whisker length is 2 in the dimensionless variable z. The quadratic is fit to theory for $z < .9$. $d/L = .0099$.

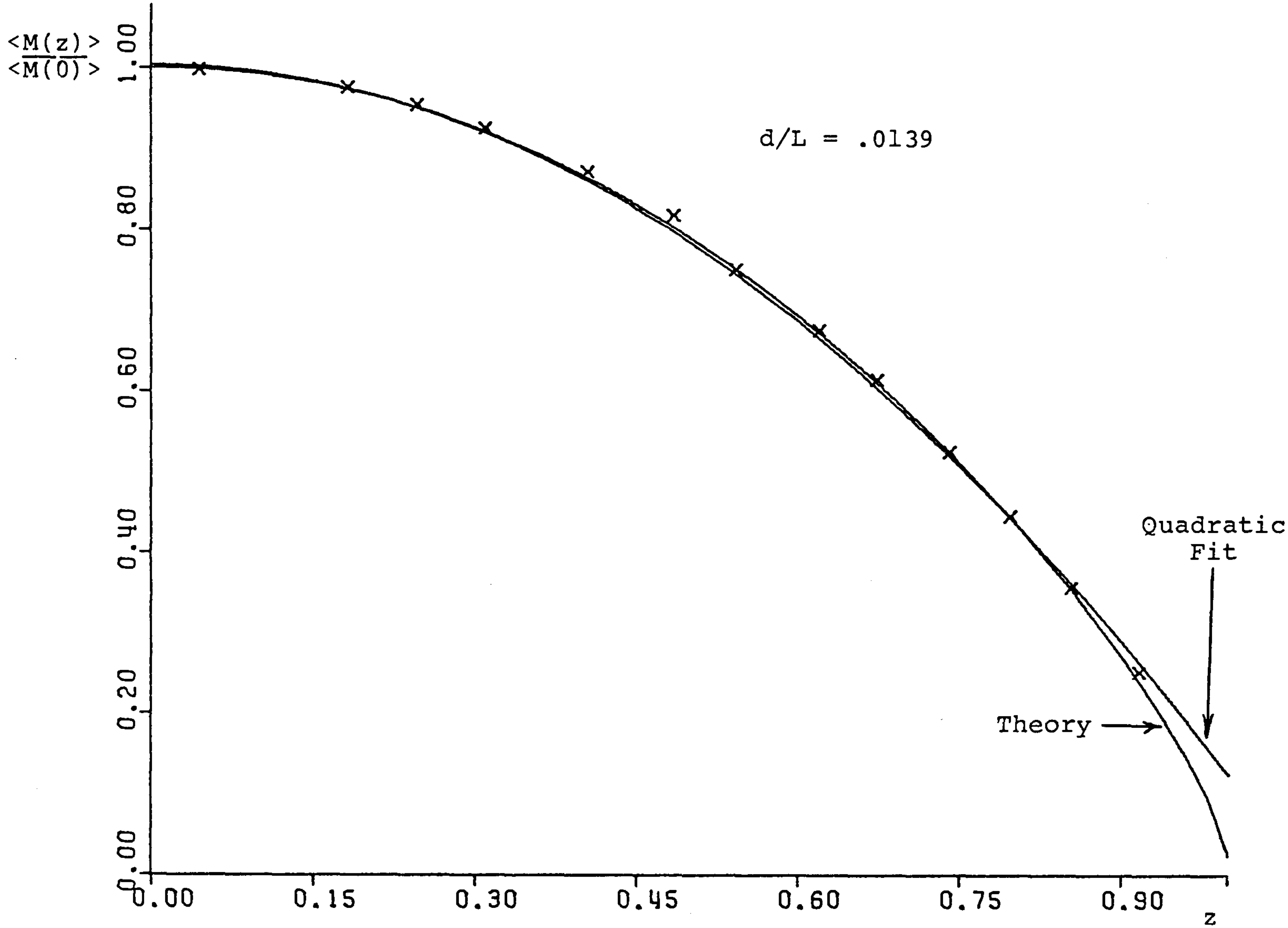

Fig. 2.3b. d/L = .0139.

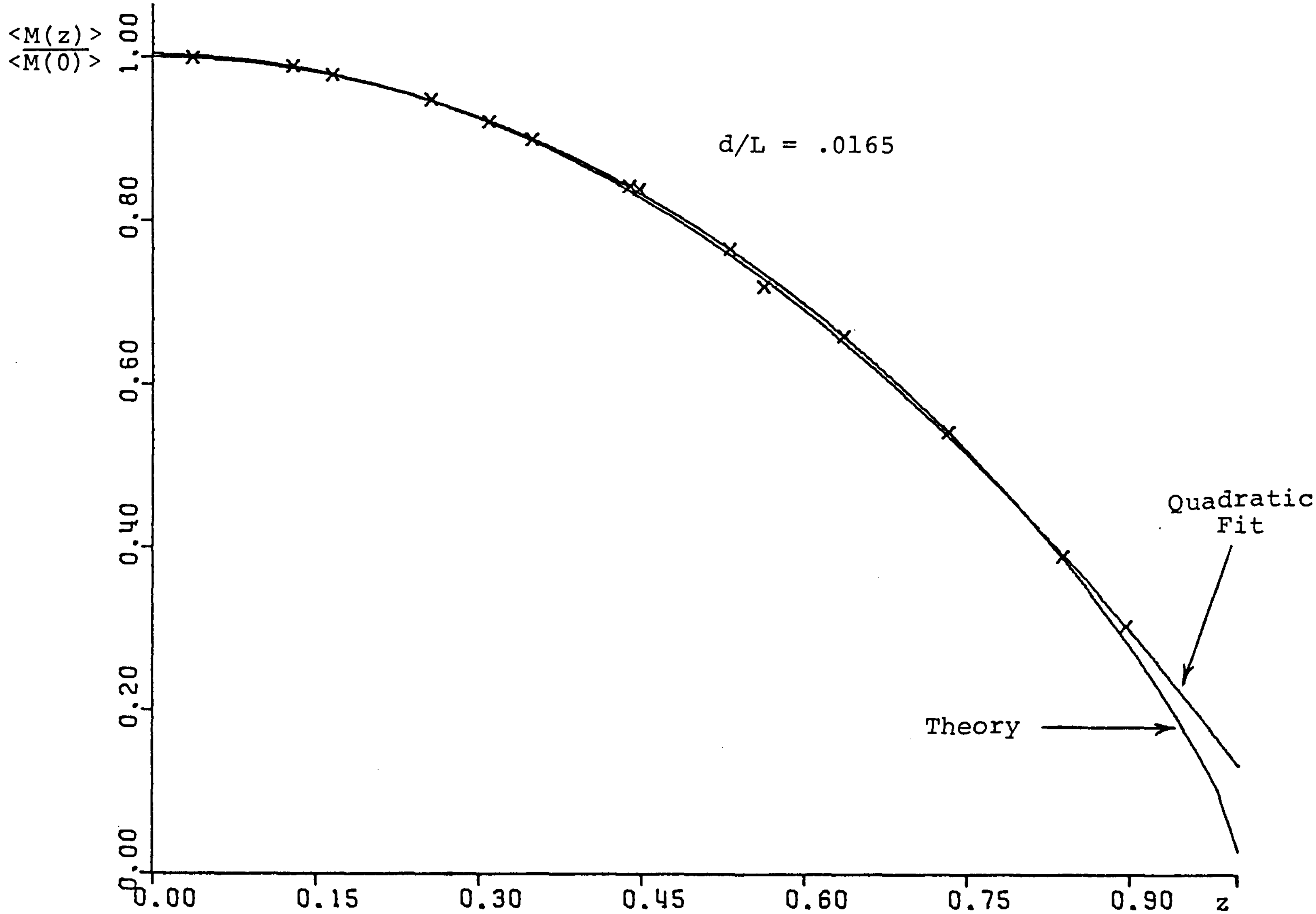

Fig. 2.3c. d/L = .0165.

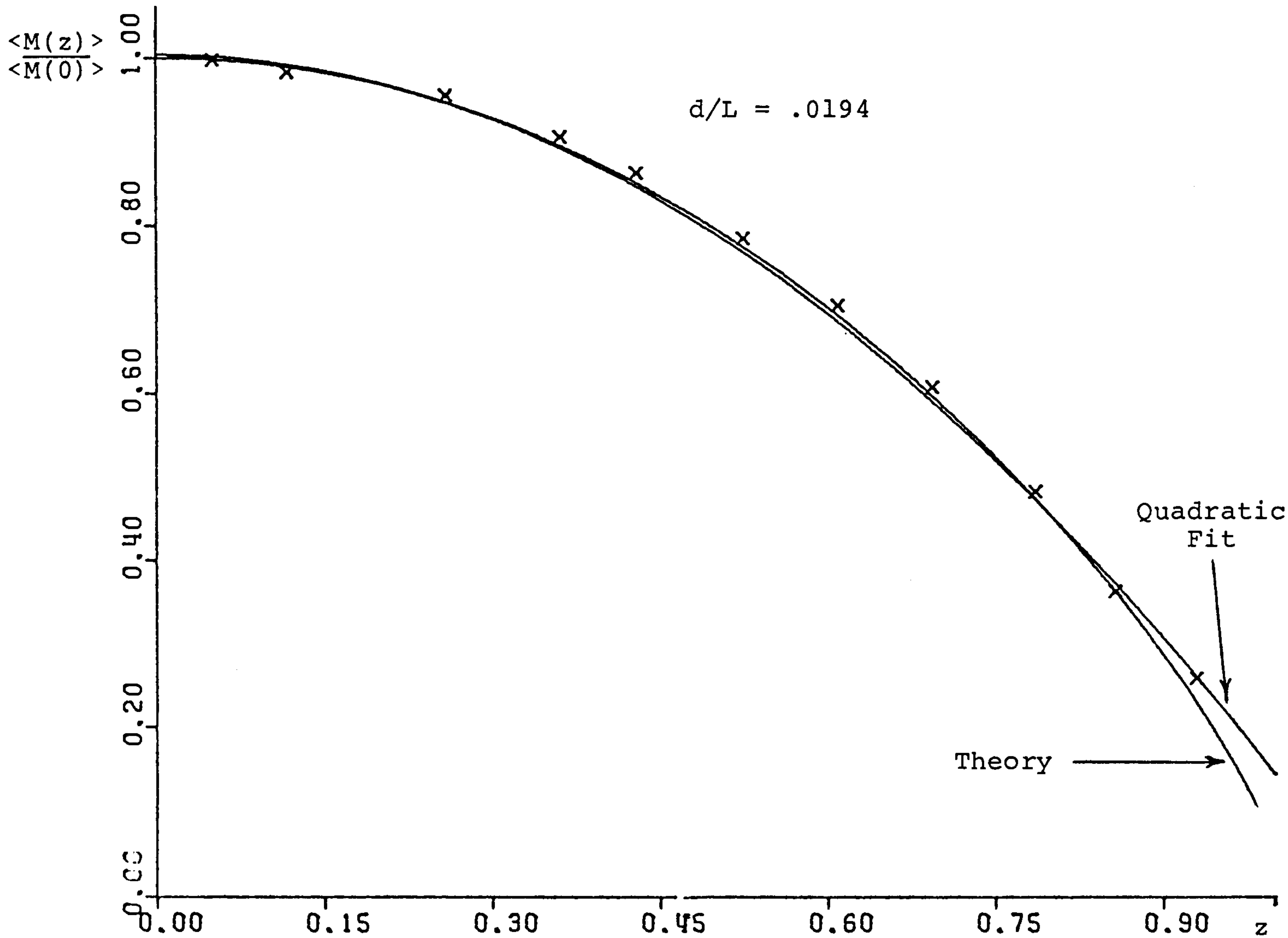

Fig. 2.3d. d/L = .0194.

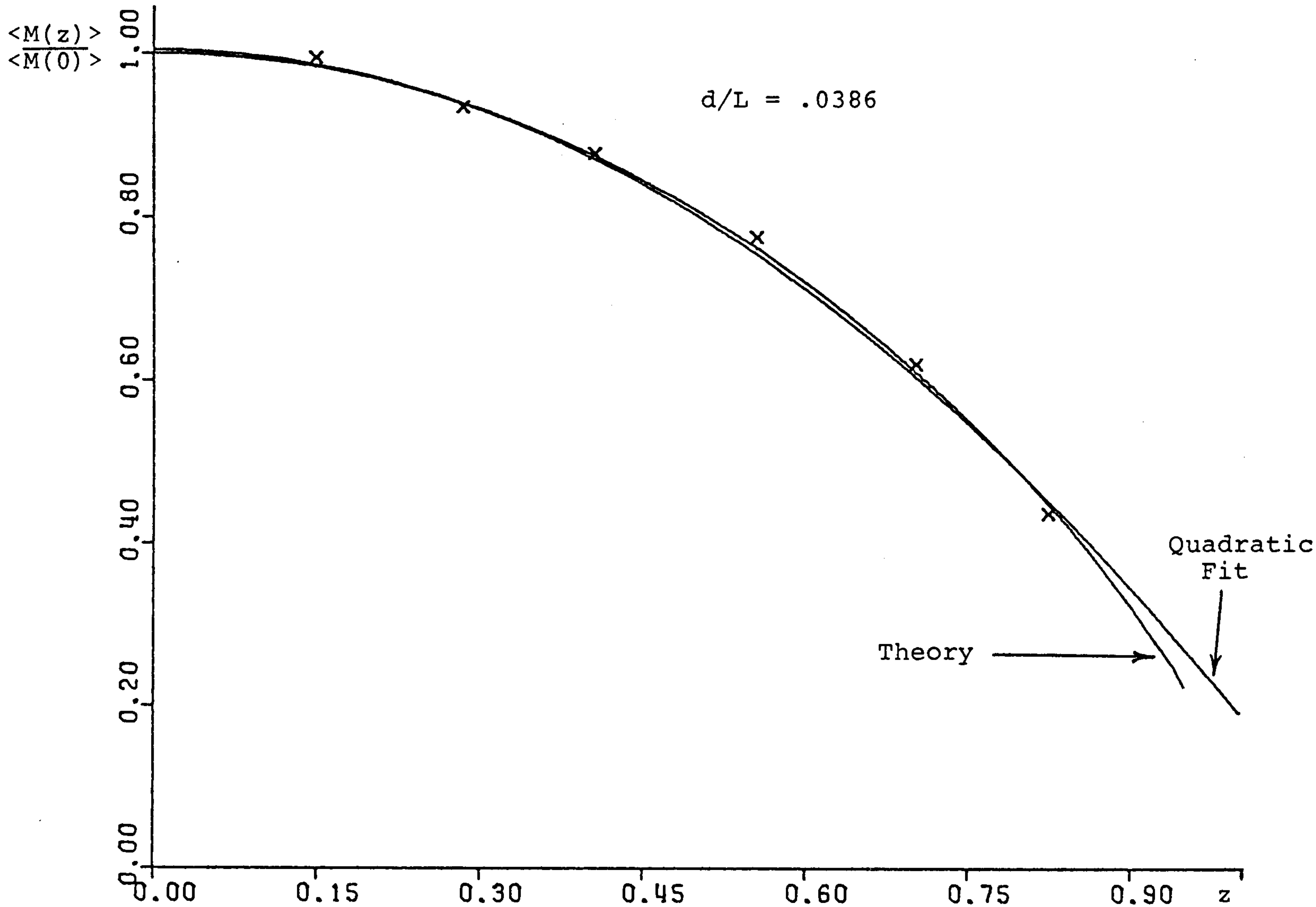

Fig. 2.3e. d/L = .0386.

follow the theoretical curve well.

At the departure field H_d one expects that $\langle M(0) \rangle$, the average value in the cross-section at the center, will be equal to M_s. Then the susceptibility can also be found from

$$\chi' = \frac{M_s}{H_d} \, . \tag{2.13}$$

In Fig. 2.4 the quantity $\chi' \frac{d}{L}$ is plotted for the five different whisker lengths. It is experimentally determined both from the departure field by (2.13) and from the calibrated susceptibility by (2.11). Three sets of theoretical values are given for the infinite susceptibility model (Chapter 5).

There are no adjustable parameters and results based on the calibration agree with the theory within the expected experimental accuracy. The departure field values are significantly larger. This is interpreted to mean the departure field (measured when the coil is at $z = 0$) is occurring <u>before</u> the wall touches the surface.

2.3.2 Local Driving

A 2-turn driving coil was placed at the center of the whisker for 3 different lengths. The magnetization curve $\chi'(H_o)$ was measured at various places and was similar to the curves for homogeneous driving (Fig. 2.2) except no tail was observed for $H_o > H_d$. This is reasonable because when the magnetization is saturated at the driving coil, there should be little response to the driving field anywhere in the whisker.

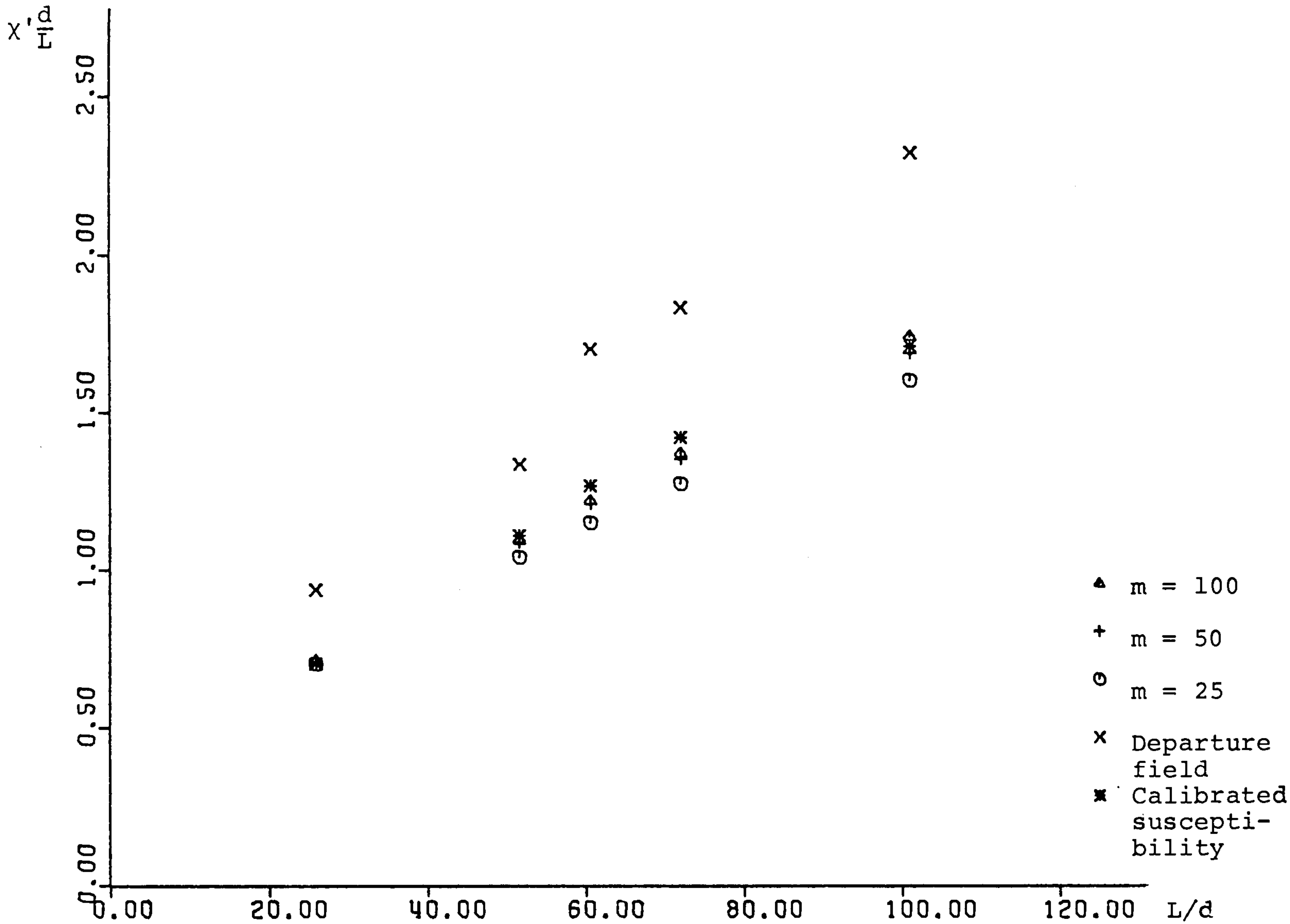

Fig. 2.4. Variation of $\chi'\frac{d}{L}$ with length. The most accurate theoretical points from Chapter 5 are for m = 100 (the cylinder is divided along its length into 2m segments for the numerical calculation). Departure field values $M_s d/H_d L$ are high because whisker is not perfect.

$\chi'(z)$ was also measured for $H_o = 0$ and is plotted in Figs. 2.5a, b, c. Also shown is the curve calculated for infinite susceptibility (Chapter 5), where the driving coil radius was set approximately equal to d. The displacement of the wall is nearly linear, in agreement with the prediction of the local model (Chapter 3). In Fig. 2.5c two different driving frequencies were used. No appreciable frequency dependence was observed.

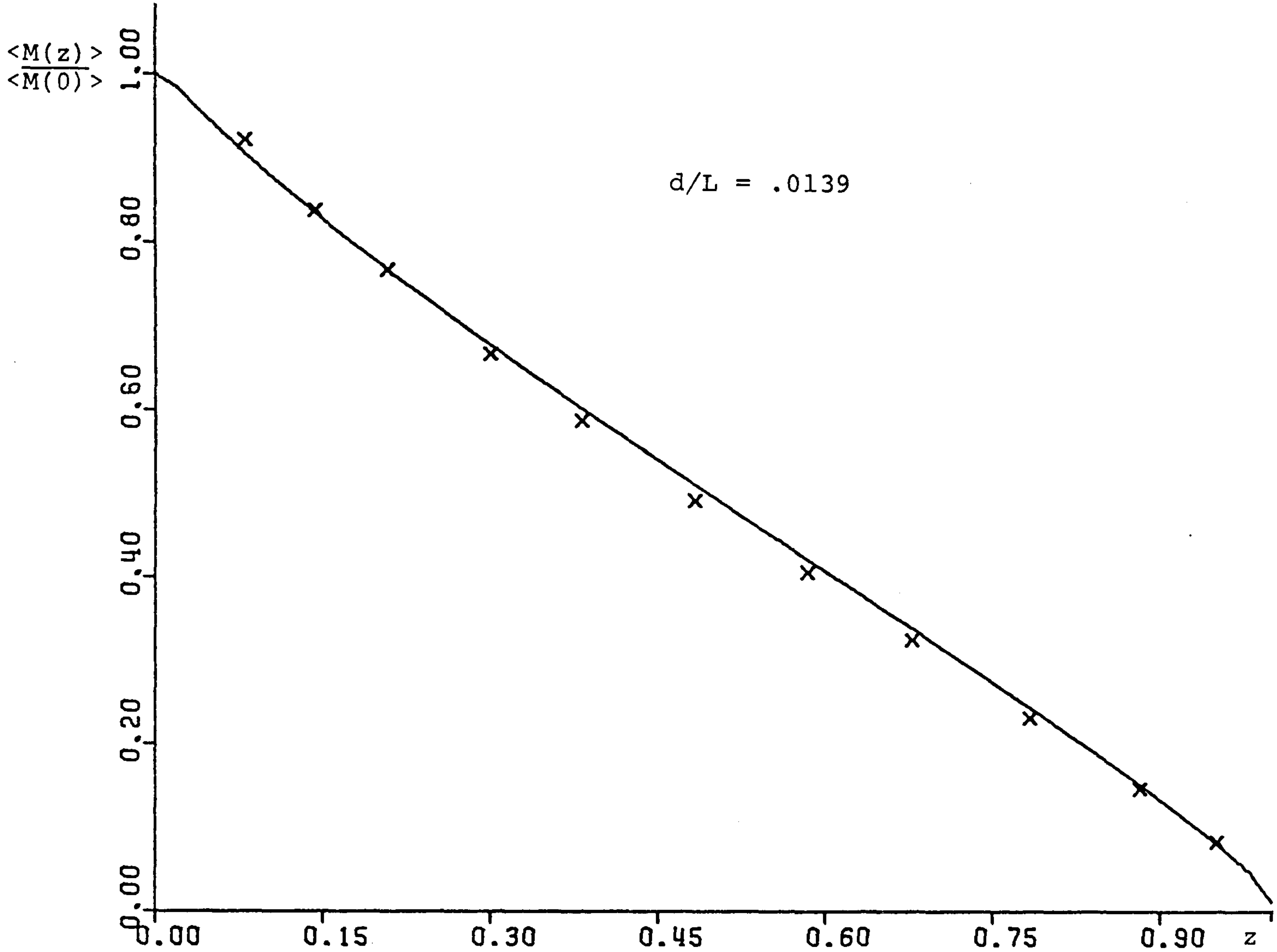

Fig. 2.5a. Local Driving. Average Magnetization in Whisker Cross-section. Points are experimental; theoretical curve is for driving coil radius $r_c = 2d/\sqrt{\pi}$ and m = 50. d/L = .0139.

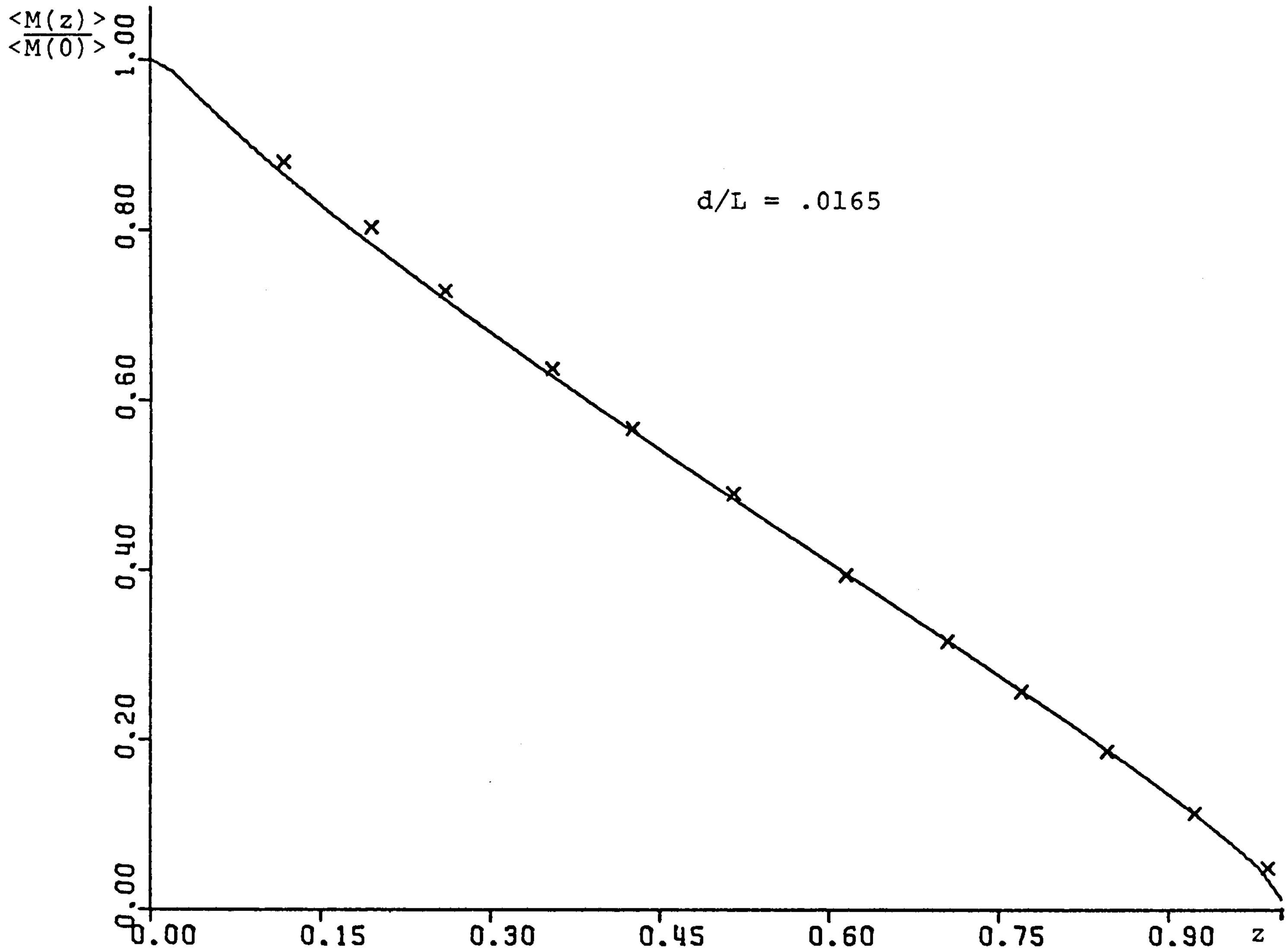

Fig. 2.5b. d/L = .0165.

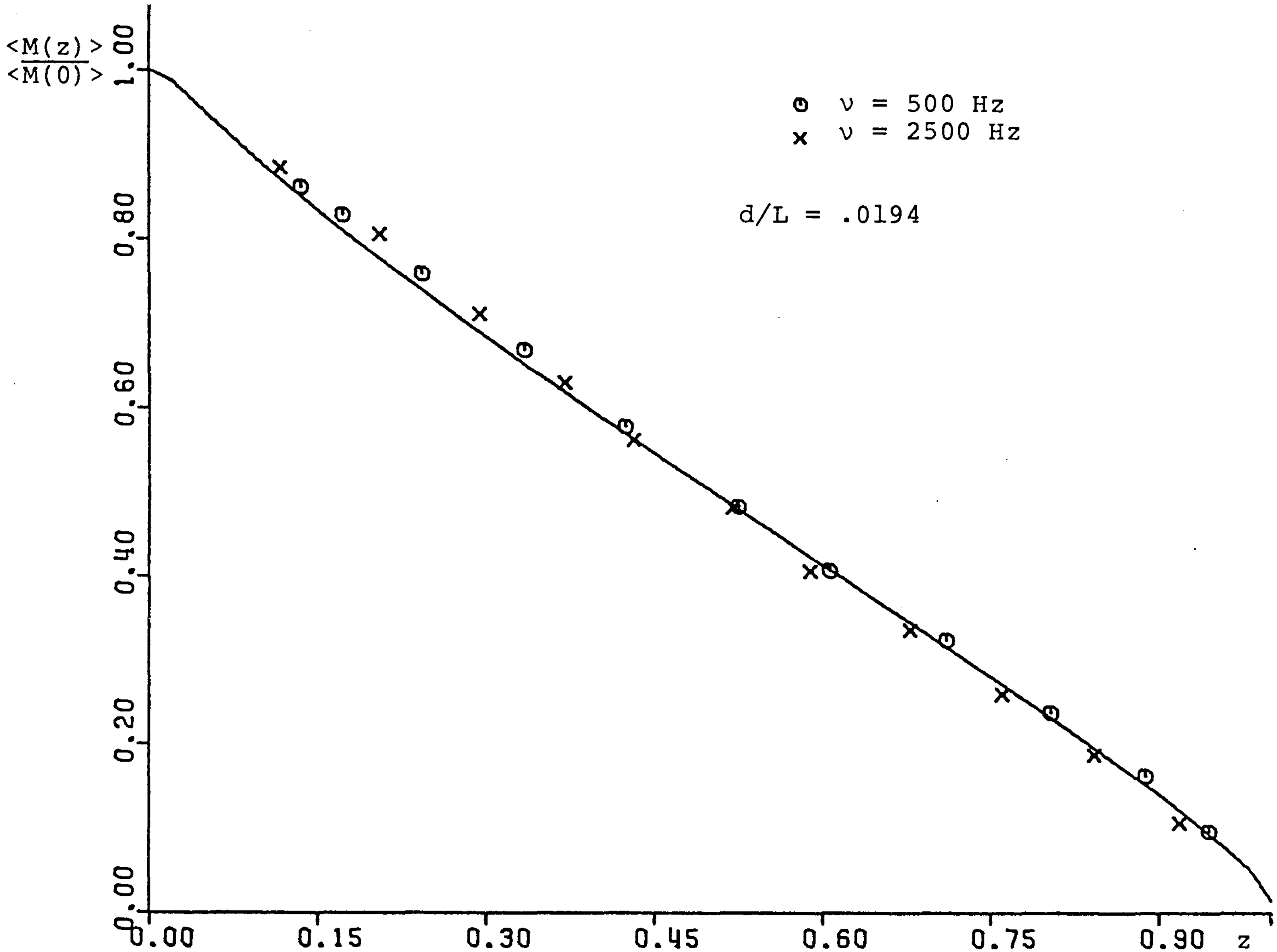

Fig. 2.5c. d/L = .0194. Experimental values are for two different driving frequencies.

CHAPTER 3

DEMAGNETIZING ENERGY AND SUSCEPTIBILITY

In this chapter we assume the Landau domain structure exists, and find approximations for the magnetostatic energy of a whisker in both homogeneous and local driving fields. The approximations will be of two types. In Sec. 3.2 we attempt to use a demagnetizing field calculated only from the local magnetization to find the energy. The usefulness of this local model is only in its predictive abilities (the long 180° wall behaves like a membrane with surface tension), and in the fact that more accurate calculations are difficult for high-frequency (damped) response.

In Sec. 3.3 we calculate accurate values for the demagnetizing energy, using experimentally observed wall shapes. These are non-local calculations, where the energy arises from the interaction of all the charges. We neglect anisotropy energy and find approximate expressions for the measured susceptibility.

3.1 Preliminary Considerations

3.1.1 Different Expressions for Demagnetizing Energy

In the pole formalism the magnetization is replaced by poles of density

$$\rho = -\vec{\nabla} \cdot \vec{M} \tag{3.1}$$

which act as the source for the demagnetizing field:

$$\vec{\nabla} \cdot \vec{H}' = 4\pi\rho \ . \tag{3.2}$$

This field is irrotational ($\vec{\nabla} \times \vec{H}' = 0$), and can thus be derived from a scalar potential U

$$\vec{H}' = -\vec{\nabla}U, \tag{3.3}$$

which in turn satisfies the Poisson equation

$$\nabla^2 U = -4\pi\rho \tag{3.4}$$

with the solution

$$U(\vec{r}) = \int \frac{\rho(\vec{r}')d\tau}{|\vec{r}-\vec{r}'|} \quad .$$

The demagnetizing energy is the interaction self-energy of these charges and can be written

$$\begin{aligned} E_d &= \tfrac{1}{2}\iint \frac{\rho(\vec{r})\rho(\vec{r}')}{|\vec{r}-\vec{r}'|}\, d\tau' d\tau \\ &= \tfrac{1}{2}\int U(\vec{r})\,\rho(\vec{r})\,d\tau. \end{aligned} \tag{3.5}$$

Using (3.4) and integrating by parts,

$$E_d = -\frac{1}{8\pi}\int U\nabla^2 U\, d\tau$$

$$= \frac{1}{8\pi}\int \vec{\nabla}U \cdot \vec{\nabla}U\, d\tau - \frac{1}{8\pi}\int \vec{\nabla} \cdot (U\,\vec{\nabla}\,U)\,d\tau\ .$$

The second term is converted to a surface integral which vanishes as 1/r at infinity, leaving

$$E_d = \frac{1}{8\pi}\int_{\text{all space}} H'^2\, d\tau\ . \tag{3.6}$$

From (3.6) it is clear that $E_d \geq 0$. The energy assumes its lowest possible value ($E_d = 0$) only in a curling pattern, where there are no poles. Starting again with (3.5), using (3.1), and integrating by parts,

$$E_d = -\tfrac{1}{2}\int U\,\vec{\nabla} \cdot \vec{M}\, d\tau$$

$$= \tfrac{1}{2}\int \vec{\nabla}U \cdot \vec{M}\, d\tau - \tfrac{1}{2}\int \vec{\nabla} \cdot (U\vec{M})\,d\tau\ .$$

The second term is again converted to a surface integral and vanishes when evaluated outside the region of magnetization, leaving

$$E_d = -\tfrac{1}{2}\int \vec{H}' \cdot \vec{M}\, d\tau\ . \tag{3.7}$$

Equations (3.6) and (3.7) are important results. They are connected by the following theorem (Brown, <u>Magnetostatic Principles in Ferromagnetism</u>, p. 44-45): Let $\vec{u}$ and $\vec{v}$ be functions which fall off at least as fast as $\frac{1}{r^2}$ for large r, and let $\vec{u}$ be irrotational ($\vec{\nabla} \times \vec{u} = 0$) and $\vec{v}$ be solenoidal ($\vec{\nabla} \cdot \vec{v} = 0$) everywhere. Then

$$\int_{\text{all space}} \vec{u} \cdot \vec{v}\, d\tau = 0$$

We let $\vec{u} = \vec{H}'$, $\vec{v} = \vec{H}' + 4\pi\vec{M} \equiv \vec{B}'$. Then

$$\frac{1}{8\pi}\int_{\text{all space}} H'^2\, d\tau = -\tfrac{1}{2}\int_{\text{all space}} \vec{H}' \cdot \vec{M}\, d\tau$$

follows directly from the theorem.

3.1.2 Distribution of Magnetic Charge Along the Whisker Axis

Fig. 3.1 shows a section of the whisker with two different magnetization configurations. In (a) the magnetization is parallel to the sides of the whisker, putting the poles on the wall. In (b) the magnetization is parallel to the wall, putting the poles on the surface. The slope of the wall is θ. In both cases it is seen from Gauss' theorem that the charge/unit length is

$$\frac{Q}{\Delta z} = 2dM_s\theta[1 + O\ (\theta^2)].$$

As long as the magnetization makes small angles with the z-axis, the net flux of $\vec{M}$ into the region (and hence the charge) will be proportional to θ.

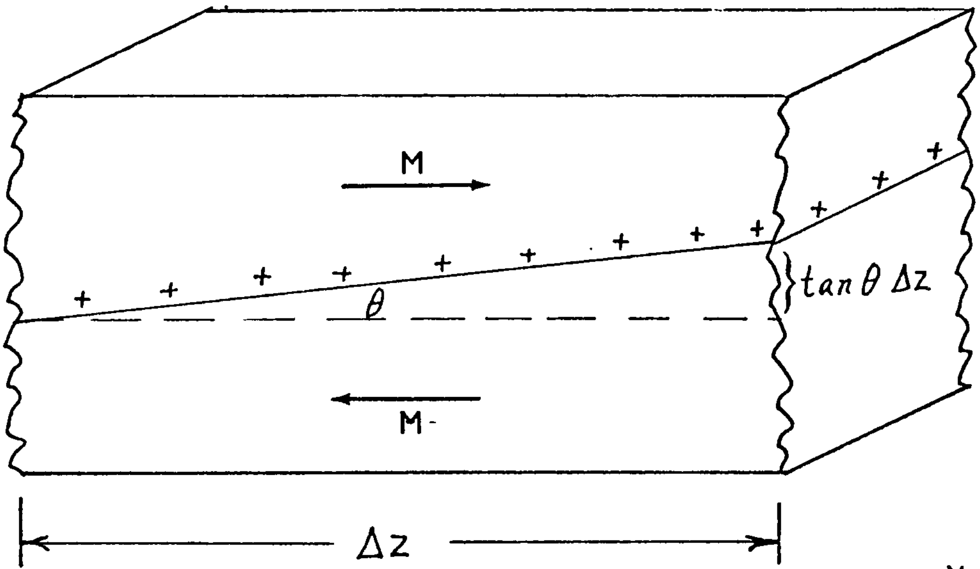

(a)

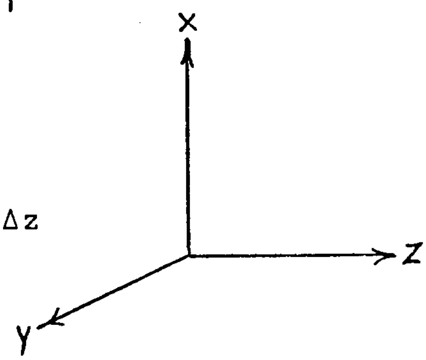

$$Q = - \iiint \vec{\nabla}\cdot\vec{M}\, d\tau = - \iint \vec{M}\cdot d\vec{S} = 2M_s d \tan\theta \ \Delta z$$

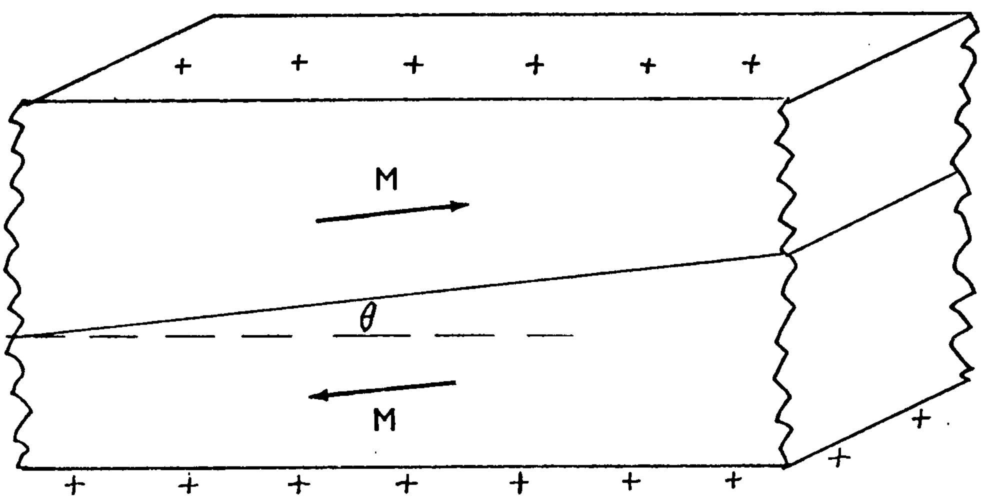

(b)

$$Q = - \iint \vec{M}\cdot d\vec{S} = 2M_s d \sin\theta \ \Delta z$$

Fig. 3.1. Possible magnetization in a short segment of whisker with resulting pole distributions. The angle θ of the Bloch wall with the surface is exaggerated for clarity. (a) $\vec{M}$ parallel to surface; (b) $\vec{M}$ parallel to wall.

3.2 The Local Model: A Simple Treatment of Demagnetizing Energy

3.2.1 Homogeneous Driving

The Landau domain configuration is shown in Fig. 3.2a. Under the influence of a longitudinal field $\vec{H}_o = H_o\hat{z}$ the 180° wall bows and the pinning points move to increase the magnetization in the $+\hat{z}$ direction (Fig. 3.2b). The wall shape is described by an unknown function $x(z)$.

The local model assumes that the demagnetizing field at any point can be found from the charge density there. A magnetization parallel to the surface results in a charge density of poles on the wall

$$\sigma_w = 2M_s \frac{dx}{dz} \quad . \tag{3.8}$$

This gives the demagnetizing field a component in the z-direction at the wall of magnitude

$$H_z'(z) = 2\pi\sigma_w \frac{dx}{dz} = 4\pi M_s \left(\frac{dx}{dz}\right)^2 \quad . \tag{3.9}$$

For simplicity this field is taken to be uniform throughout the cross-section of the whisker. (This would seem to be an over-estimate of the longitudinal field, but we will see in Chapter 5 that because of the non-local nature of the field, this is still an underestimate.) From (3.7), the demagnetizing energy is

$$E_d = -\tfrac{1}{2}\int \vec{H}' \cdot \vec{M}\, d\tau = 2\pi M_s{}^2 d^2 \int_{-L/2}^{L/2} \left(\frac{dx}{dz}\right)^2 dz \, . \tag{3.10}$$

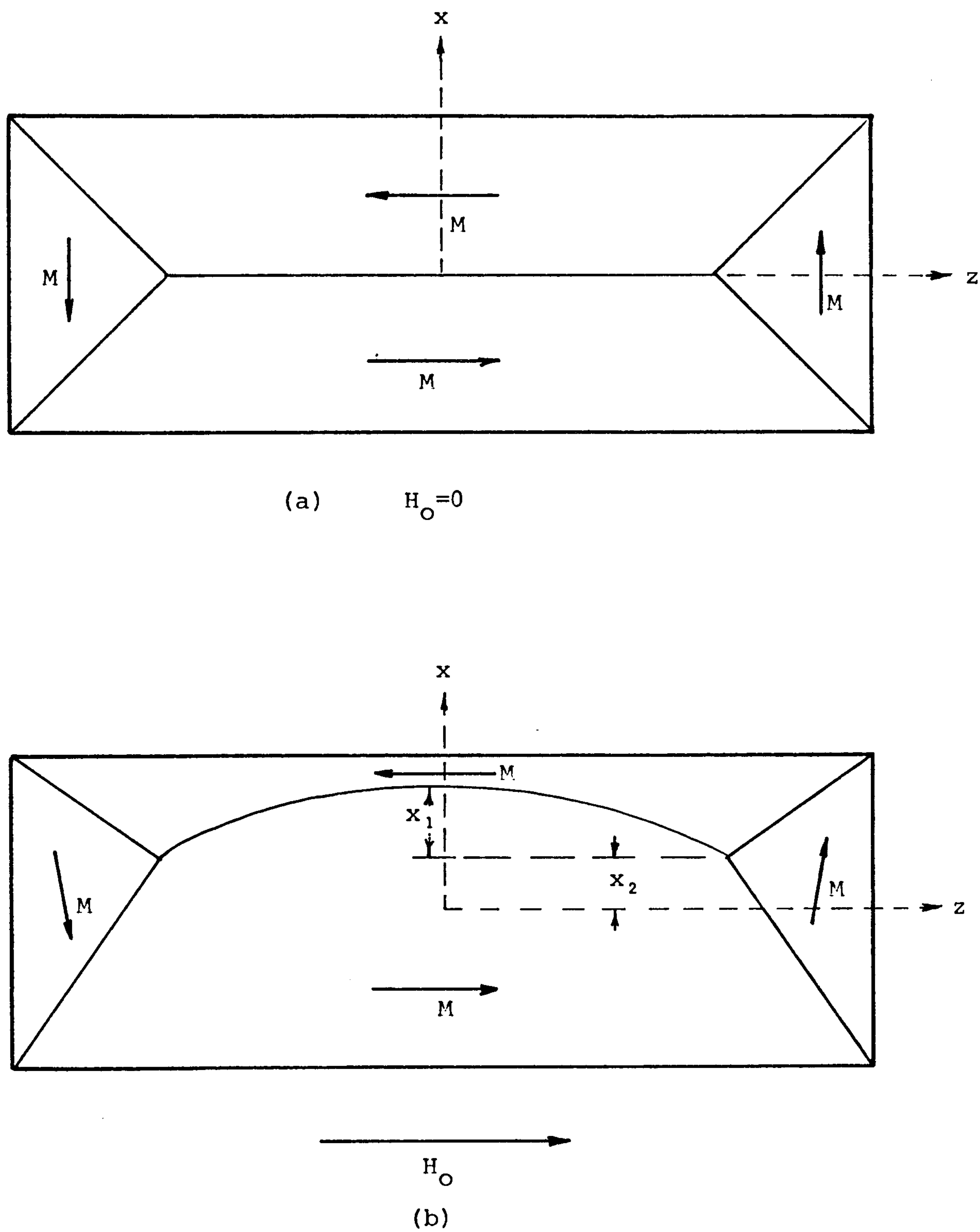

Fig. 3.2. (a) Landau Configuration in Zero Applied Field, (b) Schematic Magnetization in Applied Field (See Fig. 7.1 for more accurate representation).

The magnetizing energy is

$$E_m = -\int \vec{M} \cdot \vec{H}_o \, d\tau = -2M_sH_od\int_{-L/2}^{L/2} x dz \, . \qquad (3.11)$$

Variation of $x(z)$ to minimize $E = E_d + E_m$ (with pinning of the end points) yields the "force" equation

$$\alpha \frac{d^2x}{dz^2} = -2M_sH_od \, , \qquad (3.12)$$

where $\alpha = 4\pi M_s{}^2d^2$ is the tension in the wall due to the demagnetizing field. Using the boundary conditions

$$\frac{dx}{dz}(0) = 0 \qquad \text{and} \qquad x\left(\pm \frac{L}{2}\right) = 0,$$

the solution to (3.12) is

$$x(z) = x_1\left[1-\left(\frac{2z}{L}\right)^2\right] , \qquad (3.13)$$

where $x_1 = \dfrac{H_oL^2}{16\pi M_sd}$ is the displacement at the center of the wall.

The bowing of the long wall is quadratic. We introduce a more concise notation and use (3.10) and (3.11) to write the demagnetizing and magnetizing energies in terms of x_1:

$$E_d = \tfrac{1}{2} k_1x_1^2 \, ,$$

where

$$k_1 \equiv \gamma \frac{M_s{}^2d^2}{L} \quad \text{and} \quad \gamma = \frac{64\pi}{3} \quad ; \qquad (3.14)$$

$$E_m = -h x_1 ,$$

where

$$h \equiv \frac{4}{3} M_s H_o dL \quad . \tag{3.15}$$

The energy $E = E_d + E_m$ is a minimum when (as before)

$$x_1 = \frac{h}{k_1} \quad \text{and} \quad E = -E_d \quad . \tag{3.16}$$

In fact, the tie points at the end of this wall are not pinned; they act as if joined to the z-axis by springs. The demagnetizing energy which results from displacing these points a distance x_2 can be written (see Sec. 3.3.1)

$$E_d' = \tfrac{1}{2} k_2 x_2^2 \tag{3.17}$$

where $k_2 = \eta M_s{}^2 d$ (η is a dimensionless number). This displacement gives a magnetizing energy

$$E_m' = -\frac{3}{2} h x_2 \quad . \tag{3.18}$$

Minimizing $E' = E_d' + E_m'$ gives

$$x_2 = \frac{3}{2} \frac{h}{k_2} \quad \text{and} \quad E' = -E_d' \quad . \tag{3.19}$$

These "springs" (long wall and tie points) are not coupled in this model, and the total energy is

$$E_T = \tfrac{1}{2}(k_1 x_1^2 + k_2 x_2^2) - h(x_1 + \frac{3}{2} x_2)$$

$$= -\tfrac{1}{2}(k_1 x_1^2 + k_2 x_2^2) .$$

The total displacement of the wall is

$$x_T(z) = h\left\{\frac{1}{k_1}\left[1 - \left(\frac{2z}{L}\right)^2\right] + \frac{3}{2k_2}\right\}; \tag{3.20a}$$

at the center this reduces to

$$x_T(0) = x_1 + x_2 = h\left(\frac{1}{k_1} + \frac{3}{2k_2}\right)$$

$$= \frac{4}{3M_s}\left(\frac{L^2}{d\gamma} + \frac{3L}{2\eta}\right) H_o \ . \tag{3.20b}$$

3.2.2 Predictions for Homogeneous Driving

A. Shape of the Wall

The first prediction of the local model is that in a homogeneous field H_o the wall is bowed quadratically, leading to a parabolic longitudinal magnetization with a maximum in the center. The actual magnetization is close to quadratic (see Fig. 2.3).

B. Departure Field

As H_o increases, the tie points are displaced and the wall bows until, in a perfect crystal, it touches the surface at $H_o = H_d$, the departure field. The wall then breaks and the whisker approaches saturation with a much reduced susceptibility. The departure field occurs when

$$x_T(0) = \frac{d}{2} = h_d\left(\frac{1}{k_1} + \frac{3}{2k_2}\right),$$

or

$$\frac{M_s d}{H_d L} = \frac{8L}{3\gamma d} + \frac{4}{\eta} \ . \tag{3.21}$$

See Tables 3.2a and 3.2b (p.66-67) for values predicted by this 2-spring model. (The value of γ used there is <u>not</u> $\frac{64\pi}{3}$ from the local model).

C. Differential Susceptibility: Independent of H_o, M_s

The magnetic moment of the whisker is

$$\mathcal{M} = \int \vec{M}\, d\tau = \int_{-L/2}^{L/2} \langle M(z)\rangle dz = 2\int_{-L/2}^{L/2} M_s d\ x(z)\ dz \ .$$

The bulk differential susceptibility is from (3.20)

$$\chi'^{\,bulk} = \frac{1}{V}\frac{\partial \mathcal{M}}{\partial H_o} = \frac{16}{9}\left(\frac{L}{d}\right)^2\left[\frac{1}{\gamma} + \frac{9}{4\eta}\left(\frac{d}{L}\right)\right], \tag{3.22}$$

which is independent of M_s and depends only on the dimensions of the whisker. The bulk susceptibilty can be measured with a pick-up coil much longer than the whisker.

In the experiment a small pick-up coil of N_p turns (N_p = 10) is used, which measures instead the longitudinal flux of $\vec{M}$ at only one point along the whisker. The internal magnetic induction is

$$\vec{B}_i = \vec{H}_o + \vec{H}' + 4\pi\vec{M}$$

where $\vec{H}$ is the demagnetizing field. For typical whiskers ($L/d \sim 50$), $4\pi\langle M(z=0)\rangle$ = 22,000 gauss when $H_o = H_d \sim 20$ gauss. Also, as will be shown in Sec. 4.3.2, $\vec{H}_i = \vec{H}_o + \vec{H}' \cong 0$ below saturation, so

$$\vec{B}_i = 4\pi\vec{M}$$

is an excellent approximation.

As in Chapter 2, we consider the differential fields, magnetization changes, and fluxes produced by a small superimposed a.c. field $h^o e^{i\omega t}$. For the geometry used, the signal obtained at z = 0 after subtracting the background (when the sample is saturated) is from (2.10)

$$\varepsilon_p = -\frac{1}{c}\frac{\partial\phi}{\partial t} \cong 4\pi \frac{\omega}{c} N_p \int_{\text{sample}} \vec{m}\, dS = 8\pi N_p \frac{\omega}{c} M_s d\, \Delta x_T(0) , \qquad (3.23a)$$

where $x_T(0)$ is the differential displacement of the wall at z = 0, giving rise to a differential change in net magnetization $\vec{m}$. A term from the demagnetizing field of the whisker of relative size

$$\frac{A_p}{4\pi\chi' d^2} \sim \frac{1}{100} \qquad \text{for } \frac{L}{d} = 50$$

has been neglected. Δx_T is due to the arbitrarily small field h^o. Using (3.20a, 3.23a),

$$\varepsilon_p = \frac{32\pi}{3}\frac{\omega}{c} N_p \left[\frac{L^2}{\gamma} + \frac{3Ld}{2\eta}\right] h^o . \qquad (3.23b)$$

Note that the signal to a first approximation (neglecting the effect of the end spring) is independent of d. Two whiskers of the same length give approximately the same signal. A superimposed d.c. field H_o does not change the signal as long as the wall is able to move freely. This signal is again independent of M_s (and hence temperature). No deviations from linear susceptibility are observed experimentally at low frequency ($\nu \lesssim 10^3$ Hz) for applied fields smaller than H_d where the wall can bow freely.

The susceptibility at the center is found from (2.9, 2.10, 3.23b) to be

$$\chi'(0) = \frac{N_c A_c}{4\pi N_p} \frac{\varepsilon_p}{\varepsilon_c} \frac{1}{d^2} = \frac{8}{3\gamma}\left(\frac{L}{d}\right)^2 + \frac{4}{\eta}\left(\frac{L}{d}\right) . \tag{3.24a}$$

When the pick-up coil is not at the center this is easily generalized to

$$\chi'(z) = \frac{8}{3\gamma}\left(\frac{L}{d}\right)^2 \left[1 - \left(\frac{2z}{L}\right)^2\right] + \frac{4}{\eta}\left(\frac{L}{d}\right) . \tag{3.24b}$$

Note the equivalence:

$$\chi'(0) = \frac{\langle m \rangle}{h^o} = \frac{\langle M \rangle}{H_o} = \frac{M_s}{H_d} . \tag{3.25}$$

For iron whiskers only the z-component contributes to the average.

D. Deflection of the Tie points

From (3.20a) the fraction of the signal at z = L/2 to the signal at the center is

$$\frac{x_2}{x_T(0)} = \frac{1}{1 + \frac{2\eta}{3\gamma}\frac{L}{d}} . \tag{3.26}$$

Table 3.3 gives theoretical values for the ratio of displacement at the end, x_2, to that at the center, $x_1 + x_2$.

3.2.3 Local Driving

Instead of using homogeneous d.c. and driving fields, one can use a fine coil at $z = 0$ to drive the magnetization and a small pick-up coil as before to sample the response at different values of z. We again use the local model for the demagnetizing field. The magnetizing energy here is

$$E_m = -2M_s d \int_{-L/2}^{L/2} H_z(z)\, x(z)\, dz \quad .$$

The axial applied field a distance z from a one-turn coil of radius r_c, current I, is

$$H_o(z) \doteq H_o \frac{1}{[1+\left(\frac{z}{r}\right)^2]^{3/2}} \tag{3.27}$$

where $H_o = \dfrac{2\pi I}{cr_c}$ is the field at the center of the coil. The integrated strength of this field is

$$\bar{H} = 2\int_0^{\infty} H_o(z)\, dz = 2H_o r \quad .$$

For simplicity we will take the driving field to be $\bar{H}\delta(z-0)$.

Then

$$E_m = 2M_s \bar{H} d \int_{-L/2}^{L/2} x(z)\, \delta\, (z-0)\, dz \quad . \tag{3.28}$$

Variation of x as before to minimize E gives

$$\alpha \frac{d^2x}{dz^2} = -2M_s\bar{H}d \ \delta(z-0) \ . \tag{3.29}$$

Integration from $-\Delta$ to Δ gives

$$\alpha \frac{dx}{dz}\bigg|_{-\Delta}^{\Delta} = \left(2 \ \alpha \ \frac{dx}{dz} \ (\Delta)\right) = -2M_s\bar{H}d .$$

Using the boundary condition $x\left(\frac{L}{2}\right) = 0$,

$$x(z) = x_1\left(1-\left|\frac{2z}{L}\right|\right) \ , \qquad x_1 = \frac{\bar{H}L}{8\pi M_s d} \ . \tag{3.30}$$

The local model predicts the wall will be triangular, with its apex at the driving coil. The wall is pulled upward by the driving field and behaves like an elastic membrane with a tension determined by the demagnetizing fields. If we permit the driving field to be smeared out (as it actually is) the top of the triangle becomes rounded, with the curvature still determined by the strength of the driving field.

Again using (3.11) and (3.10) the energies can be written

$$E_m = -h^L x_1 \tag{3.31}$$

where

$$h^L = -2M_s\bar{H}d \ ,$$

and

$$E_d = \tfrac{1}{2}k_1^L x_1^2$$

where

$$k^L = \gamma^L \frac{M_s{}^2 d^2}{L} \ , \quad \gamma^L = 16\pi \ . \tag{3.32}$$

Note that $\gamma^L < \gamma$. The demagnetizing energy is less for the linear wall than the quadratic because the + and - charges are less separated.

The magnetizing energy due to the end springs is

$$E_m' = -2M_s\bar{H}dx_2 = -\mathscr{h}^L x_2 \ . \tag{3.33}$$

and the demagnetizing energy is again

$$E_d' = \tfrac{1}{2}\, k_2 x_2^2 \ . \tag{3.34}$$

Minimization of the total energy with respect to x_1 and x_2 gives at $z = 0$

$$x_T(0) = x_1 + x_2 = \mathscr{h}^L\left(\frac{1}{k_1^L} + \frac{1}{k_2}\right) . \tag{3.35}$$

The fraction of the signal at the end to that in the center is

$$\frac{x_2}{x_T(0)} = \frac{1}{1 + \frac{\eta}{\gamma^L}\frac{L}{d}} \ .$$

This fraction is < .1 for typical whiskers. The local model predicts the relative end-spring deflection in homogeneous driving to be about twice that in local driving:

$$\text{Ratio} = \frac{1 + \frac{\eta}{\gamma^L}\frac{L}{d}}{1 + \frac{2\eta}{3\gamma}\frac{L}{d}} \cong \frac{3\gamma}{2\gamma^L} = 2 \ .$$

Experiment tends to bear this out, the wall being displaced at the end about 5-6 percent of the center deflection. (Compare with Table 3.3 for homogeneous driving.)

3.3 Non-local Calculations of Energy

As we saw in Sec. 3.1, the demagnetizing energy can be found from the self-energy of the poles:

$$E_d = \frac{1}{2}\int \frac{\rho(\vec{r})\rho(\vec{r}\,')}{|\vec{r}-\vec{r}\,'|}\, d\tau\, d\tau' \ .$$

The problem is that we must know the micromagnetic solution $\vec{M}(\vec{r})$ in order to find $\rho(\vec{r})$. The approach taken in Chapter 4 is to find the transverse $\vec{M}$ and ρ in any cross-section of the whisker self-consistently. The result is then used in Chapter 5 to find the longitudinal $\vec{M}$ self-consistently. In this section we will use the longitudinal $\vec{M}$ found from experiments and calculate the demagnetizing energy for different configurations of the transverse $\vec{M}$. We will also give a more accurate description of the magnetostatic energy than the local model (Sec. 3.2).

3.3.1 Homogeneous Driving Field

A. Long Wall

From both experiment and a self-consistent calculation of the longitudinal magnetization (Chapter 5), we know that in a homogeneous field $\vec{H}_o$ the long wall bows nearly quadratically. A quadratic bowing gives rise to a charge/unit length of

$$2M_s d\,\frac{dx}{dz} = -\,\frac{16M_s x_1 d}{L^2}\, z \qquad (3.36)$$

along the whisker. Here we consider the demagnetizing energy for the cases:

(i) the charge is on the wall

(ii) The charge is on two surfaces (say, parallel to the wall)

(iii) the charge is equally on all four surfaces

(iv) the charge is on the surface of a cylinder with cross-sectional area equal to d^2,

with the above linear variation of charge density.

We first find the interaction energy between two strips of charge density

$$\sigma(z) = \sigma_o \frac{z}{L/2}$$

(where $\sigma_o = \frac{8M_s x_1}{L}$), of width dy and dy', and separated by $s = |y-y'|$. This energy is

$$d^2E = \frac{\sigma_o^2 \, dydy'}{\left(\frac{L}{2}\right)^2} \int_{-L/2}^{L/2} zdz \int_{-L/2}^{L/2} z'dz' \frac{1}{[(z-z')^2+s^2]^{\frac{1}{2}}}$$

$$= \frac{2L}{3}\left(\ln \frac{2L}{|y-y'|} - \frac{7}{3}\right) \sigma_o^2 dydy' \quad . \tag{3.37}$$

(see Appendix 1A).

In Appendix 1B the demagnetizing energy is found for the four above cases, in the form

$$E_d = \tfrac{1}{2} \gamma \frac{M_s^2 d^2}{L} x_1^2 \quad ,$$

where

$$\gamma_w = \frac{128}{3}\left[\ln\frac{2L}{d} - \frac{5}{6}\right] \tag{3.38a}$$

$$\gamma_{2s} = \frac{128}{3}\left[\ln\frac{2L}{d} - \frac{5}{6} - \frac{\pi}{4}\right] \tag{3.38b}$$

$$\gamma_{4s} = \frac{128}{3}\left[\ln\frac{2L}{d} - \frac{5}{6} - \left(\frac{\pi+\ln 2}{4}\right)\right] \tag{3.38c}$$

$$\gamma_c = \frac{128}{3}\left[\ln\frac{2\sqrt{\pi}L}{d} - \frac{7}{3}\right] . \tag{3.38d}$$

The γ from the local field model of Sec. 3.2 is

$$\gamma = \frac{64\pi}{3} .$$

Susceptibilities from these charge distributions are compared in Table 3.1, where (3.24, 3.38) are used and we set $\eta = \infty$.

B. End Spring and Interaction Energy

By Gauss' law, we know that the total charge at each end due to displacement of the tie points is (Fig. 3.3a)

$$Q_e = \pm\int_{\text{surface}} \vec{M}\cdot d\vec{s} = \pm 2M_s x_2 d.$$

Let this charge be spread over the end and the four sides within a distance d/2 from the end (total area $3d^2$). We find the self-energy of this charge when it is distributed on a sphere of area $3d^2$, which then has a radius $r = \sqrt{\frac{3}{4\pi}}\, d$. The self-energy of both ends is

Table 3.1. Susceptibilities in homogeneous driving for different transverse magnetizations.

	Local	Non-Local			
$\frac{L}{d}$	χ'	χ'_w	χ'_{2s}	χ'_{4s}	χ'_c
25.9	26.7	13.46	18.0	19.45	19.18
51.5	105.5	43.6	55.0	58.3	57.7
60.6	146.1	57.9	72.2	76.4	75.6
71.9	205.7	78.1	96.5	101.7	100.7
101.0	405.9	142.5	172.8	181.3	179.7

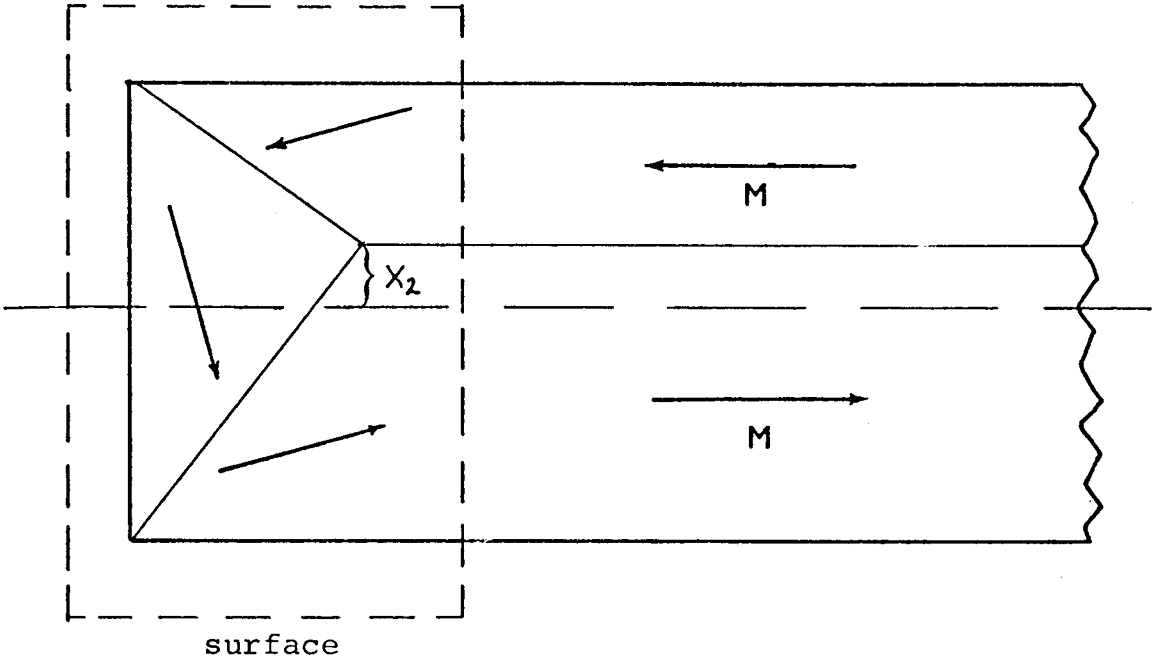

(a)

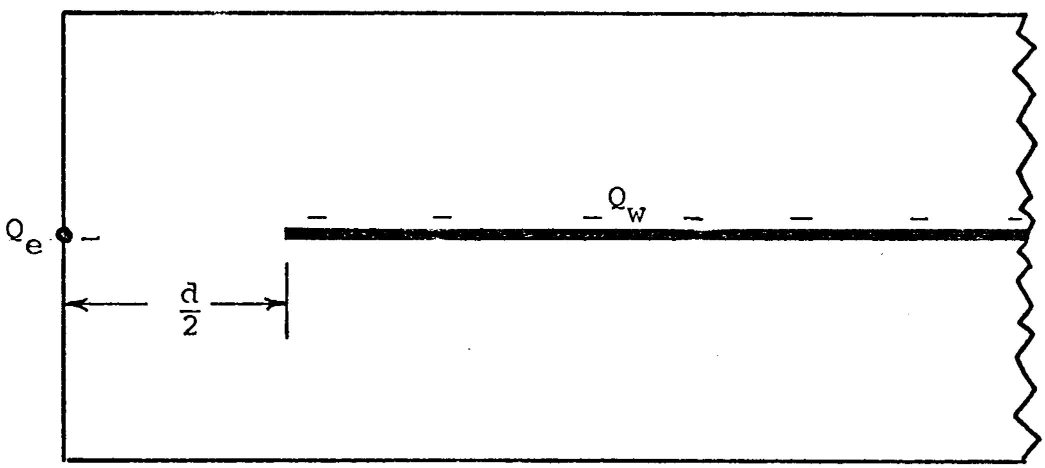

(b)

Fig. 3.3. (a) Gaussian surface for finding charge on the end spring due to displacement x_2 of tie point. (b) Diagram for approximating end spring energy and interaction energy of end spring with long wall.

$$E_d' = 2 \cdot \frac{Q_e^2}{2r} = \tfrac{1}{2}\eta M_s^2 d x_2^2$$

where $\eta \approx 16$. It will be convenient to rewrite this as

$$E_d' = \tfrac{1}{2}\gamma_2 \frac{M_s^2 d^2}{L} x_2^2 \quad , \ \gamma_2 \approx 16\,\frac{L}{2}\,. \tag{3.39}$$

There is also an interaction energy E_d'' between the charges on the end and those due to bowing of the long wall. To find this crudely, we center the sphere of charge at the end of the whisker and put the bowing charges on a line down the center of the whisker which ends at the pinning point, a distance $\frac{d}{2}$ from the effective end charges (Fig. 3.3b). For the bowing charges, $|dQ_w| = \dfrac{16M_s dx_1 zdz}{L^2}$ and

$$E_d'' = 2\int_{-L/2}^{L/2 - \frac{d}{2}} \frac{Q_e dQ_w}{\frac{L}{2} - z}$$

$$= \frac{32M_s^2 d^2}{L} x_1 x_2 \int_{-1}^{1-\frac{d}{L}} \frac{zdz}{1-z}$$

$$= k_3 x_1 x_2 \tag{3.40}$$

where $k_3 = \gamma_3 \dfrac{M_s^2 d^2}{L}$, $\gamma_3 = 32\left(\ln \dfrac{2L}{d} - 2\right)$.

With the assumption that the charges are on the four surfaces, the demagnetizing energy can be written

$$E_d = \tfrac{1}{2}k_1 x_1^2 + \tfrac{1}{2}k_2 x_2^2 + k_3 x_1 x_2 \tag{3.41}$$

where $k_1 = \gamma_{4s} \dfrac{M_s^2 d^2}{L}$. The magnetizing energy is again

$$E_m = -h\left(x_1 + \frac{3}{2}x_2\right). \tag{3.42}$$

Minimization of the total energy with respect to x_1 and x_2 gives

$$x_1 = \frac{k_2 - \frac{3}{2}k_3}{k_1 k_2 - k_3^2} h \quad \text{and} \quad x_2 = \frac{\frac{3}{2}k_1 - k_3}{k_1 k_2 - k_3^2} h. \tag{3.43}$$

At $H_o = H_d$, $x_T(0) = x_1 + x_2 = \frac{d}{2}$. Then

$$\frac{M_s d}{H_d L} = \frac{4\gamma_1 + \frac{8}{3}\gamma_2 - \frac{20}{3}\gamma_3}{\gamma_1\gamma_2 - \gamma_3^2}\frac{L}{d}. \tag{3.44}$$

We compare this with (3.21), which is the limit of (3.44) where $\gamma_3 \to 0$ (no interaction):

$$\frac{M_s d}{H_d L} = \left(\frac{8}{3\gamma_1} + \frac{4}{\gamma_2}\right)\frac{L}{d} \tag{3.45}$$

and with the one-spring model where both $\gamma_2 \to \infty$ and $\gamma_3 \to 0$:

$$\frac{M_s d}{H_d L} = \frac{8}{3\gamma_1}\frac{L}{d}. \tag{3.46}$$

These values are compared in Tables 3.2a, b with the results of Chapter 5, which are written as $\frac{\langle M(0)\rangle}{H_o}\frac{d}{L}$, and with the corresponding experimental value $\frac{\varepsilon_p}{\varepsilon_c}\frac{N_c A_c}{4\pi N_p dL}$ from (2.11). We used $\gamma_1 = \gamma_{4s}$. Comparison of experiment with the theory of Chapter 5 was given in Fig. 2.4.

The relative magnitudes of these "susceptibilities" can be easily understood. The one-spring model should have the

Table 3.2a

L(cm)	$\chi'\frac{d}{L} = \frac{M_s d}{H_d L}$ 1-spring from (3.46)	$\chi'\frac{d}{L} = \frac{M_s d}{H_d L}$ 2-spring Non-interacting from (3.45)	$\chi'\frac{d}{L} = \frac{M_s d}{H_d L}$ 2-spring Interacting from (3.44)	$\chi'\frac{d}{L} = \frac{\langle M(0)\rangle}{H_o}\frac{d}{L}$	$\chi'\frac{d}{L} = \frac{\varepsilon_p}{\varepsilon_c}\frac{N_c A_c}{4\pi N_p L d}$
1.468	1.80	2.05	1.84	1.74	1.71
1.047	1.42	1.67	1.46	1.37	1.42
.881	1.26	1.51	1.30	1.22	1.27
.746	1.13	1.38	1.18	1.09	1.11
.376	.75	1.00	.80	.715	.705

Susceptibilities in homogeneous driving: theories and experiment. In the three spring model (energy) calculations, the charge is assumed to be on the surface: $\gamma = \gamma_{4s}$ (3.38c).

Table 3.2 b

$$\left(\xi = \left\langle \frac{M(o)}{H_o} \right\rangle \frac{d}{L} \right)$$

L(cm)	$\frac{M_s}{H_d} \frac{d}{L} \Big/ \xi$ 1-spring	2-spring Non-interacting	2-spring Interacting	$\frac{\varepsilon_p}{\varepsilon_c} \frac{N_c A_c}{4\pi N_p L d} \Big/ \xi$
1.468	1.035	1.175	1.055	.98
1.047	1.035	1.22	1.065	1.035
.881	1.03	1.24	1.065	1.04
.746	1.035	1.27	1.08	1.02
.376	1.05	1.40	1.12	.985

Susceptibilities in homogeneous driving: ratio of spring model and experimental values to the theoretical values of Chapter 5.

least susceptibility, and the two-spring non-interacting one should have the largest value, because it permits deflection at the ends as well. The model with an interaction energy added should have an intermediate value. From Table 3.2a, we see that the interaction energy is relatively large, the susceptibility being only slightly greater than for the pinned-end model.

We conclude that the 1-spring model gives a good approximation to the demagnetizing energy and hence to χ'. A large interaction term must be included when the end springs are added. This interaction energy drives the susceptibility back to near the 1-spring value. Hence Table 3.1 was constructed using the simple case of $\gamma_2 = \infty$ and $\gamma_3 = 0$.

The actual χ' ($\propto 1/\gamma$) is an upper bound for the susceptibilities of any set of postulated charge distributions (assuming the demagnetizing energies are accurately found). Thus of these possibilities, reference to Table 3.1 shows that a real whisker is most closely approximated by putting the charge equally on the four surfaces. (The local model result has a greater susceptibility than the non-local values due to neglect of non-local demagnetizing fields.)

In summary, the susceptibility can be accurately calculated using the 1-spring model and assuming the charge is on all four surfaces.

Table 3.3 gives the displacement of the tie points as a fraction of the displacement at the center of the wall, as

L	$\frac{x_2}{x_1 + x_2}$ Non-interacting	Interacting	Quadratic Fit
1.468	.085	.076	.119
1.047	.105	.097	.135
.881	.117	.110	.144
.746	.128	.123	.154
.376	.181	.191	.206

Table 3.3. Relative magnetization (homogeneous driving) at the end of the whisker to that at the center, for non-interacting springs (from (3.43) with K_3=0), interacting springs (from (3.43) with K_3 given in (3.40)), and best quadratic fit to theory of Chapter 5.

predicted by the two models here. Also shown for comparison are the values found from the best quadratic fit to the magnetization calculated in Chapter 5.

The 2-spring models attempt to treat the actual departure from linearity of the charge density along the whisker as being concentrated entirely at the end, giving rise to the second spring and interaction energies. The results of Chapter 5 indicate that for a self-consistent solution, the extra charge on the end must be spread along more of the whisker.

The most impressive thing about these models is that there are no adjustable parameters. Susceptibilities are found which agree with experiment within 5 percent, based on the assumption of a parabolic magnetization. An assumed magnetization which is not too far from micromagnetic equilibrium can give good results for the energy, because at equilibrium the variation of the energy is of second order when the variation of $\vec{M}$ is of first order. We have assumed various magnetization configurations, giving different charge distributions. Those configurations which are "close" to equilibrium give excellent results for the energies (and hence susceptibility). However, comparison of the energies does not give much information about the true $\vec{M}$. To find $\vec{M}$ we must minimize (to zero) the torques on the atomic moments.

3.3.2 Local Driving

We found in Sec. 3.2 that the local model predicted a triangular-shaped wall for local driving, with $\gamma^L = 16$. From experiment, the wall is nearly this shape. In Appendix 1C, the actual demagnetizing energy (non-local) for a triangular wall is calculated for the case of charges on the surface of a cylinder. We find

$$E_d = \tfrac{1}{2}\gamma_c^L \frac{M_s^{\,2}d^2}{L} x_1^2 , \tag{3.47}$$

where $\gamma_c^L = 32\left[\ln \frac{\sqrt{\pi}L}{2d} - 1 + \frac{12d}{\pi^{3/2}L}\right]$.

By comparing γ_c^L with γ_c (for the homogeneous driving), we find

$$\frac{\gamma_c}{\gamma_c^L} \approx \frac{4}{3}$$

to within one percent, for $\frac{L}{d} \gtrsim 30$. This would be expected if the susceptibility in homogeneous driving for both triangular and quadratic walls is nearly equal, because the ratio of areas, and hence magnetizing energy, is also 4/3. On energy considerations alone, in homogeneous driving a triangular response of the magnetization should be as favorable as the actual quadratic bowing of the wall. This emphasizes the point made in the last section that different magnetizations which are not "too far" from micromagnetic equilibrium have nearly identical susceptibilities.

It is interesting that the local model also predicts

$$\frac{\gamma}{\gamma^L} = \frac{\frac{64}{3}\pi}{16\pi} = \frac{4}{3} \quad .$$

The magnitude of each of these quantities is incorrect (by a factor of about 2) but the relative sizes seem to be accurate for different wall shapes.

In local driving, only the deflection at the center determines the magnetizing energy. The wall shape just minimizes the demagnetizing energy for a given center deflection. The triangular wall has only 3/4 the demagnetizing energy of the quadratic wall for the same center deflection, so the former will clearly be favored. The actual shape of the wall is found, from the self-consistent field approach of Chapter 5, to be very sensitive to the radius of the driving coil (Fig. 5.6).

Although we can't distinguish well between different wall shapes from these energy calculations, we have seen that minimization of magnetostatic energy requires the charge to be at the surface. That the charge is in fact at the surface (because of the low crystalline-anisotropy of iron) will be shown in the next chapter).

CHAPTER 4

THE TRANSVERSE MAGNETIZATION

In this chapter it is shown that in a long whisker the transverse and longitudinal magnetization can be solved for separately. In Sec. 4.1.1 a simple functional form for the transverse magnetization is assumed and the parameters in the expression are evaluated. In Sec. 4.1.2 the micromagnetic equations are reduced to a set of coupled linear algebraic equations and solved numerically. Most of the magnetic charge is found to be on the whisker surface, with very little on the 180° wall and virtually none within the domain volume. In Sec. 4.1.3 it is assumed that the volume charge is zero and a more accurate calculation of the surface charge distribution is presented.

Contributions to the magnetic energy of the entire whisker are calculated in Sec. 4.2. Neglect of wall energy and exchange energy within the long domains is justified, and it is shown that the anisotropy energy within the long domains lowers the whisker susceptibility about a percent below the magnetostatic result found in Sec. 3.3.

The similarity of the iron whisker to a medium of infinite magnetic susceptibility is established in Sec. 4.3, and the result is used in Chapter 5 to calculate the longitudinal magnetization (i.e., the shape of the long 180° wall).

4.1 Micromagnetic Theory: The Torque Equation

It was shown in Chapter 1 that the distribution of magnetization can be found in two equivalent ways: (i) varying $\vec{M}$ to minimize the "energy", or (ii) varying $\vec{M}$ until the "field" is parallel to $\vec{M}$ everywhere. In this section, we adopt the latter method. We first discuss self-consistent fields and a simple analytical model for the whisker. The micromagnetic equations are then set up in integral form and solved numerically.

4.1.1 Self-consistent Fields

We will find the transverse magnetization in a long whisker ($L >> d$) when a longitudinal field $H_o\hat{z}$ is applied. We start by assuming the existence of the 180° wall and the closure domains in zero applied field ($H_o = 0$). In this configuration there is no demagnetizing field $\vec{H}'$ and the torque equation $\vec{M} \times \vec{H}_T = 0$ (where $\vec{H}_T = \vec{H}_o + \vec{H}' + \vec{H}_k + \vec{H}_{ex}$) is satisfied by the competition between the anisotropy field $\vec{H}_k$ and the exchange field $\vec{H}_{ex}$ within the domain walls. This competition is unaffected by the displacement of the wall in an applied field. We need consider only the effects of $\vec{H}_o$, $\vec{H}'$, and $\vec{H}_k$ within the domains themselves. The magnetization within a domain varies slowly enough that $\vec{H}_{ex}$ is negligible there.

The simplest magnetization distribution which approximates the whisker is shown in Fig. 4.1. The origin of the coordinate system is at the center of the whisker. The angles are greatly exaggerated for clarity. Throughout this section the wall is assumed to be in the center ($x = 0$) to simplify the calculation. (The wall is near the center only for the initial magnetization ($H_o \ll H_d$), but our conclusions will be valid for all $H_o < H_d$). The magnetization is assumed to rotate uniformly from the center to the sides, giving rise to + and - contributions to the uniform volume charge from the derivatives of x and y angles, respectively. It will be seen that this is a fairly good approximation.

The magnetic charge for this approximate solution is found from

$$\rho = -\vec{\nabla}\cdot\vec{M} = -\frac{\partial M_x}{\partial x} - \frac{\partial M_y}{\partial y} \equiv \rho_x + \rho_y,$$

which gives for small angles ($\phi_3 \sim \phi_2 < \phi_1 < \theta \ll 1$) the volume charge densities

$$\rho_x = \frac{M_s(\phi_1 - \phi_2)}{d/2} \tag{4.1a}$$

and

$$\rho_y = \frac{M_s(-\phi_3)}{d/2} \quad , \tag{4.1b}$$

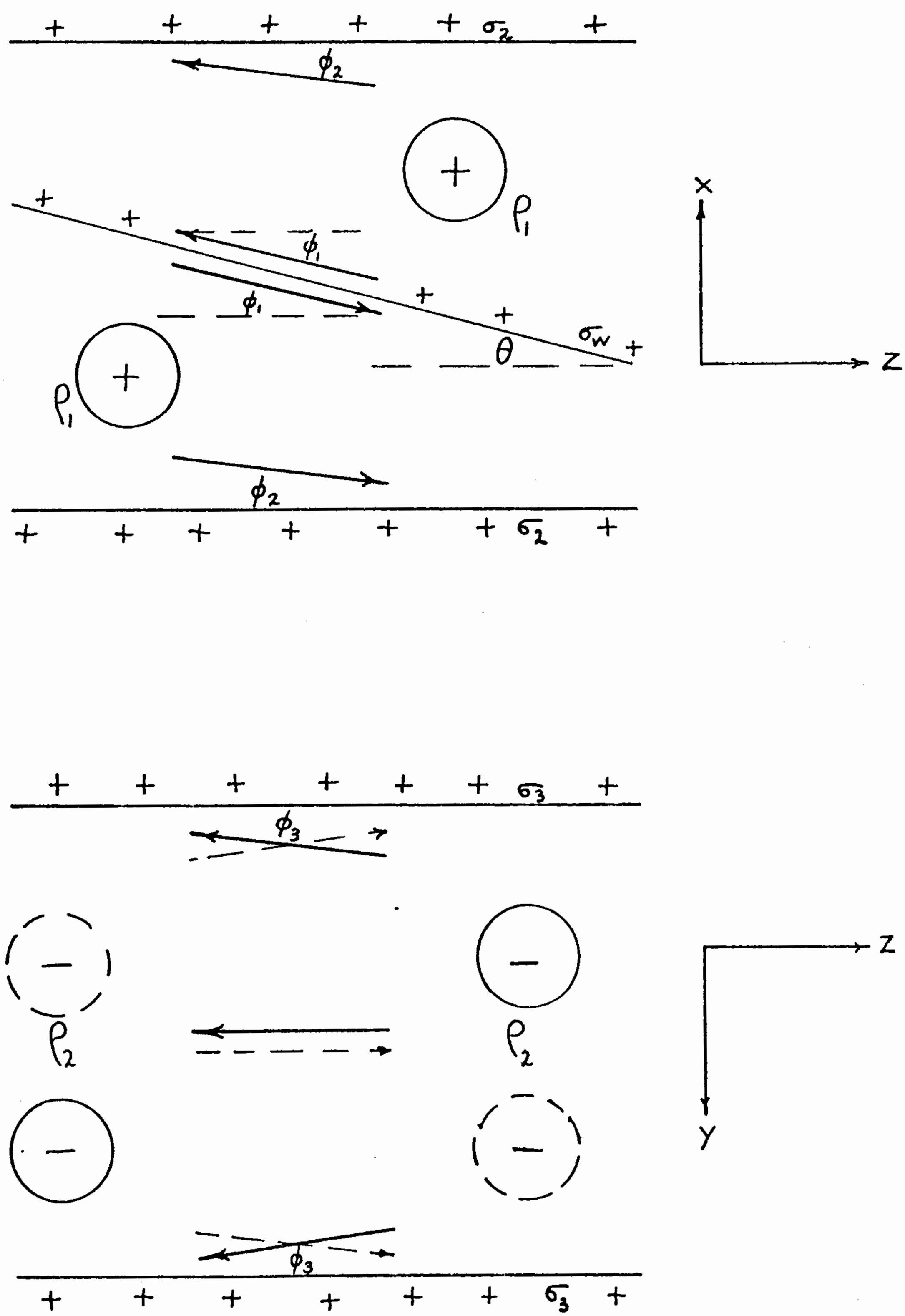

Fig. 4.1. Charge densities ($\sigma_w, \sigma_2, \sigma_3, \rho_1, \rho_2$), magnetization angles (ϕ_1, ϕ_2, ϕ_3), and wall angle θ in approximate configuration for long domains separated by 180° wall. Volume charge is assumed to be uniform; actual volume charge is $\rho = \rho_1 + \rho_2$. Dotted arrows in y-z projection indicate magnetization on far side of Bloch wall.

and the surface charge densities

$$\sigma_W = 2M_s(\theta - \phi_1), \tag{4.1c}$$

$$\sigma_2 = M_s\phi_2, \tag{4.1d}$$

and

$$\sigma_3 = M_s\phi_3 \quad . \tag{4.1e}$$

The transverse demagnetizing fields are found from these charge distributions.

A. Separation of the Problem

At any point z along the whisker, the wall makes an angle $\theta(z)$ which results in a total charge/unit length $\rho_\ell \propto \theta(z)$ (Sec. 3.1). This angle is slowly varying over distances (in the z direction) comparable to d. Because the transverse fields fall off rapidly as $\frac{1}{z^2}\ \frac{1}{z}$, they can be equivalently calculated from an infinitely long bar with the same charge distribution in cross-section, but uniform charge/unit length in the z direction given by ρ_ℓ above. This equivalence is further aided by the fact that first order deviations in $\theta(z)$ on each side of the point in question give transverse fields which tend to cancel, being positive from one side and negative from the other.

In a whisker cross-section at any point z, the demagnetizing fields, and hence transverse magnetization, vary linearly with $\theta(z)$, but do not otherwise depend on z. Thus, the total amount of charge in the x-y cross-section scales linearly with $\Theta(z)$, and the distribution of this charge, which is determined by the demagnetizing fields (and the crystalline anisotropy), is independent of z. Note, however, that very near the ends of the long domain wall the approximations made here are of limited validity.

The three-dimensional problem thus separates into a two-dimensional (x-y) and a one-dimensional (z) problem. As the separation is valid everywhere except near the ends, it is a good approximation for long whiskers. The longitudinal problem is to find x(z), the shape of the wall, and is studied in Chapter 5.

B. Self-consistency at the Wall

At the wall, the angle of $\vec{M}$ with the z-axis, ϕ_1, can be immediately found. By symmetry, the only demagnetizing field acting on these spins is due to the charge on the wall itself. Fig. 4.2 shows the fields. $\vec{M}$ points in the direction of the sum of anisotropy and demagnetizing fields. For small angles and using (4.1c),

$$\phi_1 \cong \frac{2\pi\sigma_W}{H_A} = \frac{4\pi M_S(\theta-\phi_1)}{H_A} \quad .$$

Defining

$$\Phi_1 \equiv \frac{\phi_1}{\theta} \qquad \text{and} \qquad R \equiv \frac{H_A}{4\pi M_S} \approx \frac{500}{21{,}000}$$

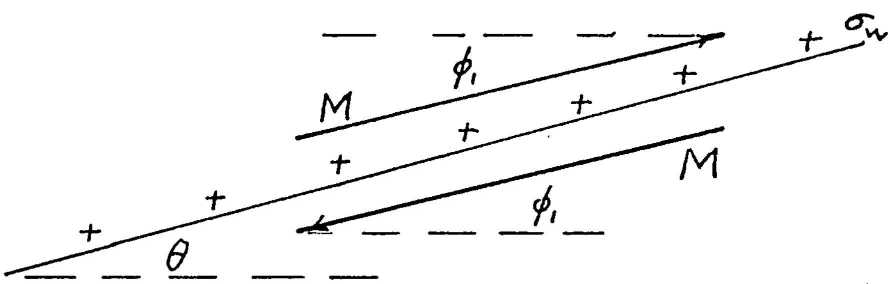

(a)

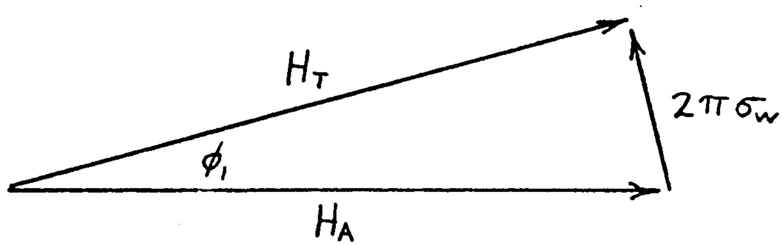

(b)

Fig. 4.2. (a) Magnetization and charge at the wall--definition of magnetization and wall angles. (b) Self-consistency condition at the wall.

we find

$$\Phi_1 = \frac{1}{1+R} \quad , \tag{4.2}$$

and the fractional charge on the wall is

$$1 - \Phi_1 = \frac{R}{1+R} = .023.$$

Only 2.3% of the charge is on the wall.

This result also applies when the wall is not in the center of the whisker, where there is an added transverse demagnetizing field. In the small angle approximation, this extra field rotates the spins on one side into the wall, and on the other side an equal amount away from the wall. The net flux of $\vec{M}$ into the wall (and hence the charge on the wall) does not change.

C. Simple Model

As a first attempt to find the transverse magnetization (and distribution of magnetic charge), we assume a solution to (1.15) of the form (Fig. 4.1)

$$M_x(x) = \begin{cases} M_s\theta\left[\Phi_1 - (\Phi_1 - \Phi_2)\frac{2x}{d}\right], & 0 < x \le \frac{d}{2} \\ -M_s\theta\left[\Phi_1 - (\Phi_1 - \Phi_2)\frac{2x}{d}\right], & -\frac{d}{2} \le x < 0 \end{cases} \tag{4.3}$$

$$M_y(y) = M_s\theta\Phi_3\frac{2y}{d} \quad , \qquad -\frac{d}{2} \le y \le \frac{d}{2}$$

where Φ_1 is known from (4.2) and Φ_2 and Φ_3 are the constants to be determined. This magnetization creates uniform volume charge densities due to both $\frac{\partial M_x}{\partial x}$ and $\frac{\partial M_y}{\partial y}$. In Appendix 2 the fields perpendicular to the surface from the volume, wall, and surface charges are evaluated at two points: $(x,y) = \left(\frac{d}{2}, 0\right)$ and $\left(\delta, \frac{d}{2}\right)$. δ is any non-zero distance less than $\frac{d}{2}$. In the small angle approximation, the self-consistency condition (1.11)

$$\vec{M} \times (\vec{H}_o + \vec{H}' + \vec{H}_k) = 0$$

is equivalent to setting the transverse demagnetizing fields at these two points proportional to the x-angle (ϕ_2) and y-angle (ϕ_3), respectively. These two equations are solved in Appendix 2 for the unknown angles ϕ_2 and ϕ_3, and the results are given in Table 4.1.

The y-field is evaluated at $(x = \delta,\ y = \frac{d}{2})$ in order to avoid the logarithmic singularity in the y-field at the wall ($x = 0$) due to the wall charge. (The field tangential to a charged plate is infinite at the edge of the plate.) The solutions are thus finite and fairly independent of δ (Table 4.1).

In the limit of vanishing $R = \frac{H_A}{4\pi M_s}$, which can be observed experimentally at high temperatures, the transverse demagnetizing fields must also vanish. The solution for the

Table 4.1

Charge Distribution Within The Whisker

	R	Fraction of Charge			
		Volume	Wall	Surface // Wall	Surface ⊥ Wall
Exact Solution	0	0	0	.5	.5
Approximate Solution $\delta = .1$	0	.0803	0	.4599	.4599
	.023	.0726	.0229	.4481	.4565
	.23	.0228	.1927	.3657	.4187
	2.3	-.0379	.7048	.1391	.1939
	23	-.0088	.9598	.0199	.0291
Approximate Solution $\delta = .25$	0	.0803	0	.4599	.4599
	.023	.0781	.0229	.4506	.4485
	.23	.0619	.1927	.3794	.3660
	2.3	.0195	.7048	.1448	.1310
	23	.0024	.9598	.0201	.0178
Accurate Numerical Solution from Sec. 4.1.3*	.0233	0	.0229	.4863	.4908
	.233	0	.1896	.3944	.4160
	2.33	0	.7006	.1378	.1617
	23.3	0	.9590	.0184	.0226

* Volume charge assumed to be zero.

transverse charge distribution becomes identical to the two-dimensional solution for the charge on an infinitely long metal bar with

$$\rho_{\ell} = \text{charge/unit length} = 2M_s\theta \ .$$

In a metal bar, the charges arrange themselves on the surface to give zero electric field everywhere inside. This analogy of electric charges on a metal bar will prove useful for all aspects of the iron whisker in a magnetic field.

In the limit as $R \to 0$, the exact solution would have all charge on the surface. Our simple calculation gives about 92 percent on the surface and 8 percent in the volume. It is the difference between the charge distributions calculated for $R = 0$ and $R = .023$ which is meaningful (see also Sec. 4.1.3 and entry at bottom of Table 4.1). This difference is 2.3% on the wall and less than a percent (of negative charge!) in the volume. Thus, we can conclude even from this simple model that about 98% of the charge is on the surface for these iron whiskers at room temperature.

4.1.2 The Two-dimensional Solution

For a more rigorous calculation of the transverse magnetization, but still under the approximation that the charge per unit length is constant along the whisker, one generalizes the fractional angles Φ_1, Φ_2 and Φ_3 to continuous variables

$\Phi_x(x,y)$ and $\Phi_y(x,y)$. One neglects difference between $\Phi(x,y)$ and $\sin\Phi(x,y)$ to linearize the self-consistency equations (1.20). Neglecting the terms on the LHS and writing the transverse demagnetizing fields in integral form, one gets two coupled integral differential equations:

$$4\pi R\Phi_x(x,y) = \int_{-d/2}^{d/2} dx' \int_{-d/2}^{d/2} dy' K_x(x-x',y-y') \left[- \frac{\partial \Phi_x}{\partial x}(x',y') - \frac{\partial \Phi_y}{\partial y}(x',y') \right] + \int_{-d/2}^{d/2} dy' \Big\{ K_x(x,y-y') \cdot 2(1-\Phi_x(0,y'))$$

$$+ \left[K_x\left(x-\frac{d}{2},y-y'\right) + K_x\left(x+\frac{d}{2},y-y'\right)\right] \Phi_x\left(\frac{d}{2},y'\right) \Big\}$$

$$+ \int_{-d/2}^{d/2} dx' \left[K_x\left(x-x',y-\frac{d}{2}\right) + K_x\left(x-x', y+\frac{d}{2}\right)\right] \Phi_y\left(x',\frac{d}{2}\right) \quad (4.4a)$$

and a similar equation (4.4b) for $4\pi R\Phi_y(x,y)$, where on the RHS only the K_x are replaced by K_y.

$K_x(x-x',y-y')$ is the Green function for the x-component of the field at (x,y) due to an infinite line charge at (x',y'):

$$K_x(x-x',y-y') = \int_{-\infty}^{\infty} dz' \frac{(x-x')}{[z'^2+(x-x')^2+(y-y')^2]^{3/2}}$$

$$= \frac{2(x-x')}{(x-x')^2+(y-y')^2} \quad . \quad (4.5a)$$

Similarly,

$$K_y(x-x',y-y') = \frac{2(y-y')}{(x-x')^2+(y-y')^2} \quad . \quad (4.5b)$$

For example, the demagnetizing field in the x-direction at (x,y) due to a rectangular bar at (x',y'), infinite in the z-direction and of cross section dx'dy', which contains a uniform charge density $\rho(x',y') = -M_s \frac{\partial \phi_x}{\partial x}(x',y')$, is given by

$$K_x(x-x',\ y-y')\left(-M_s\frac{\partial \phi_x}{\partial x}(x',y')\,dx'dy'\right).$$

Division by $M_s\theta$ gives the integrand of the first term of (4.4a) above. Likewise, a segment of surface charge at y_o, infinite in the z-direction and of width dx', with surface charge density

$$\sigma(x',y_o) = M_s\theta\Phi_y(x',y_o)\ ,$$

gives a field in the x-direction at (x,y) of

$$M_s\theta K_x(x-x',\ y-y_o)\Phi_y(x',y_o)\,dx'.$$

In (4.4) we have taken the wall to be in the center (x = 0) for two reasons. First, it gives the basic charge distribution for small fields. Since the wall has only about 2% of the charge, we expect the distribution to be nearly unchanged even for a large bowing of the wall. (The experimental evidence for this is given in Sec. 4.3.) Second, it gives the charge distribution the symmetry of two perpendicular mirror planes intersecting along the z-axis, which simplifies the calculation.

Because (4.4a,b) are valid at every point (x,y), each one constitutes a two-fold infinite set of simultaneous equations. An exact analytic solution of these equations is, to our knowledge, impossible.

An approximate solution, whose accuracy is limited only by the size of an available computer, is found by replacing these integral equations by a set of simultaneous linear equations. A quadrant of the whisker is broken up into an $m \times m$ grid. The volume charge in each grid is approximated by a line charge at the center, and the surface and wall charges are approximated by a line charge at the center of the appropriate grid line. Both the x and y fields from these charges are evaluated (using the above Green functions) at the $(m+1)^2$ intersections of grid lines, and $2(m+1)^2$ equations are formed by setting these fields proportional to the respective x and y angles at these $(m+1)^2$ points. Details of the reduction of (4.4) to algebraic equations are given in Appendix 3.

The resulting transverse magnetization for $m = 10$ is given in Figs. 4.3a, b, c, d, for four different values of R. The most important conclusion is that the volume charge is very near zero (< .5%, which is within the expected error of the program) and this holds for all values of R . When R is large and traps a significant part of the charge on the wall, there still is no significant charge distributed in the volume. The

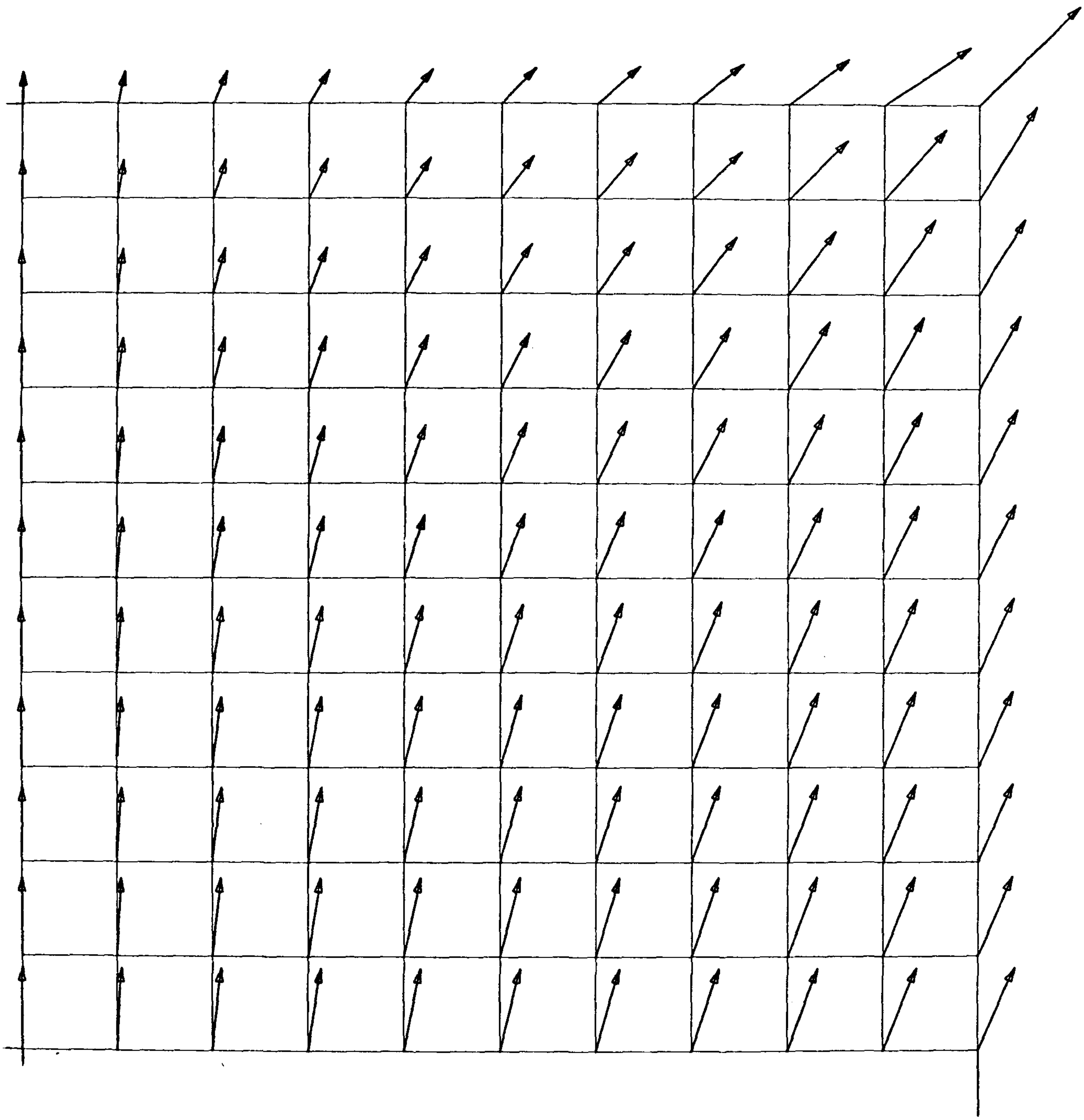

Fig. 4.3a. Transverse magnetization in one quadrant of the whisker, calculated from (4.4) for m = 10 (242 self-consistency conditions). Bloch wall is horizontal line at bottom.
$R = H_A/4\pi M_s = .023$, $\Phi_w = \phi_w/\theta = .977$.

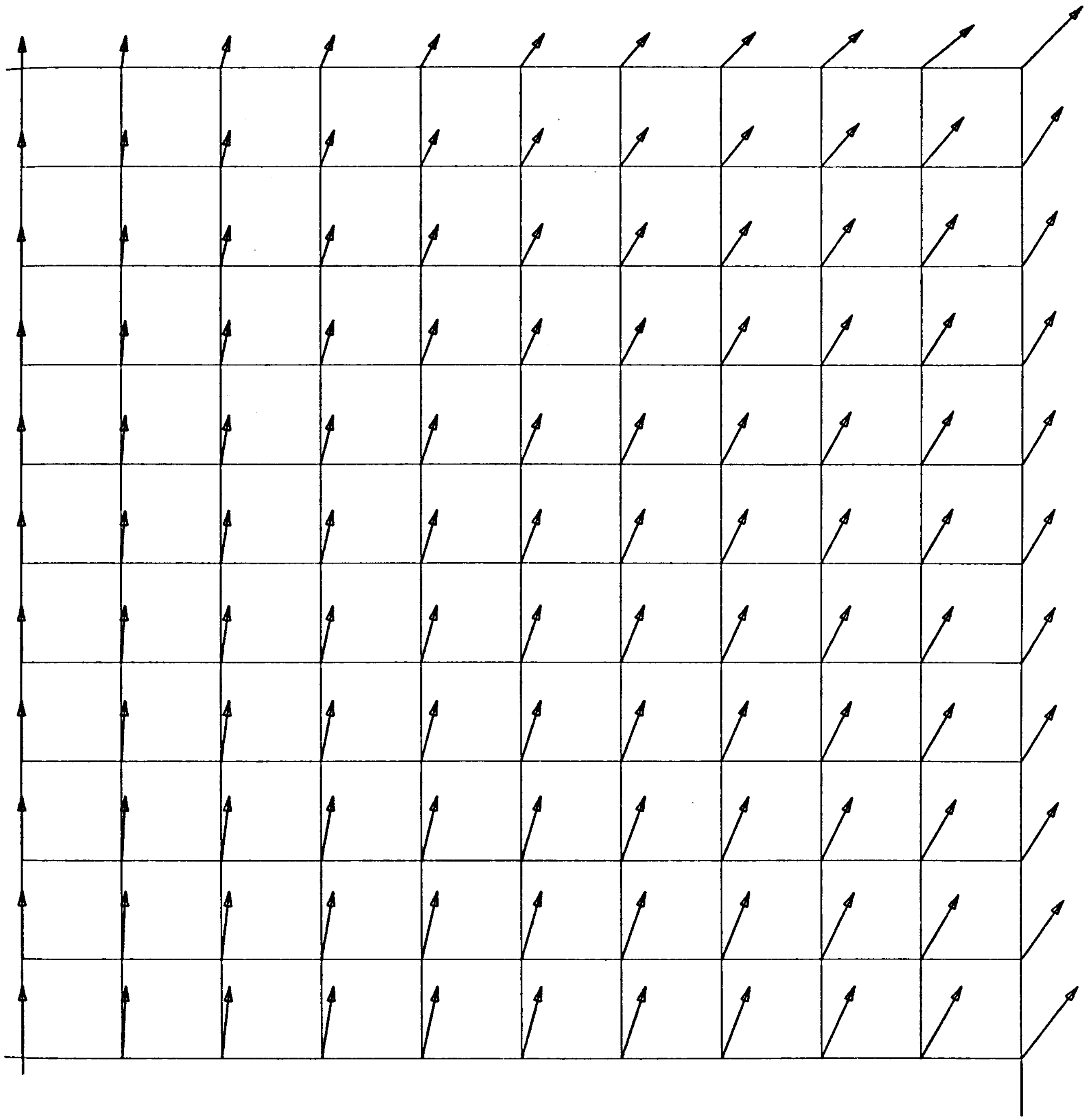

Fig. 4.3b. Transverse Magnetization. R = .23, Φ_W = .813.

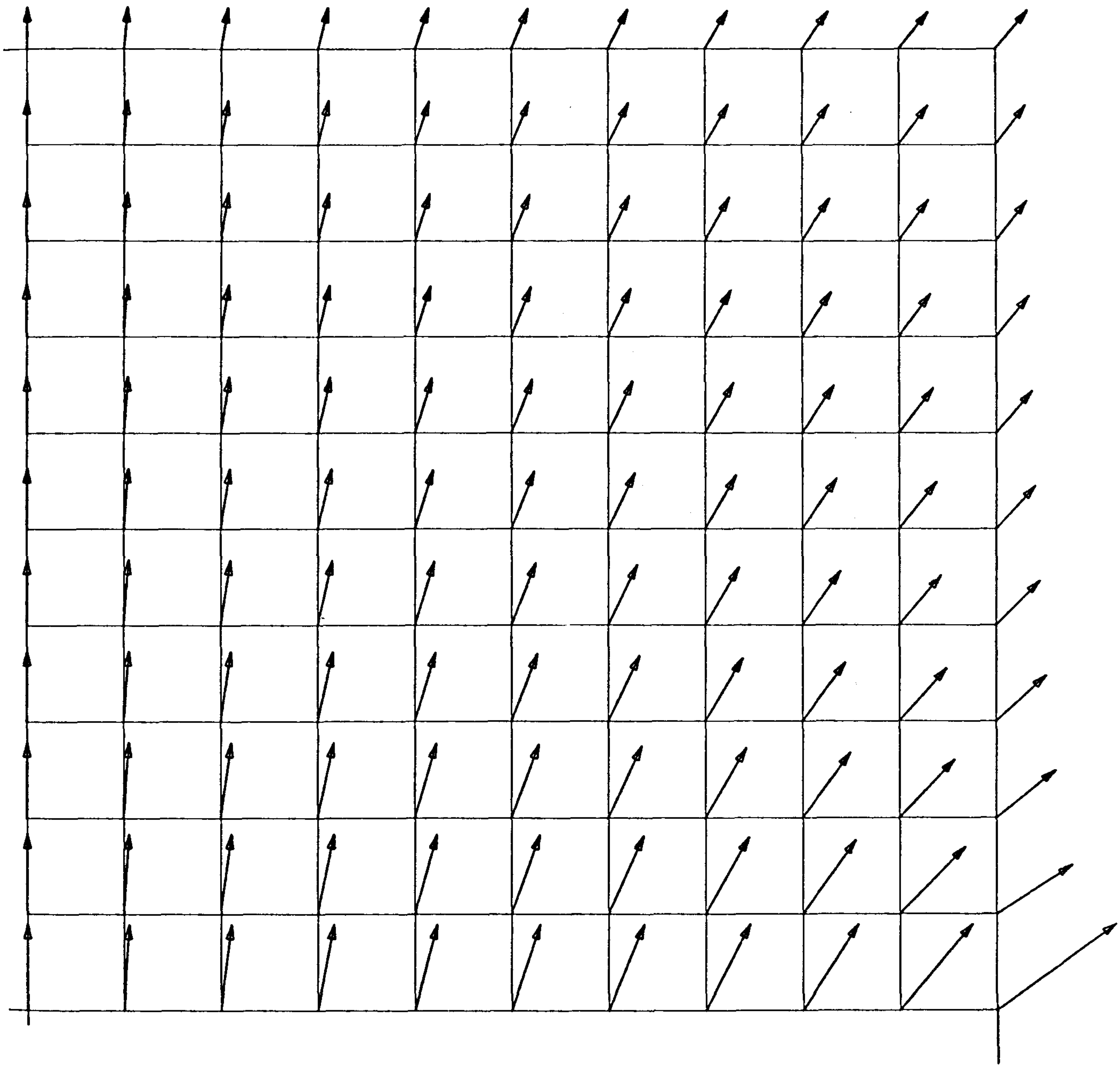

Fig. 4.3c. Transverse Magnetization. $R = 2.3$, $\Phi_w = .303$.

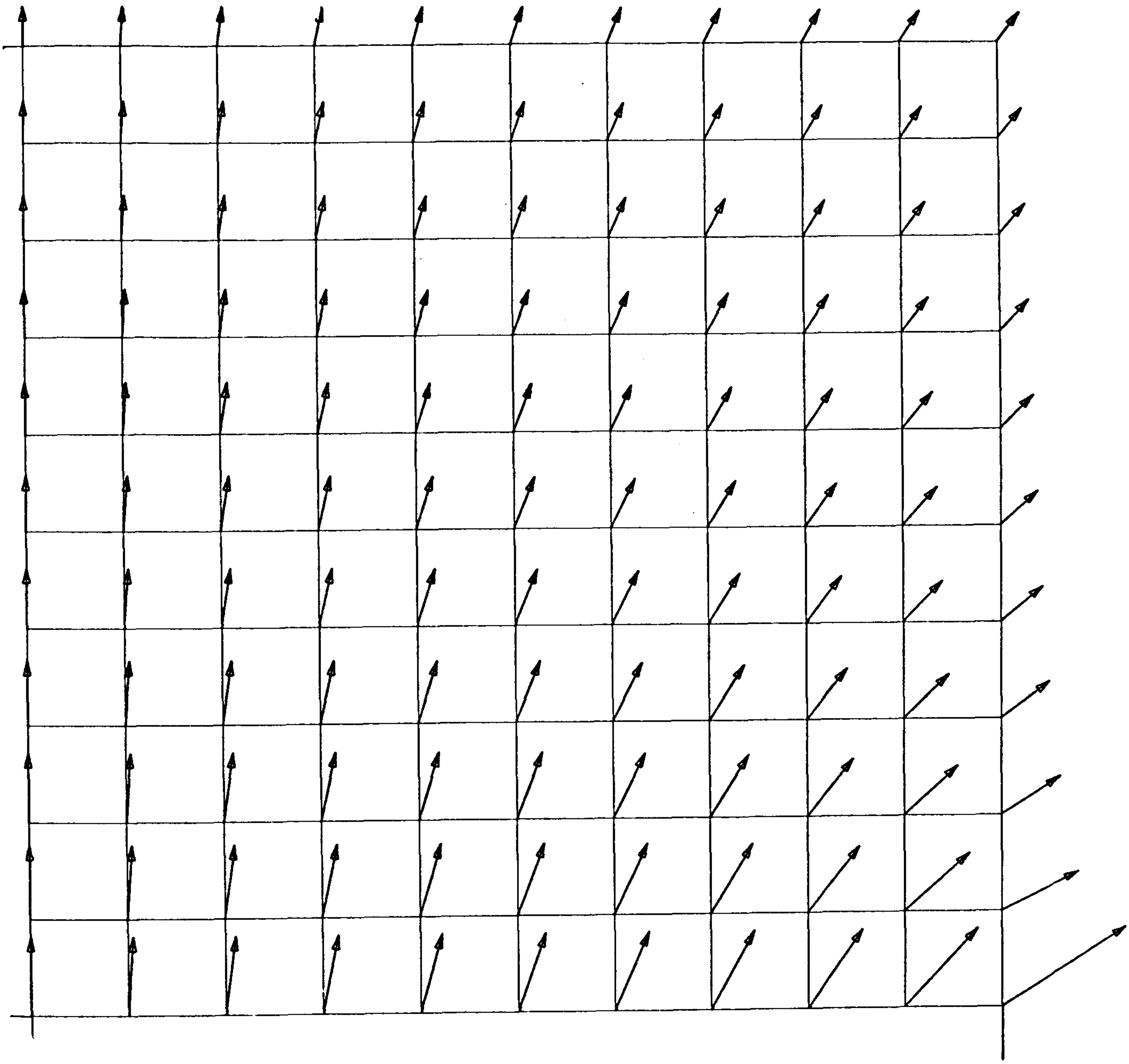

Fig. 4.3d. Transverse Magnetization. R = 23.0, Φ_w = .042.

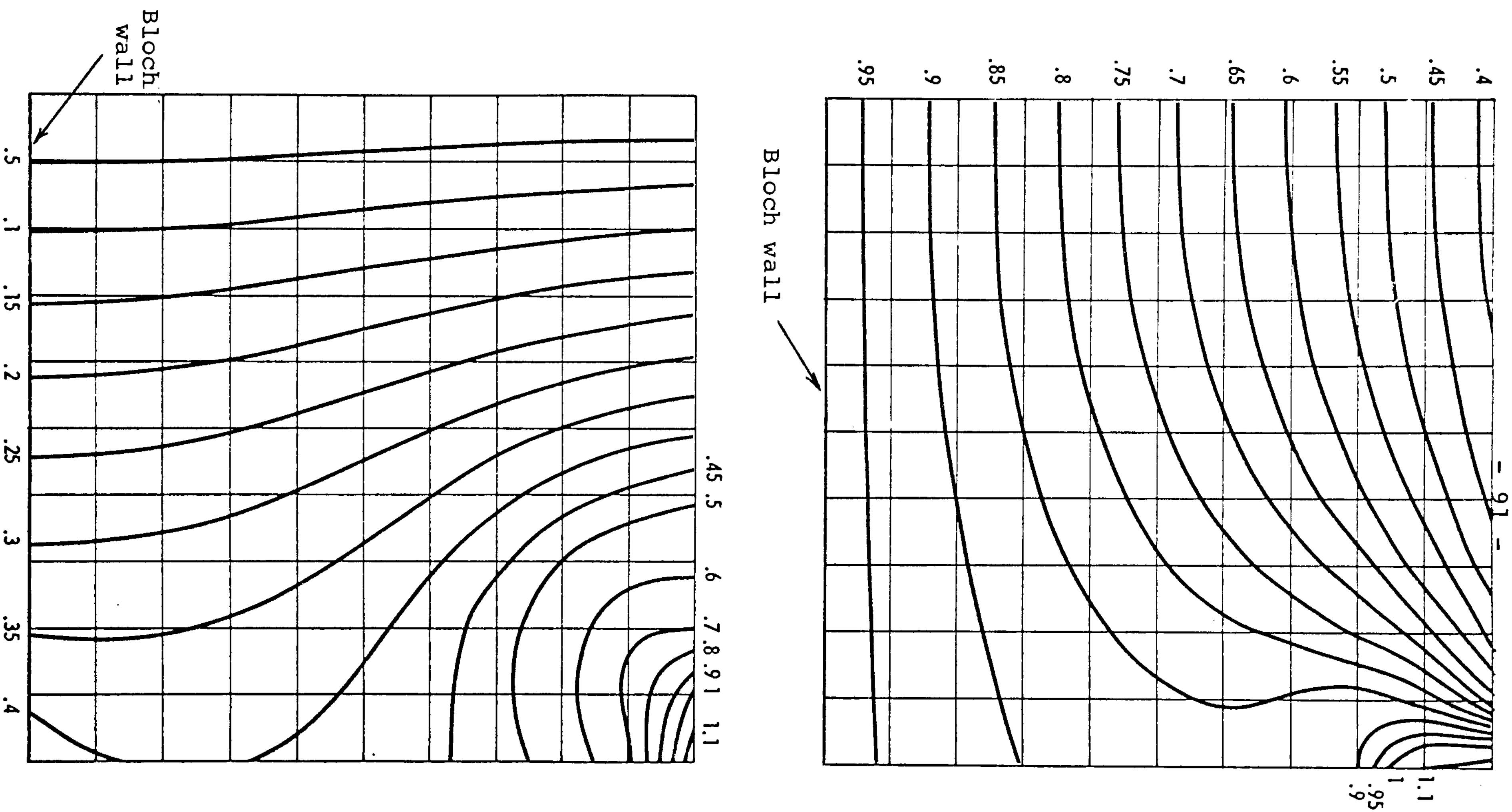

Magnetization parallel to wall

Magnetization perpendicular to wall

Fig. 4.4a. Iso-angle contours for x and y components of magnetization in one quadrant. Bloch wall is horizontal line as shown. $R = .023$, $\Phi_w = .977$.

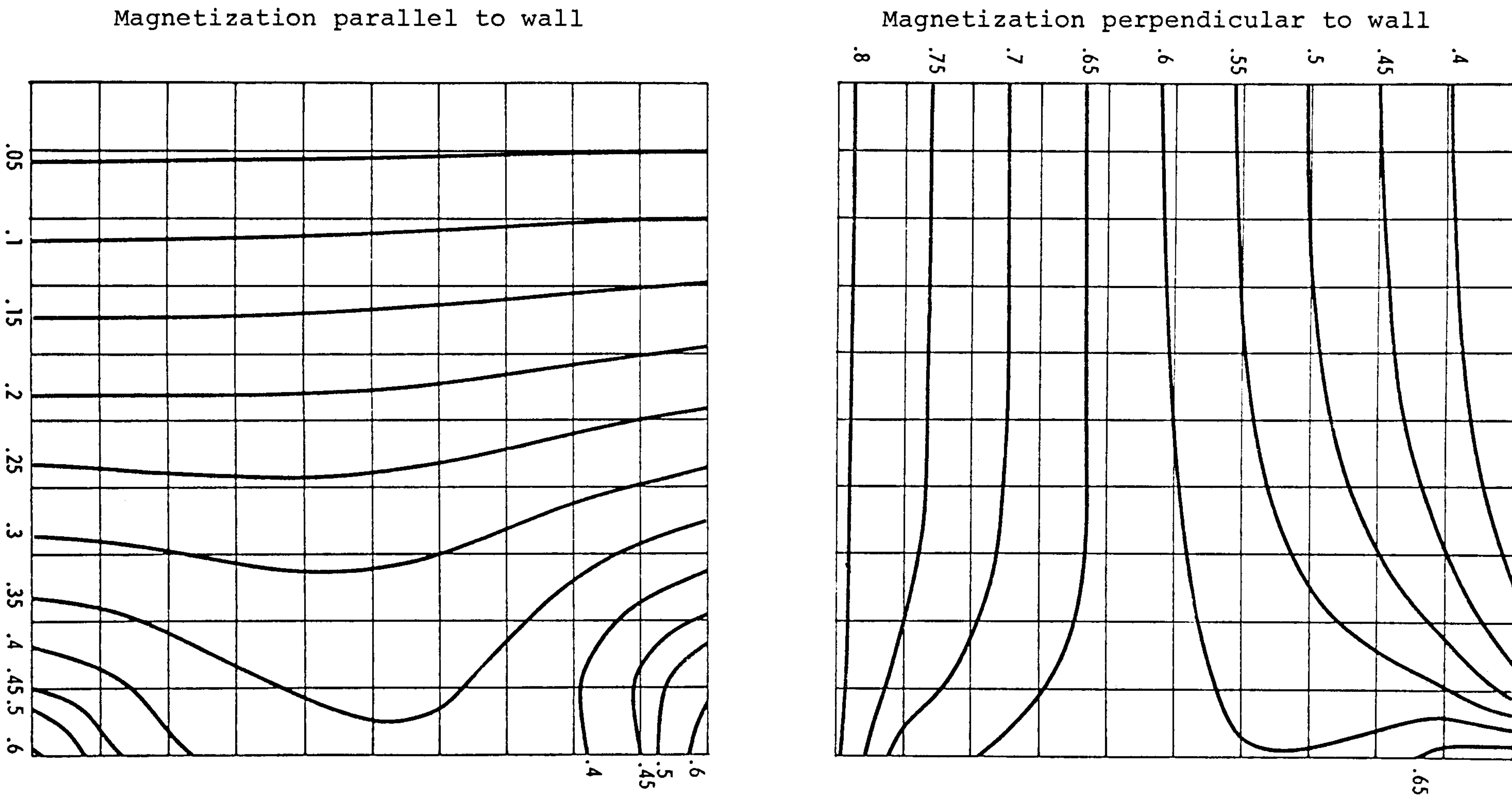

Fig. 4.4b. Iso-angle contours. R = .23, Φ_w = .813.

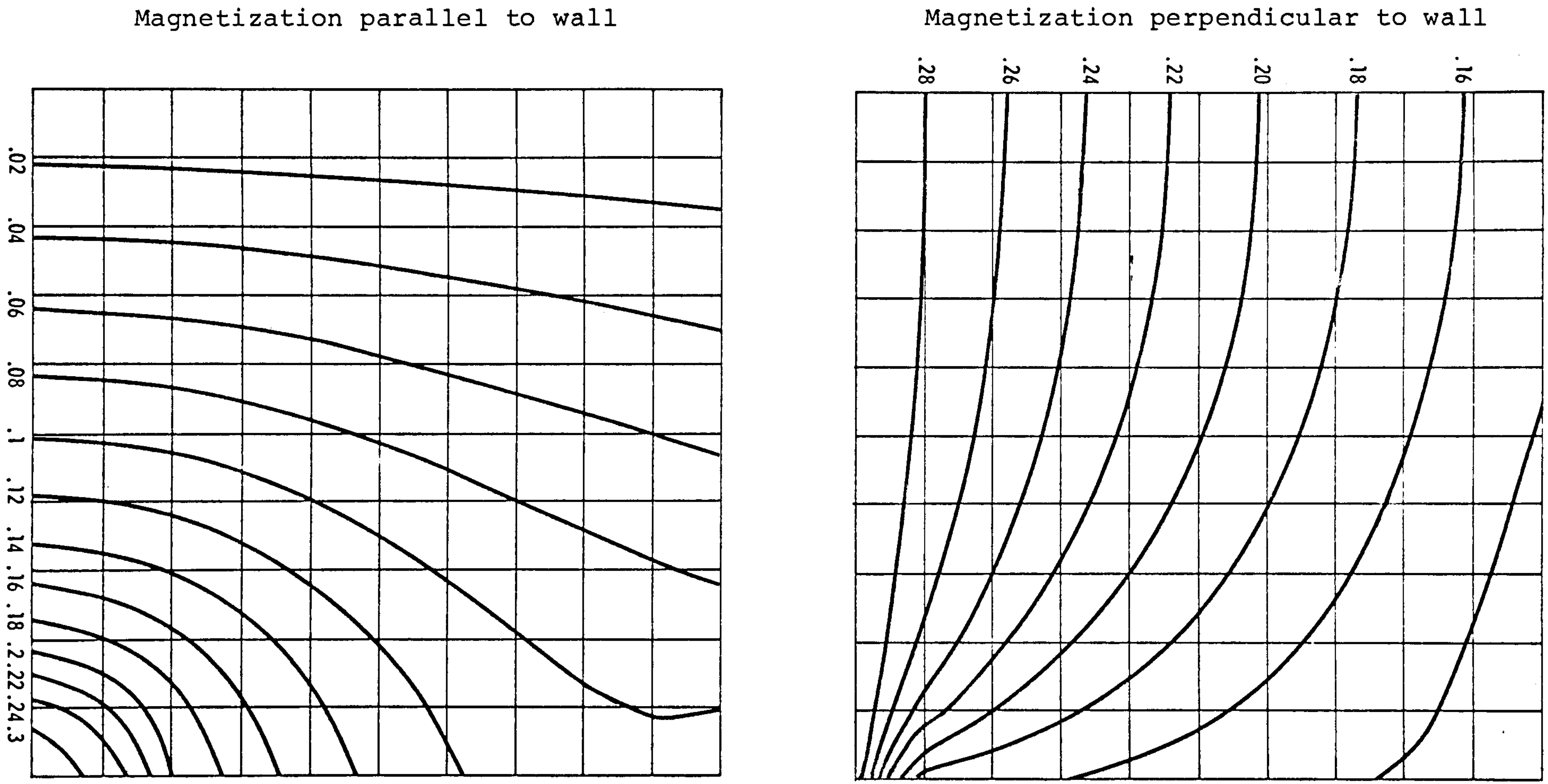

Fig. 4.4c. Iso-angle contours. R = 2.3, $\Phi_w = .303$.

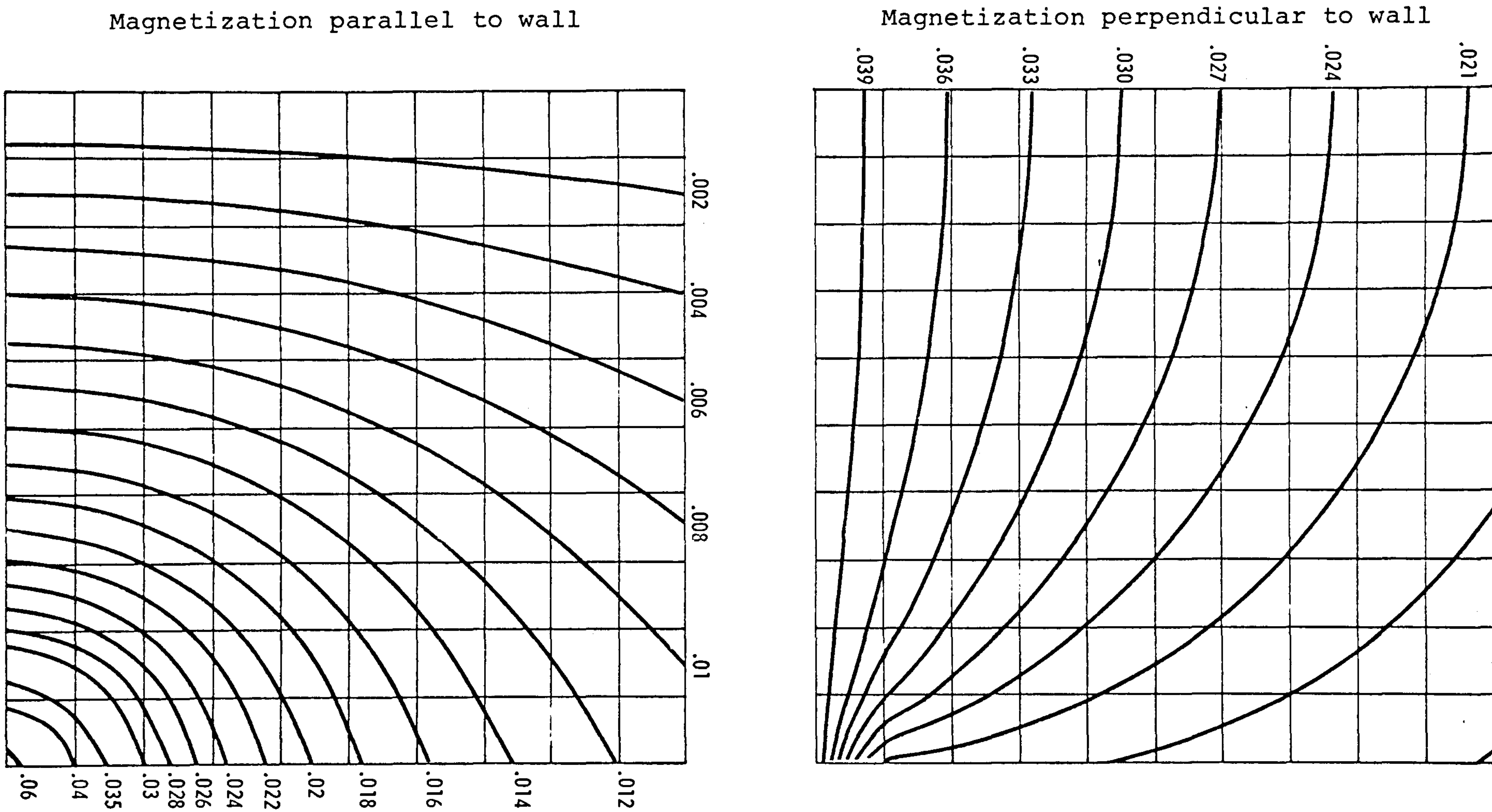

Fig. 4.4d. Iso-angle contours. R = 23.0, $\Phi_w = .042$.

charge density on the surfaces has logarithmic singularities at the corners and at the intersection of the charged wall. (The true charge density can of course never be larger than M_s. The infinity results from the small angle approximation.)

Figs. 4.4a, b, c, d show iso-angle contours for the x and y angles of the magnetization. The rotation of the x spins away from the wall and the y spins away from the x-z plane quickly deviates from the uniform rotation assumed in the simple model above. Peaking of the charge density at the corner (for iron) and the ends of the wall (high anisotropy) is evident. For $H_A = 0$ (not shown) the magnetization is nearly identical to that for $R = \frac{H_A}{4\pi M_s} = .023$ (iron at room temperature).

4.1.3 More Accurate Calculation of the Surface Charge

Within the approximation (if any) of no volume charge, we can carry out a more detailed investigation of the surface charge. The charge density on the wall, as a fraction of the wall angle, is again

$$\frac{\sigma_w}{M_s\theta} = 2(1-\Phi_w) = \frac{2R}{1+R} \; . \tag{4.6}$$

In dimensionless variables, the torque equations at the surfaces and perpendicular to them are

$$4\pi R\Phi_x(y) = 2(1-\Phi_w)\int_0^1 dy'[K_x(1,y-y') + K_x(1,y+y')]$$

$$+\int_0^1 dy'[K_x(2,y-y') + K_x(2,y+y')]\ \Phi_x(y')$$

$$+\int_0^1 dx'[K_x(1-x',y-1) + K_x(1+x',y-1)$$

$$+ K_x(1-x',y+1) + K_x(1+x',y+1)]\ \Phi_y(x')$$

$$- 2\pi\Phi_x(y) \qquad (4.7a)$$

and

$$4\pi R\Phi_y(x) = 2(1-\Phi_w)\int_0^1 dy'[K_y(x,1-y') + K_y(x,1+y')]$$

$$+\int_0^1 dy'[K_y(x-1,1-y') + K_y(x-1,1+y')$$

$$+ K_y(x+1,1-y') + K_y(x+1,1+y')]\Phi_x(y')$$

$$+\int_0^1 dx'[K_y(x-x',2) + K_y(x+x',2)]\Phi_y(x')$$

$$- 2\pi\Phi_y(x), \qquad (4.7b)$$

for the surfaces parallel and perpendicular to the wall, respectively.

These coupled equations must be solved, along with the

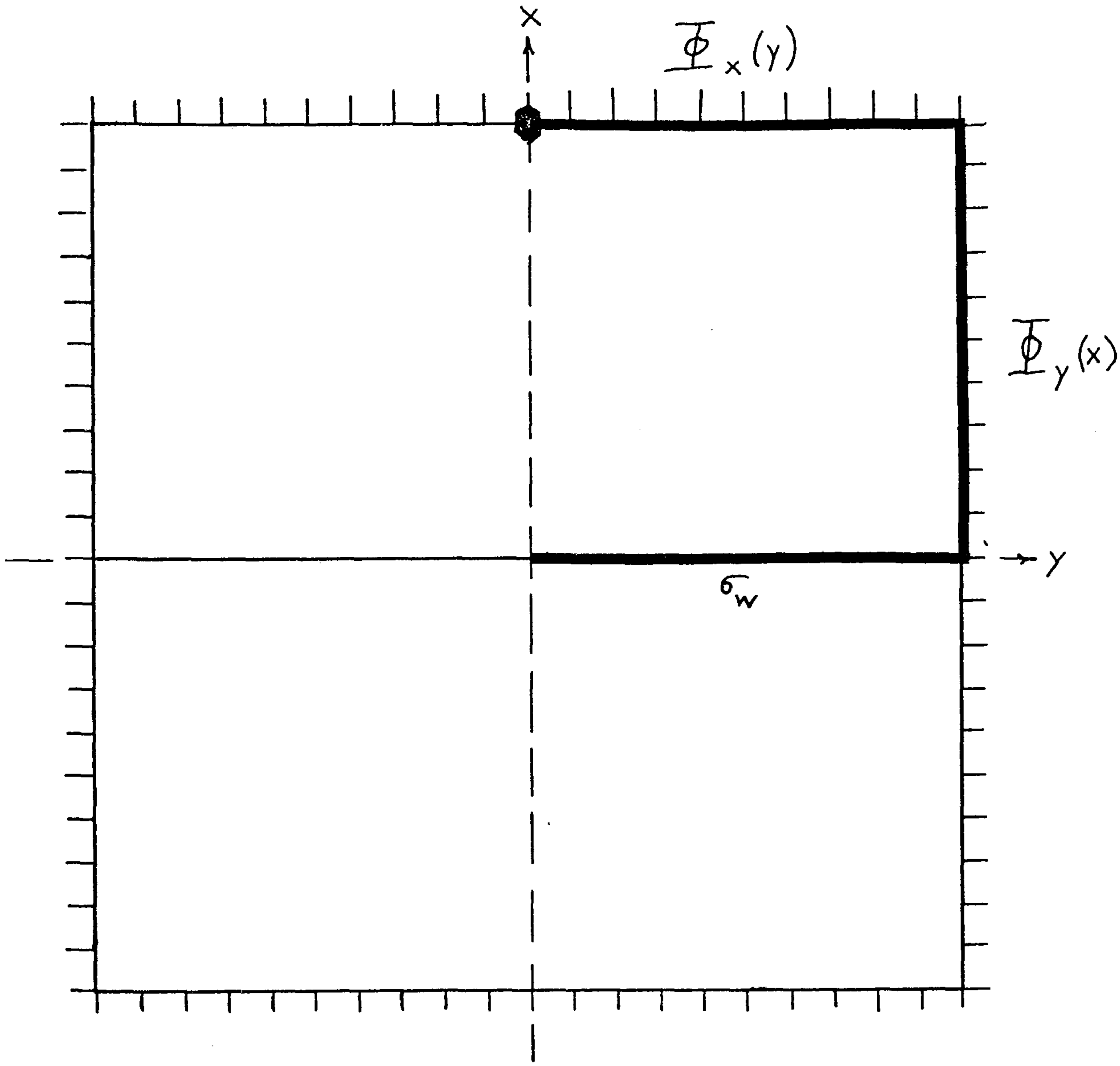

Fig. 4.5. Grids used to solve (4.7), shown here for m = 10. Fields are evaluated on the grid lines in the upper right quadrant, except at the point ⬥ where the self-consistency condition is replaced by (4.7c). σ_w is uniform and depends only on R.

constraint of unit charge/length on wall and surfaces:

$$\int_0^1 \Phi_x(y')dy' + \int_0^1 \Phi_y(x')dx' = \Phi_w \,. \qquad (4.7c)$$

In converting to linear equations, we divide each surface in a quadrant into m segments, with n = m + 1 angles needed as before to express the m charge densities (Fig. 4.5). The wall charge is also segmented, and we arrive at 2n + 1 equations and 2n unknown angles. One of the self-consistency conditions must be ignored (we choose the one for $\Phi_x(0)$, because to first order Φ_x doesn't vary there), and the remaining 2n equations are solved. (The program is in Appendix 4). The charge densities are plotted in Figs. 4.6a, b, c, d, e for m = 100. These charge densities are normalized in the sense of (4.7c). The curve for iron at room temperature (Fig. 4.6b) is almost identical to that for $H_A = 0$ (Fig. 4.6a). The logarithmic singularity at the intersection of wall and surface, is most evident at high anisotropy, when the wall charge is considerable.

Both the applied field $H_0\hat{z}$ and the longitudinal demagnetizing field $H'_z\hat{z}$ exert torque on the transverse magnetization, and should be included in $\vec{H}_T$. As we will see in Chapter 5, these two fields are nearly equal in magnitude and opposite in direction. Even if the cancellation were not good (which it is!), the applied field is always much less than H_A. In short whiskers $\frac{L}{d} \sim 25$ the departure field is ~ 50 gauss, and hence would give a small correction to R and a negligible correction

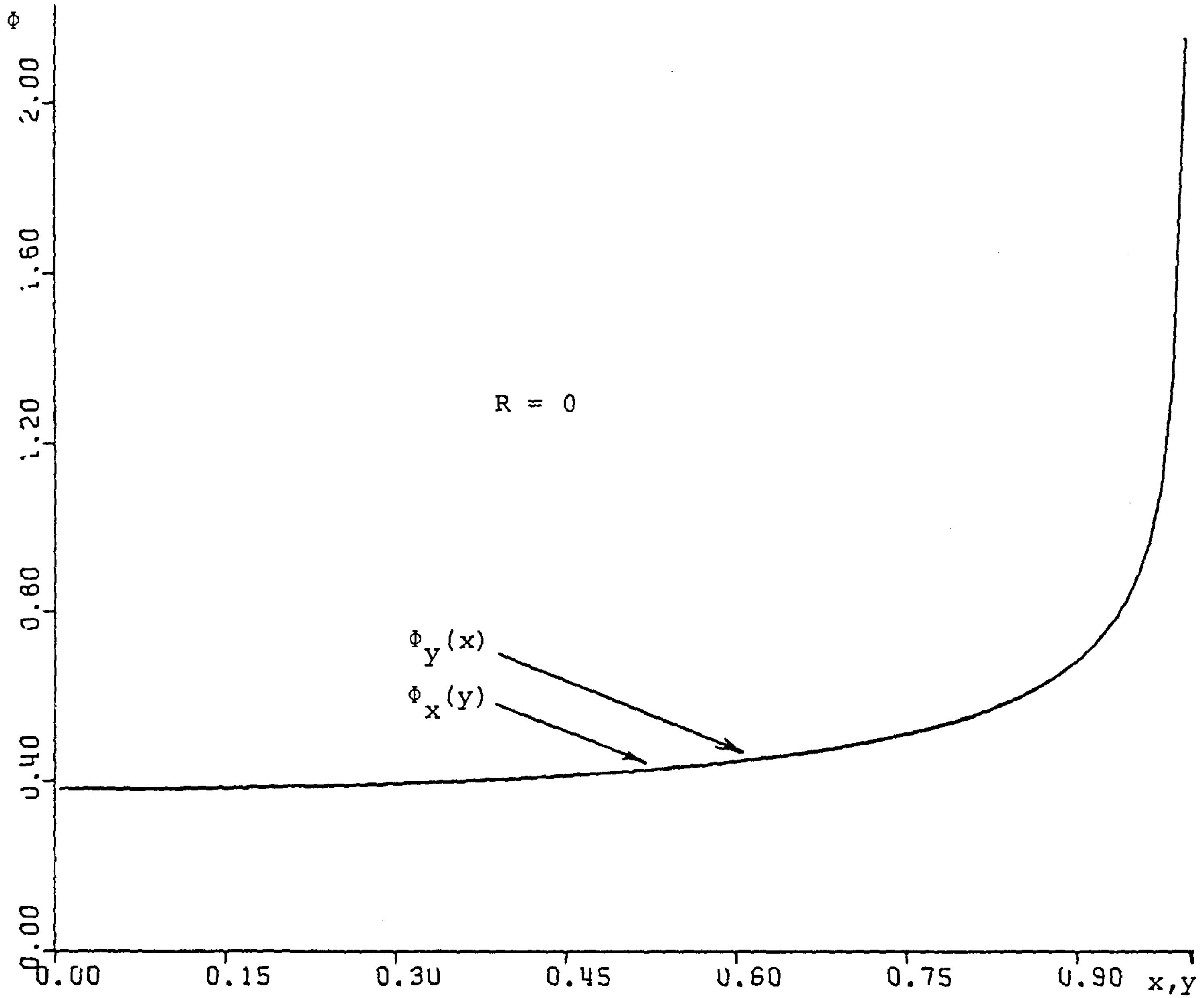

Fig. 4.6a. Magnetic surface charge density in the cross-section, assuming $\vec{\nabla}\cdot\vec{M} = 0$ in the domains. Charge density is normalized as in (4.7c). R = 0, and fraction of charge on wall = R/(1 + R) = 0. For this case, $\Phi_x = \Phi_y$.

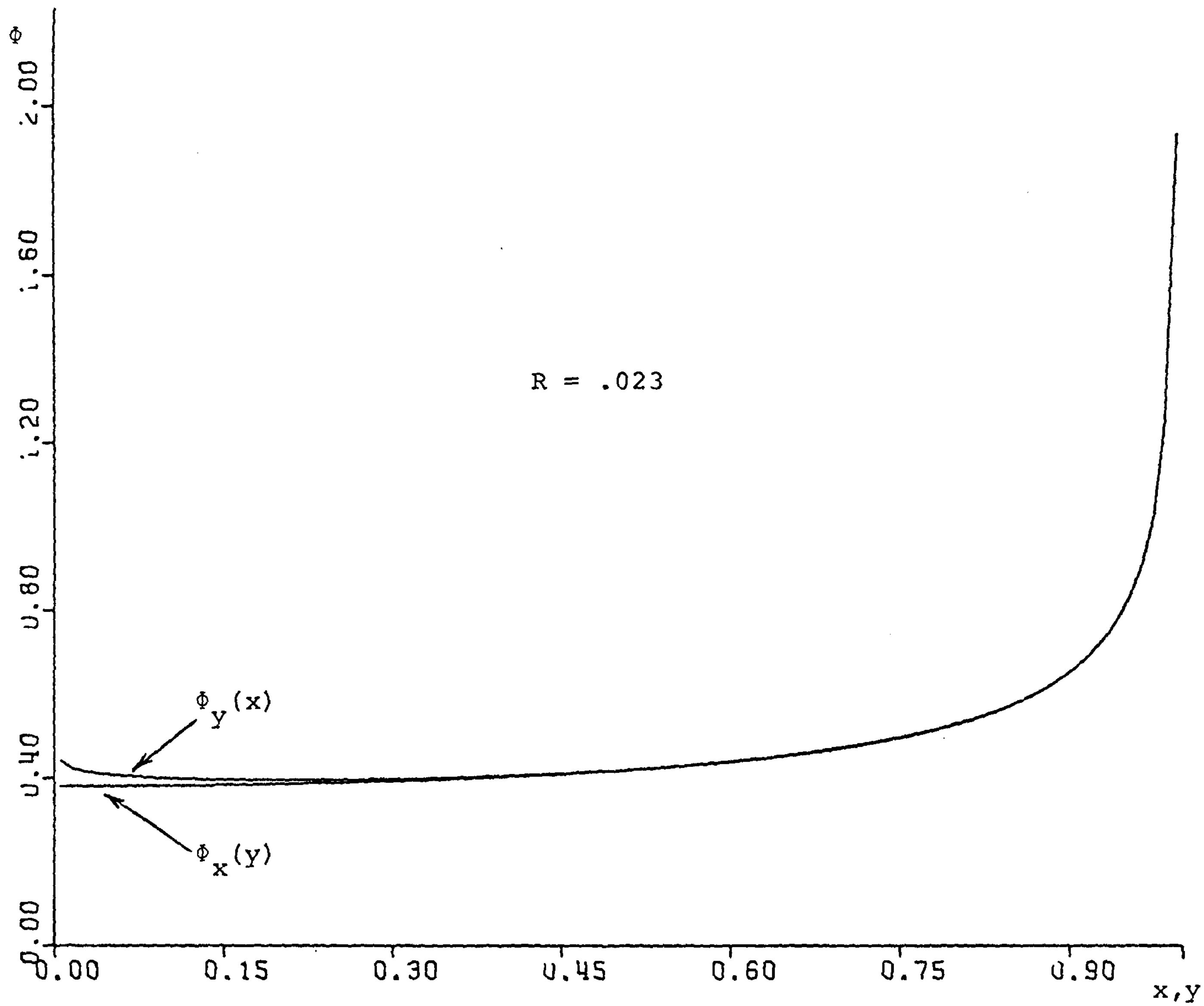

Fig. 4.6b. Magnetic surface charge density. R = .023, R/(1+R) = .023.

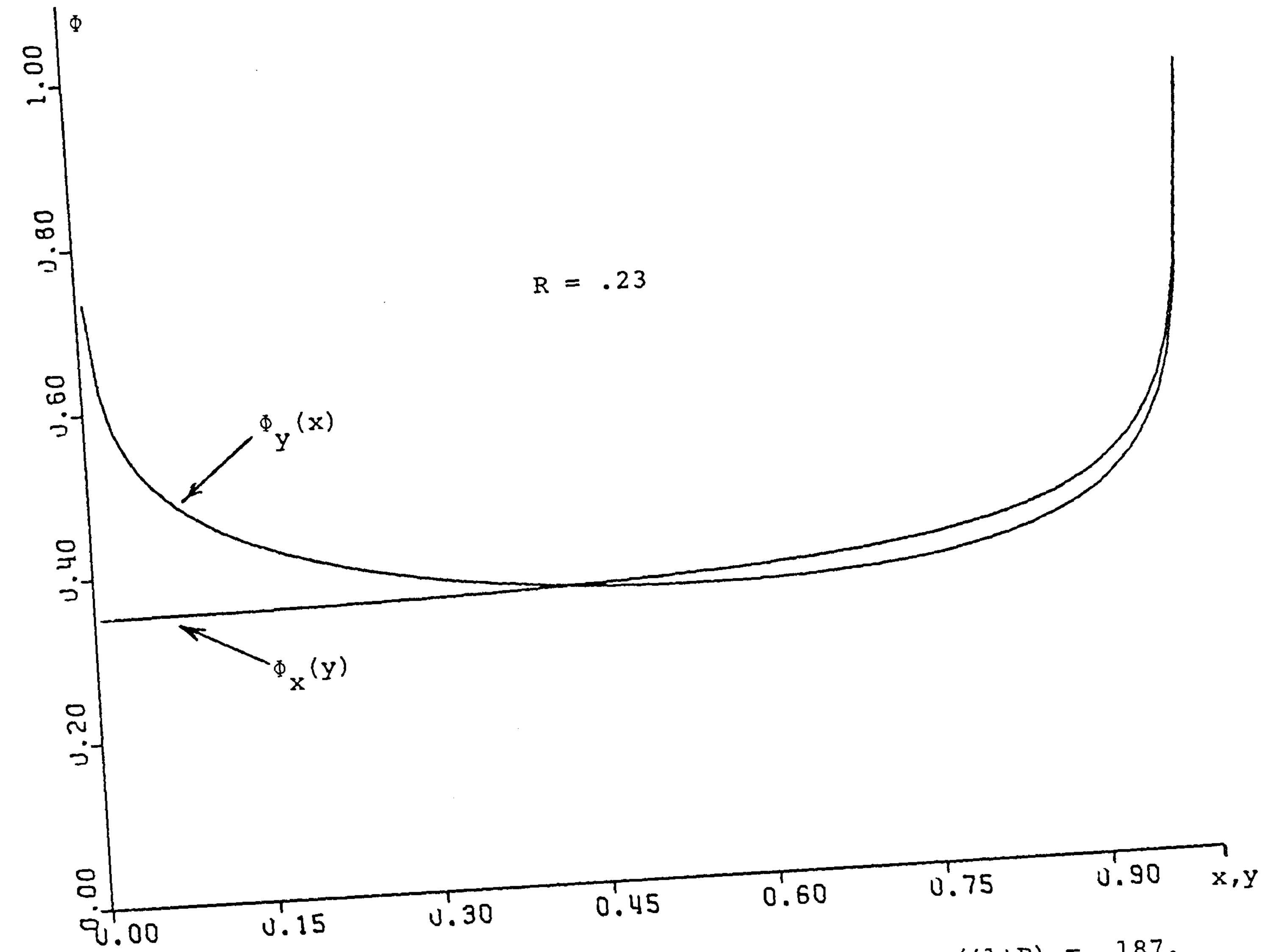

Fig. 4.6c. Magnetic surface charge density. R = .23, R/(1+R) = .187.

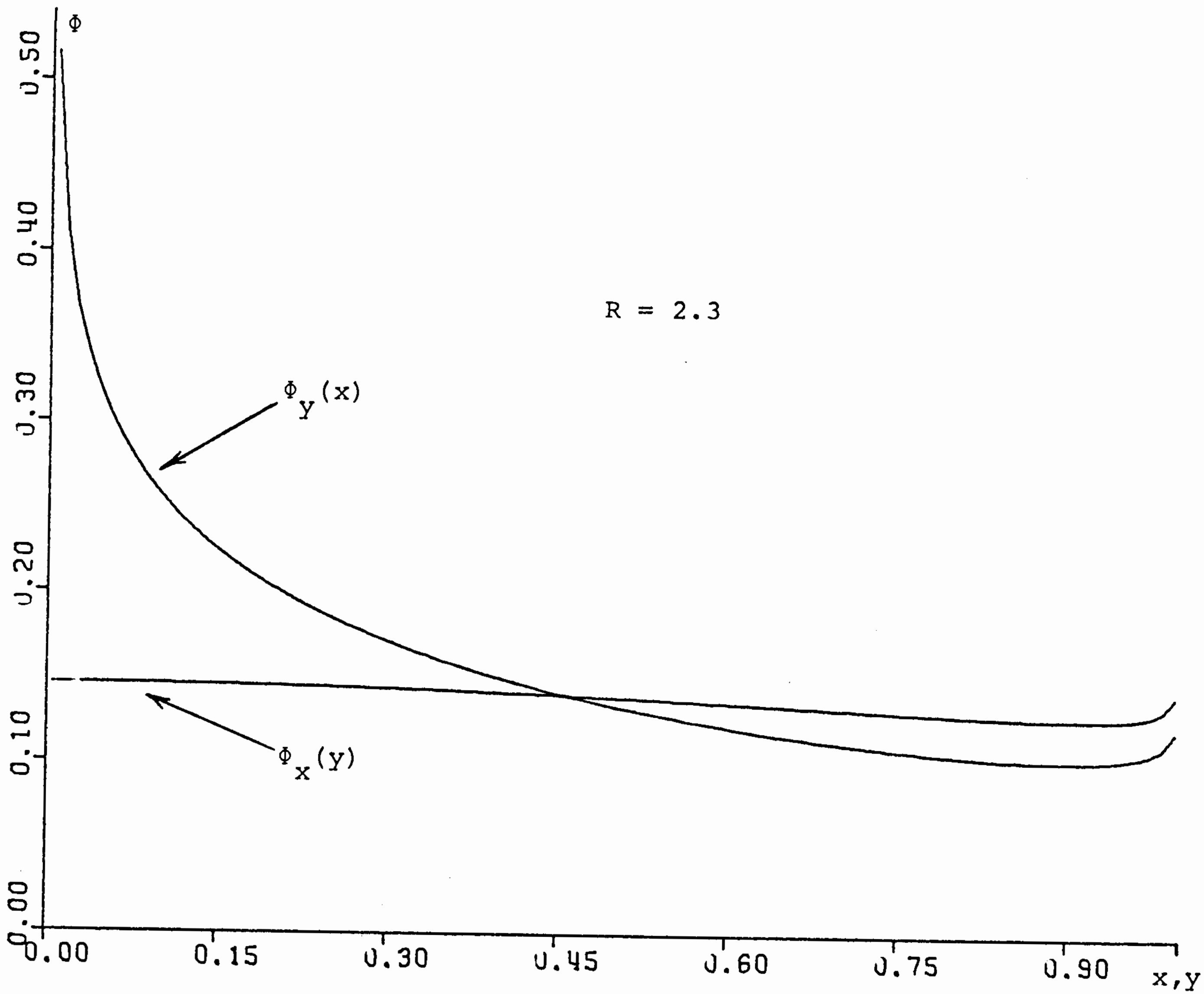

Fig. 4.6d. Magnetic surface charge density. R = 2.3, R/(1+R) = .697.

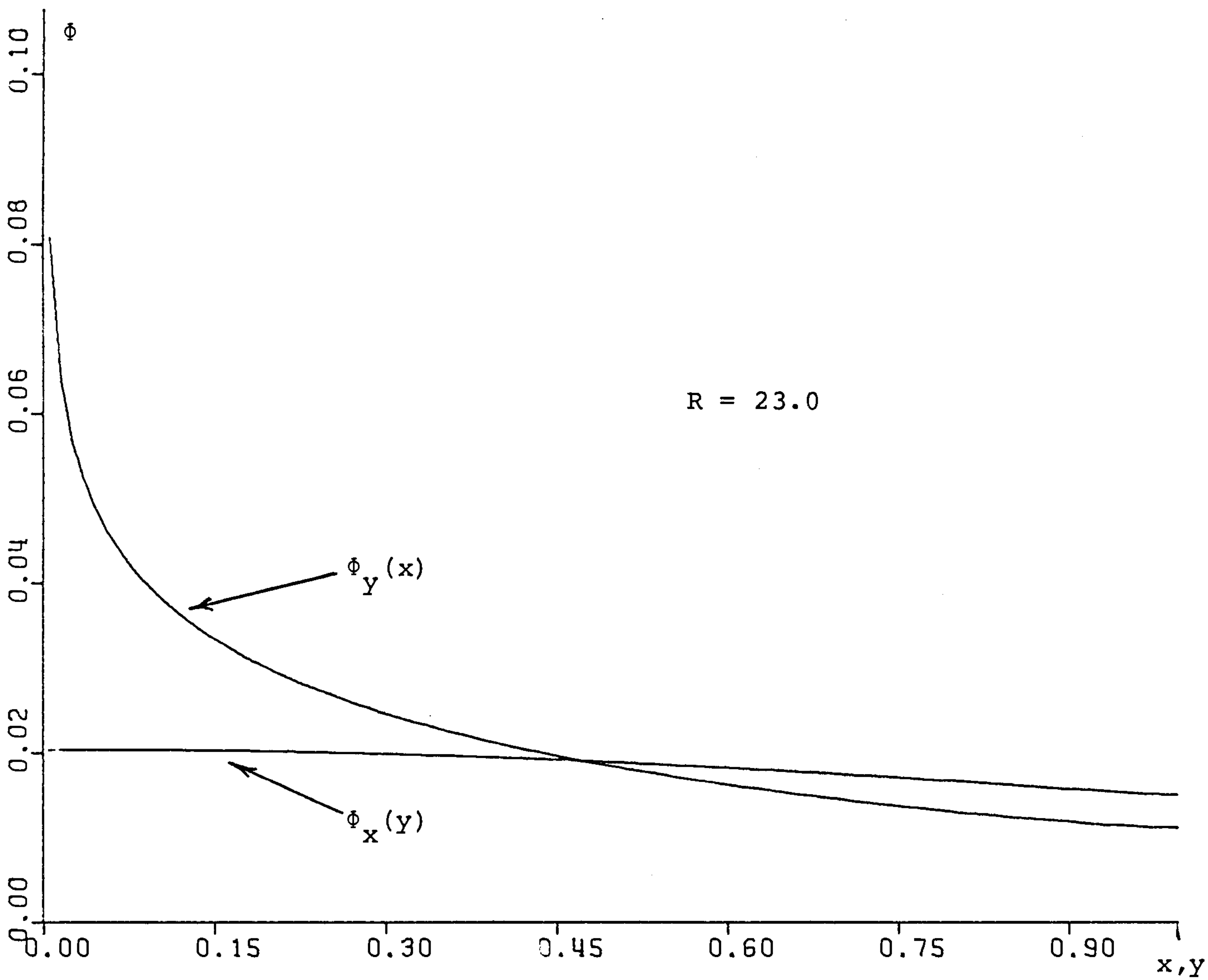

Fig. 4.6e. Magnetic surface charge density. $R = 23.0$, $R/(1+R) = .958$.

to the charge distribution (which as we have seen depends on $\frac{H_T}{4\pi M_s}$).

4.2 Minimization of the Energy

Consider an infinite ferromagnetic bar of square cross-section with a 180^0 wall in the center. If the sum of magnetostatic (demagnetizing) and anisotropy energies is minimized with the constraint of constant magnetic charge/unit length and a fraction $\frac{H_A}{4\pi M_s}$ of that charge on the wall, one arrives at the torque equations (4.4) solved previously. The energy/unit length of this model bar becomes infinite logarithmically as the length of the bar becomes infinite.

In this section we compare the energies (wall, exchange, magnetostrictive, anisotropy, and magnetostatic) of a finite whisker in a homogeneous field H_o with an assumed quadratic wall bowing. Only magnetostatics and anisotropy are important at room temperature, and an approximate expression is found for the increase in stiffness due to the anisotropy (over the stiffness due to magnetostatics alone).

4.2.1 Wall Energy

We are interested in the wall energy difference between the magnetized and unmagnetized whisker in the Landau configuration. We consider only the long wall and assume the wall energy/unit length is not changed by the applied field. This assumption is valid if the longitudinal internal field H_{i_z} is very small (so that the wall is symmetric about the plane through its center) and if the change in wall structure due to the charge on it is not significant.

The wall energy then changes during magnetization only due to an increase in length. Using (3.13) for the wall displacement in a small applied field, the change in wall area due to the bowing is

$$\Delta A = d \left[2 \int_0^{L/2} \sqrt{1 + \left(\frac{dx}{dz}\right)^2} dz \quad - L \right] ,$$

where

$$\Theta(z) \equiv \frac{dx}{dz} = - \frac{8 x_1 z}{L^2} .$$

Thus

$$\Delta A = \frac{8x_1^2 d}{3L} ,$$

and the change in wall energy is

$$\Delta E_w = \xi_w \Delta A, \tag{4.8}$$

where (Ki-56R, §10)

$$\xi_w \cong 2\pi(K_1 JS^2/a)^{1/2} \sim 1.1 \text{ erg/cm}^2$$

for iron. We rewrite (4.8) as

$$\Delta E_w = C_w \frac{x_1^2 d^2}{L} , \tag{4.9a}$$

where for d = .01 cm,

$$C_w = \frac{8\xi_w}{3d} \sim 300 \text{ erg/cm}^3 . \tag{4.9b}$$

This energy is 3 orders of magnitude less than the anisotopy energy in the domain(4.13) and of the same form; it can therefore be neglected. The wall itself acts like an elastic membrane with negligible restoring force.

4.2.2 Exchange Energy within the Domain

This energy is completely insignificant. For simplicity we consider only $\left(\frac{\partial M_x}{\partial x}\right)^2$ and take the exchange energy between two adjacent atoms to be

$$W_{ex}(z) = JS^2\psi_x^2(z) \cong JS^2\left[\frac{a}{d} \quad \Theta(z)\right]^2 ,$$

where ψ_x is the angle difference in the x-direction and a is the lattice spacing. The number of these atoms/unit length of the whisker is d^2/a^3, so the exchange energy is roughly

$$\Delta E_{ex} = \frac{2JS^2}{a}\int_0^{L/2} \Theta^2 dz = C_{ex}\frac{x_1^2 d^2}{L} , \qquad (4.10a)$$

where for d = .01 cm,

$$C_{ex} = \frac{16}{3}\frac{JS^2}{ad^2} \sim \frac{1}{10} \ \text{erg/cm}^3 . \qquad (4.10b)$$

4.2.3 Magnetostrictive Energy

Magnetostriction is only important in the closure domains, favoring

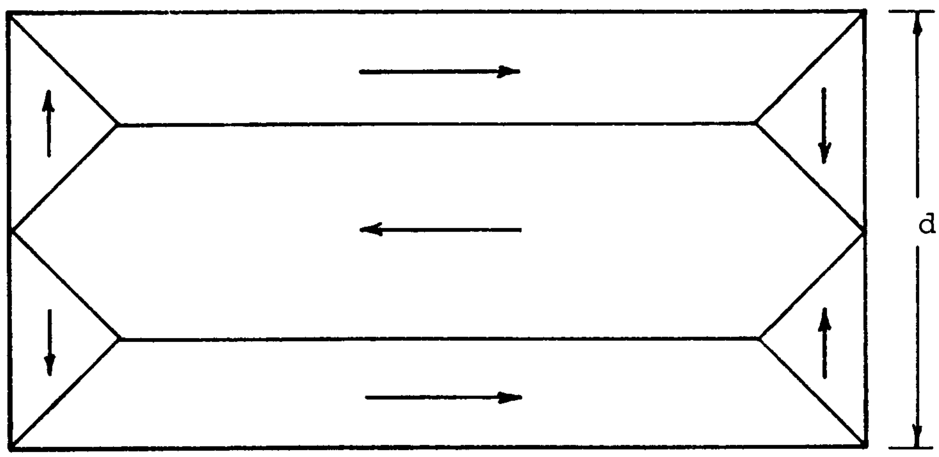

over the Landau structure. However, the Landau configuration has less wall energy, and a simple calculation (analogous to Chikazumi, Physics of Magnetism, p. 230) shows it is favored in iron when d $\lesssim$ 740 μ.

Differentiation between the two structures is not possible using only the in-phase susceptibility (see Chapter 5). Both configurations should have the same departure field (at $\langle\langle M \rangle\rangle \approx \frac{2}{3} M_s$), but the two-walled structure is expected to have reduced eddy current losses, and hence a smaller out-phase susceptibility (He-72). The double brackets $\langle\langle\ \rangle\rangle$ indicate a volume average over the entire whisker.

4.2.4 Anisotropy Energy

If all magnetization were along $\hat{z}$ or $-\hat{z}$, the charges would be entirely on the wall and the anisotropy energy would be zero. We compare this with the energy for a uniform rotation of magnetization discussed in Sec. 4.1, where for

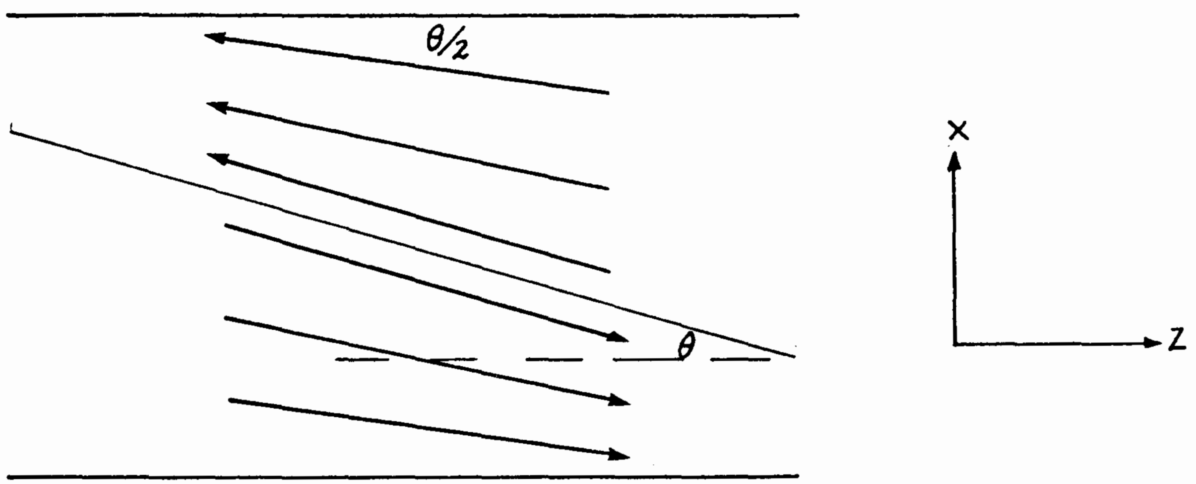

Angles are $\alpha(x,z)$

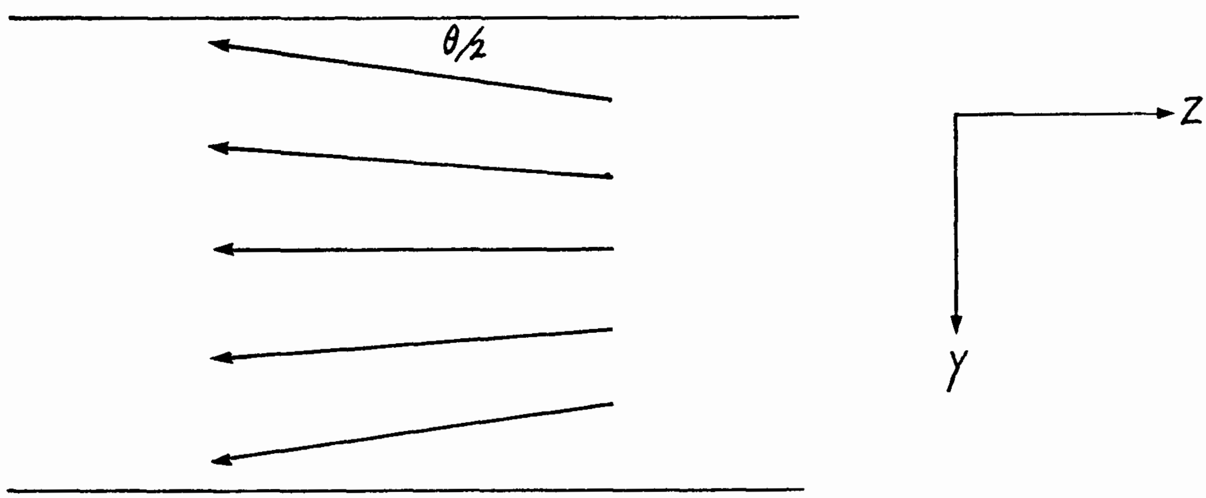

Angles are $\beta(y,z)$

Fig. 4.7. Approximate magnetization in a segment of the whisker. The wall is in the center and all charge is put uniformly on the four surfaces.

simplicity all charge is distributed uniformly on the four sides and the wall is in the center (Fig. 4.7). For small deviations from the z-direction the magnetization is

$$\hat{M} = \alpha(x,z)\ \hat{x} + \beta(y,z)\ \hat{y} + \left[1 - \frac{1}{2}\ (\alpha^2 + \beta^2)\right]\hat{z}, \quad (4.11)$$

where for a quadratic bowing of the long wall the approximate micromagnetic solution is $(x,y,z > 0)$

$$\alpha(x,z) = \Theta\left(1 - \frac{x}{d}\right) = \frac{8x_1}{L^2}\ z\ \left(1 - \frac{x}{d}\right) \quad (4.12)$$

$$\beta(y,z) = \Theta\ \frac{y}{d} = \frac{8x_1}{L^2 d}\ yz.$$

To second order in small angles from (1.8)

$$\Delta E_a = \iiint K_1\ (\alpha^2 + \beta^2)\ d\tau$$

$$= \frac{1}{3}\ M_s H_A d^2 \int_{-L/2}^{L/2} \Theta^2(z)\ dz$$

$$= C_K\ \frac{x_1^2\ d^2}{L}, \quad (4.13a)$$

where $C_K = \frac{32}{9} K_1$ and $K_1 = \frac{1}{2}\ M_s H_A.$ (4.13b)

For iron $K_1 = 4.2 \times 10^5\ \frac{erg}{cm^3}$, and

$$C_K = 1.5 \times 10^6\ \frac{erg}{cm^3}. \quad (4.13c)$$

4.2.5 Magnetostatic Energy

In Ch. 3 the demagnetizing energy was found for various distributions of the poles. The reduction in demagnetizing energy when the poles are moved from the wall to the four surfaces is

$$\Delta E_d = E_w - E_4 s = C_d \; x_1^2 \frac{d^2}{L} \;, \tag{4.14a}$$

where using (3.38),

$$C_d = \frac{64}{3} \; M_s^2 \left(\frac{\pi + \ln 2}{4} \right) = 5.9 \times 10^7 \; \frac{\text{erg}}{\text{cm}^3} \;. \tag{4.14b}$$

Because the angles are small, the magnetizing energy $-\int \vec{M} \cdot \vec{H}_o d\tau$ is not sensitive to the actual transverse magnetization. Here

$$\Delta E_m = H_o M_s \int \frac{1}{2} \; (\alpha^2 + \beta^2) \; d\tau = \frac{H_o}{H_A} \; \Delta E_a \;. \tag{4.15}$$

For typical whiskers $d << L$, $H_o << H_A$ in the linear susceptibility region, and this term can be ignored.

These energies show that magnetostatics strongly favors putting the charge on the surfaces and anisotropy weakly favors putting the charge on the wall. Energy minimization will clearly lie with most of the charge on the surface.

4.2.6 Decrease in Susceptibility due to Anisotropy

We ask for the relative change in stiffness when H_A is increased from 0 (near T_c) to ~ 500 gauss (the room temperature value). Let the energy be E_o when $H_A = 0$. This energy is purely magnetostatic and depends only on the applied field and the shape of the specimen. We are neglecting exchange energy. For $H_A = 0$, the 90° walls do not exist. Instead, the magnetization follows a curling pattern resembling the Landau structure (Chapter 6). We take from (3.38c)

$$E_o \approx E_{4s} = \frac{64}{3} M_s^2 \left[\ln \frac{2L}{d} - \frac{5}{6} - \left(\frac{\pi + \ln 2}{4} \right) \right] \frac{x_1^2 d^2}{L} \text{ ergs.} \quad (4.16)$$

Now increase H_A to 500 gauss, a value much less than $4\pi M_s$. This results in an increase in energy and hence a decrease in susceptibility. The increase in anisotropy energy is slightly compensated because about 2.3 percent of the charge goes to the wall, both decreasing the anisotropy energy and increasing the demagnetizing energy. But it will be seen that these latter effects are quite small. For small angles ($M_x, M_y \ll M_s$) the anisotropy energy varies as the square of the charge on the surface. Then the change in anisotropy energy is from (4.13)

$$\Delta E_a = p^2 E_a \quad , \qquad (4.17)$$

where $E_a = 1.5 \times 10^6 \dfrac{x_1^2 \; d^2}{L}$ and p is the fraction of charge left on the surface when charge q=1-p moves to the wall.

The increase in demagnetizing energy is

$$\Delta E_{mag} = E_o p^2 + E_w q^2 + E_{int}\, pq - E_o \; , \qquad (4.18)$$

where from (3.38a)

$$E_w = \frac{64}{3} M_s^2 \left[\ln \frac{2L}{d} - \frac{5}{6} \right] \frac{x_1^2 d^2}{L} \text{ ergs} \qquad (4.19)$$

is the demagnetizing energy when all poles are on the wall, and E_{int} is the energy of interaction between poles on the wall and surfaces.

E_{int} could be found by doing the integration, assuming uniform charge distribution on the surfaces. However the charge is not uniform and another approach is necessary.

The total change in energy is

$$\Delta E = \Delta E_a + \Delta E_{mag}. \tag{4.20}$$

We vary p to minimize ΔE and solve for E_{int}:

$$E_{int} = \frac{2p\ (E_o + E_w + E_a) - 2E_w}{2p - 1}. \tag{4.21}$$

Expanding E_{int} in a power series in q, retaining terms to order q and using $E_a << E_o$,

$$E_{int} \cong 2(E_o + E_a) - 2q\ (E_w - E_o). \tag{4.22}$$

Now E_{int} must be larger than $2E_o$. Otherwise, the minimum energy state in the <u>absence</u> of anisotropy would have some charge on the wall. Then (4.22) becomes

$$E_a > q(E_w - E_o). \tag{4.23}$$

This is satisfied for the quantities calculated here. From micromagnetics we know p = .977. The value of E_a (4.13) is probably accurate within 10 percent. Using these in (4.20) and (4.21), we construct Table 4.2. $E_{int} \cong 2.001\ E_o$, only very slightly greater than 2. The increase in stiffness (decrease in susceptibility) from the presence of H_A is

Table 4.2

Magnetostatic and Anisotropy Energies for a Whisker

$\frac{L}{d}$	$\frac{E_o}{\frac{x_1^2 d^2 10^6}{L}}$	$\frac{E_w}{E_o}$	$\frac{E_a}{E_o}$	$\frac{E_{int}}{E_o}$	$\frac{\Delta E_a}{E_o}$	$\frac{\Delta E_{mag}}{E_o}$
25	131	1.45	.0115	2.0017	.0110	2.8×10^{-4}
50	173	1.34	.0086	2.0013	.0082	2.1×10^{-4}
75	198	1.30	.0076	2.0011	.0072	1.8×10^{-4}
100	216	1.27	.0069	2.0010	.0066	1.7×10^{-4}

$$\frac{\Delta E}{E_o} \cong \frac{\Delta E_a}{E_o} ,$$

arising almost entirely from turning on the anisotropy energy. The relaxation effects which in magnitude equal ΔE_{mag} are but 2 percent of ΔE. ΔE falls in the range

$$.6\% < \frac{\Delta E}{E_o} < 1.1\% \qquad (4.24)$$

for the whiskers studied. This is the fractional decrease in susceptibility when the temperature is lowered from T_c to room temperature.

4.3 The Poles are on the Surface

4.3.1 Experimental Verification

There are three experimental results which are sensitive to the location of the poles:

i) χ' (Ho) is a constant for $H_o < H_d$,

ii) χ' is independent of M_s and H_A, and

iii) the magnitude of χ' agrees with theory when the poles are on the surface.

The differential susceptibility is independent of the wall position. If there are both appreciable wall and surface charges one would expect the magnetostatic energy of these charges to change as the wall approaches one surface. It is unlikely that a charge redistribution will keep χ' constant as the applied field is varied.

Both the magnetization and H_A are monotonically decreasing functions of temperature, but H_A vanishes much more rapidly (approximately as M^{10}) as T increases (Chikazumi, Physics of Magnetism, p. 151). When $H_A = 0$ the energy is entirely magnetostatic and the poles are on the surface. If the poles were on the wall at room temperature, we would expect χ' to increase about 35 percent as the temperature is raised to T_c. The susceptibility has been found (Ar-72a) to be independent of T over the range $650^oK < T < T_c$. From the calculation of Sec. 4.2 we expect χ' to change by less than half a percent in this temperature range, in agreement with experiment. (The slight temperature dependence observed there results mostly from a change in eddy-current damping due to the temperature dependence of the conductivity.)

Finally, as shown in Sec. 3.3, the measured susceptibility is found to agree very well with the susceptibility calculated for charge on the surface. From Table 3.2a, the experimental deviation is not more than 5 percent from the energy calculation (one-spring model) and 3 percent from the field calculation of Chapter 5. If all charge were on the wall, the measured susceptibility would be 26 percent less than calculated.

4.3.2 Analogy to Infinite Susceptibility Medium

We consider the whisker in the limit $H_A \to 0$, which can be obtained in practice at temperatures near but below T_c. The self-consistency conditions (1.20) in this limit give

$$H_x' = \alpha(H_o + H_z') \tag{4.25}$$

$$H_{y'} = \beta(H_o + H_z').$$

Because there is no volume charge density we also have

$$\vec{\nabla}\cdot\vec{H}' = 0 \quad \text{inside,} \tag{4.26}$$

and the solution

$$\left.\begin{aligned} H'_x &= 0 \\ H'_y &= 0 \\ H'_z &= -H_o \end{aligned}\right\} \quad \vec{H}_i = 0 \tag{4.27}$$

clearly satisfies (4.25) and (4.26).

We now argue that (4.27) is the unique solution in this limit. The anisotropy energy vanishes as $H_A \to 0$. To the extent to which the exchange energy of the curling pattern can be neglected (Sec. 4.2.2), the whisker energy is entirely magnetostatic and the analogy of a perfect conductor in an electric field is exact. There, minimization of the electrostatic energy requires $\vec{E}_i = 0$ inside the conductor, since electric charge can move in the presence of a field. The analogous condition for the whisker is (4.27), that the internal magnetic field is zero everywhere. All charge is on the surface and the magnetostatic energy is a minimum.

We can describe the whisker when $H_A = 0$ as a medium of infinite intrinsic magnetic susceptibility, since a finite magnetization results when $\vec{H}_i = 0$. The demagnetizing field $\vec{H}'$ exactly cancels $\vec{H}_o$ everywhere inside, and the measured susceptibility is determined entirely by the shape of the whisker. (The perfect conductor likewise has infinite electric susceptibility, with a finite polarization when $\vec{E}_i = 0$. The depolarization field from the surface charge exactly cancels the applied electric field inside the conductor).

For a room temperature whisker ($H_A/4\pi M_s = .023$) there are small components of the transverse and longitudinal demagnetizing fields, and about 2.3 percent of the charge is on the wall. But compared to the zero anisotropy case, this is only a small rearrangement of charge in the cross-section. The longitudinal charge distribution still essentially minimizes magnetostatic energy, and would not be appreciably different from the zero anisotropy case. Thus for a room temperature specimen,

$$H'_z \cong -H_o.$$

Then from (1.20), the transverse demagnetizing fields are

$$H'_x \cong \alpha\, H_A$$

$$H'_y \cong \beta\, H_A.$$

The transverse internal fields are always much smaller than H_A, and the longitudinal internal fields are always much smaller than H_o (for $H_o < H_d$).

We call the infinite susceptibility model the "bar" to distinguish it from the whisker. The magnetization is continuous in the bar and has a <u>variable</u> magnitude.

$$\vec{M} = \lim_{\substack{\chi \to \infty \\ \vec{H}_i \to 0}} \chi \vec{H}_i \, . \tag{4.28}$$

The whisker is constrained by exchange forces to have $|\vec{M}| =$ constant, and for $H_A = 0$ the magnetization would be in a curling pattern to avoid poles at the ends. The magnetization in the bar is variable and decreases near the ends to avoid large demagnetizing fields there. The bar resembles the whisker in having an identical pole distribution on the surface.

In the next chapter we solve Maxwell's equations for the magnetization inside a long cylindrical bar in a longitudinal magnetic field, when the medium is linear (χ not a function of H_i),

$$\vec{M} = \chi \vec{H}_i . \tag{4.29}$$

We will be most interested in the special cases of $\chi = \infty$ and $H_0(z) = $ constant, but the method is applicable to any susceptibility and to any applied field.

CHAPTER 5

MAGNETOSTATICS OF LINEAR MEDIA: THE LONGITUDINAL MAGNETIZATION

In this chapter we derive approximate solutions to Maxwell's equations in media characterized by the linear relation $\vec{M} = \chi\vec{H}_i$. For simplicity we replace the bar of square cross-section (Sec. 4.3) by a cylindrical rod of equal length (L) and equal cross-sectional area, and solve for the internal fields and magnetization when a longitudinal field $H_o(z)\hat{z}$ is applied.

The experimental connection of the bar with the whisker is that in applied fields $H_o < H_d$ the average longitudinal magnetization in a cross-section should be nearly the same for both an infinite susceptibility bar and an iron whisker. For in such applied field, the 180° wall bows away from the center of the whisker. Correspondingly, the bar assumes a magnetization whose magnitude varies along the long axis in the same way as the 180° wall bends.

There is a long history of experimental and theoretical work on the magnetization of iron rods. Magnetization measurements were made on iron rods as early as 1899 (La-1899). Approximate calculations for the magnetization of a finite rod having arbitrary χ in a uniform axial field were made in Germany between 1924 and 1939 (Wa-36, Wa-37, Wa-39). The longitudinal magnetization was expressed in a series of even powers of z and carried out only to order z^2, although corrections to the fields from the quartic term were included. In the most elaborate calculation (St-35) a weighting factor was used to make the solution less dependent on the magnetization near the end, which was most inaccurate. Warmuth (Wa-39) tabulated various calculations for the rod, along with some interpolation formulas he devised for short and long rods. The results were reviewed by Bozorth and Chapin (Bo-42).

More recently, Okoshi (Ok-65) has determined ballistic demagnetizing factors for $\chi = \infty$ rods by analog measurements in an electrolytic tank. There have been several calculations (Jo-65, Jo-66) of rods with $\chi = 0$ (uniform magnetization), but this special case is not useful for soft ferromagnets except near saturation. Copeland (Co-72) did a one-dimensional iterative calculation of the magnetization in thin rectangular slabs of permalloy, and the results are similar to ours. For two- and three-dimensional magnetostatic problems, the differential equations can be solved iteratively by finite differences (Ko-70, Si-70). These methods are sufficiently general to allow for arbitrary material characteristics (B-H curve) and sample shape.

5.1 Fields, Poles, and Demagnetizing Factors

The internal magnetic field is composed of both applied and demagnetizing fields:

$$\vec{H}_i = \vec{H}_o + \vec{H}'. \tag{5.1}$$

We define the local intrinsic and measured susceptibilities, respectively, by

$$\vec{M} = \chi\vec{H}_i = \chi'\vec{H}_o. \tag{5.2}$$

(Similar expressions in (2.3) were for differential susceptibility and can be defined for any magnetic material, although the interpretation of χ as a local intrinsic property of a real ferromagnet makes sense only for $\chi = \infty$. Otherwise χ is at best a microscopic average.) We consider linear media, where χ is independent of H_i. It was shown in Sec. 4.3.2 that when $\chi = \infty$, the fields in this fictitious magnetic medium are similar to those in a whisker.

Using (1.1a), (1.3), (5.2),

$$\vec{\nabla} \cdot \vec{B}_i = \vec{\nabla} \cdot (1+4\pi\chi)\vec{H}_i = (1+4\pi\chi)\vec{\nabla} \cdot \vec{H}_i = 0 \ ,$$

so for a ferromagnet

$$\vec{\nabla} \cdot \vec{H}_i = 0$$

and it follows that

$$\vec{\nabla} \cdot \vec{M} = 0 \qquad \text{inside,} \tag{5.3}$$

(This holds even for a perfect diamagnet (superconductor) since nothing discontinuous can happen as $\chi \to -\frac{1}{4\pi}$). For any susceptibility, all charge is on the surface. Because $\vec{H}$ is defined to be an axial field ($\vec{\nabla}\times \vec{H}_i = 0$),

$$\vec{\nabla} \times \vec{M} = 0 \tag{5.4}$$

and $\vec{M}$ can be written as the gradient of a potential U_m, which satisfies the Laplace equation

$$\nabla^2 U_m = 0 \qquad \text{inside} .$$

The demagnetizing field from a uniform magnetization is uniform only in ellipsoidal specimens. For any other shape the demagnetizing field is non-uniform. The equilibrium magnetization is then non-uniform (when $\chi \neq 0$) and scales linearly with H_i. (In real ferromagnets $|\vec{M}| = M_s$, and the magnetization does approach saturation (uniformity) as $H_o \to \infty$).

For an ellipsoidal specimen the demagnetizing factor $\overleftrightarrow{D}$ defined by

$$\vec{H}' \equiv -4\pi \overleftrightarrow{D} \vec{M} \tag{5.5}$$

is a tensor and depends only on the sample dimensions. For non-ellipsoidal specimens it depends on position and intrinsic susceptibility as well as shape. Two useful average demagnetizing factors are the ballistic (D_b) and magnetometric (D_m), defined as

$$\langle H'_z(z)\rangle = -4\pi D_b(z)\ \langle M_z(z)\rangle \tag{5.6a}$$

and

$$\langle\langle H'_z\rangle\rangle = -4\pi D_m\ \langle\langle M_z\rangle\rangle\quad , \tag{5.6b}$$

where the average in (5.6a) is as usual over the cross-section at z and in (5.6b) the entire sample is averaged. We are considering long rods in a longitudinal field, so only the D_{zz} component is important. D_b is useful when the pick-up coil is much shorter than the sample. We will only be interested in $D_b(0) \equiv D_b$, the value at the center. From (5.1), (5.2), (5.6a, b),

$$\frac{1}{\chi'_b} - \frac{1}{\chi} = 4\pi D_b \tag{5.7a}$$

$$\frac{1}{\chi'_m} - \frac{1}{\chi} = 4\pi D_m \tag{5.7b}$$

where

$$\frac{1}{\chi'_b} = \frac{H_o}{\langle M(0)\rangle} \qquad \text{and} \qquad \frac{1}{\chi'_m} = \frac{H_o}{\langle\langle M\rangle\rangle} \quad .$$

For infinite instrinsic susceptibility the measured susceptibilities are given by these demagnetizing factors alone. When $D >> \frac{1}{4\pi\chi}$, the demagnetizing factor dominates the response of the sample, which then can be treated with little error as a medium of infinite susceptibility.

5.2 Solution for the Long Cylinder

In cylindrical coordinates (5.3) becomes

$$\frac{\partial M_z}{\partial z} = -\frac{1}{r}\frac{\partial}{\partial r}(rMr) \cdot \tag{5.8}$$

The magnetization satisfies

$$\vec{M} = \chi(\vec{H}_o + \vec{H}') \tag{5.9}$$

everywhere inside the rod. $\vec{H}'$ is related to $\vec{M}$ by

$$\vec{H}'(\vec{r}) = \iint_{\text{surface}} \frac{\sigma(\vec{r}')}{|\vec{r}-\vec{r}'|^2}(\hat{r}-\hat{r}')dS,$$

where $\sigma = \vec{M} \cdot \hat{n}$ and $\hat{n}$ is the outward unit normal to the surface.

For long cylinders ($\rho \equiv \frac{d}{L} << 1$) we can neglect the r-dependence of $\frac{\partial M_z}{\partial z}$, and (5.8) can be integrated to

$$\frac{\partial M_z}{\partial z} = -\frac{2}{r} M_r \cdot \tag{5.10}$$

Integrating again along the z-axis and using

$$M_r(r = \frac{d}{2}, z) = \sigma(z)$$

$$M_z(r, z = \frac{L}{2}) = \sigma_{end}(r),$$

we find

$$M_z(z) = \sigma_{end}(0) + \frac{4}{d}\int_z^{L/2} \sigma(z')dz' \quad . \tag{5.11}$$

In the presence of an applied field $H_o\hat{z}$, the demagnetizing field along the z-axis is

$$\vec{H}'(z) = \hat{z}\pi d \int_0^{L/2} \sigma(z')dz' \left\{ \frac{z-z'}{[(z-z')^2+\left(\frac{d}{2}\right)^2]^{3/2}} - \frac{z+z'}{[(z+z')^2+\left(\frac{d}{2}\right)^2]^{3/2}} \right\}$$

$$+ \vec{H}'_{end}(z) \ , \tag{5.12}$$

where we used $\sigma(z) = -\sigma(-z) \geqslant 0$. Taking σ_{end} to be uniform and putting (5.11) and (5.12) into the self-consistency condition (5.9), we get

$$-H_o = 2\pi\rho \int_0^1 \sigma(z')K(z,z')dz' - 2\pi\sigma_{end}J(z)$$

$$- \frac{1}{\chi}\left[\sigma_{end} + \frac{2}{\rho}\int_z^1 \sigma(z')dz'\right] , \tag{5.13}$$

where

$$K(z,z') = \frac{z-z'}{[(z-z')^2+\rho^2]^{3/2}} - \frac{z+z'}{[(z+z')^2+\rho^2]^{3/2}}$$

and

$$J(z) = 2 - \frac{1-z}{[(1-z)^2+\rho^2]^{\frac{1}{2}}} - \frac{1+z}{[(1+z)^2+\rho^2]^{\frac{1}{2}}} \quad .$$

Note that the variables are now dimensionless.

This integral equation (5.13) has ρ and χ as parameters. The applied field on the LHS is uniform (this case is treated in Sec. 5.2.1), but in general it can be any function of z (a non-uniform field is treated in Sec. 5.2.2). The equation is valid at all points on the z-axis for z < 1. It constitutes an infinite number of simultaneous linear equations in the unknowns $\sigma(z)$ and σ_{end}, and can be solved to arbitrary accuracy by dividing the cylinder into 2m discs with uniform charge on the surface of each disc. We let the source points be in a ring centered on the surface of each disc and evaluate (5.13) on the axis at

$$z = \frac{k-1}{m} \quad , \qquad k = 1, \ldots m + 1 \quad .$$

These m + 1 equations are solved for the m charge densities on the side and the charge on the end of the cylinder.

5.2.1 Homogeneous Driving Results

In Fig. 5.1 we plot $\langle M(z)\rangle/\langle M(0)\rangle$ for various χ for a long rod ($\rho = \frac{2r}{L} = .01$) homogeneously driven. The magnetization is normalized to the value at the center. The $\chi = \infty$ curve fits the measured susceptibility (Figs. 2.3). The magnetization is nearly quadratic for $\chi \gg \frac{1}{4\pi D_b}$ and in the limit $\chi \to 0$ it approaches uniformity where all the poles are on the ends.

$\langle M(0)\rangle$ is a maximum ($\langle M(0)\rangle = \frac{H_o}{4\pi D_b}$) for $\chi = \infty$ and decreases to χH_o as $\chi \to 0$. Fig. 5.2 shows $\chi'(z) = \frac{\langle M(z)\rangle}{H_o}$, the susceptibility of the rod (as measured with a short pick-up coil), plotted for various χ. For $\chi \gg \frac{1}{4\pi D_b}$ the shape of the rod determines χ', and the energy is mostly magnetostatic. For $\chi' \ll \frac{1}{4\pi D_b}$ the susceptibility is proportional to H_o, and the energy is mostly in the intrinsic magnetization process (Brown,

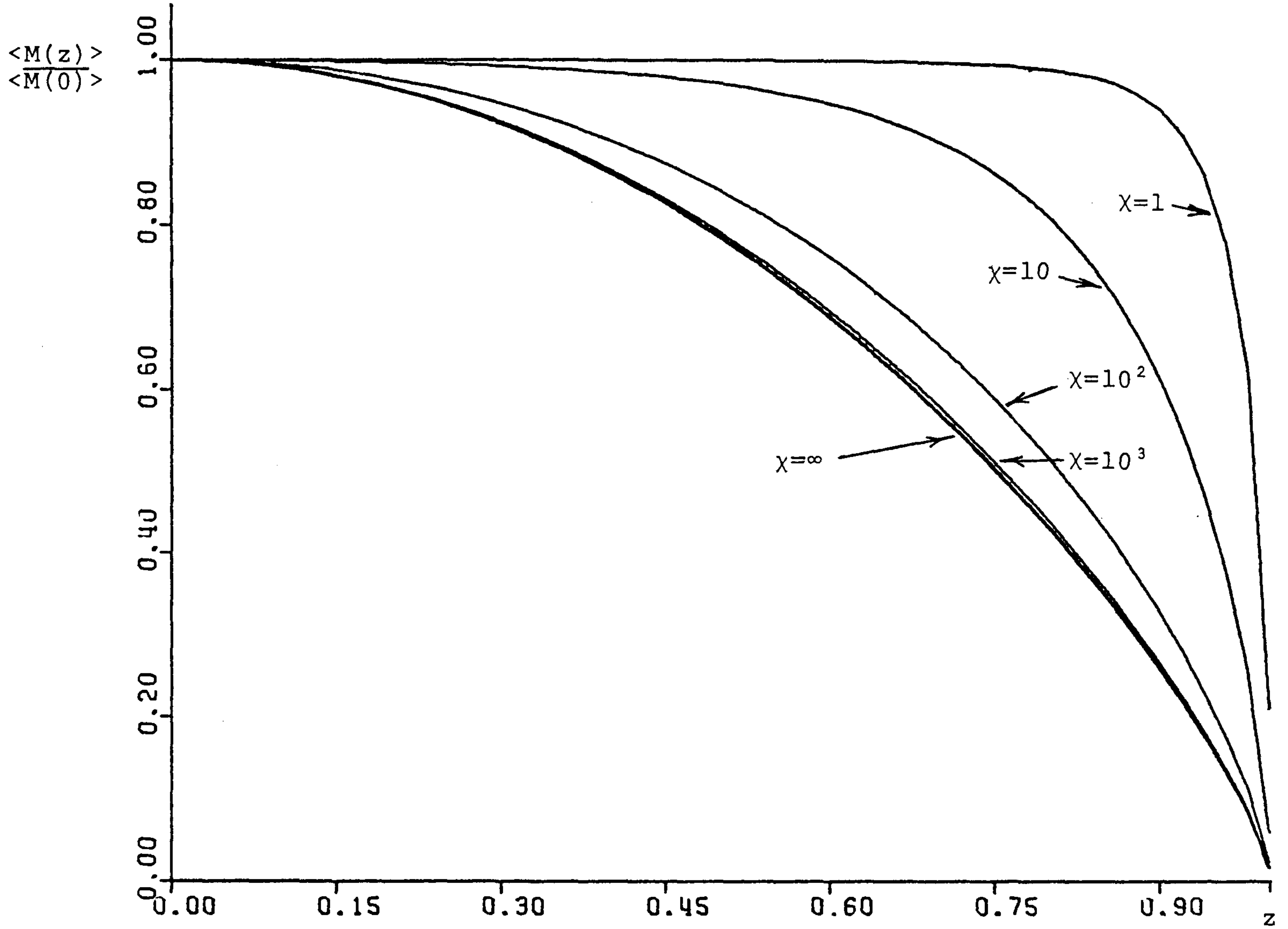

Fig. 5.1. Calculated normalized magnetization along a cylinder in homogeneous d.c. field. $\rho = 2r/L = .01$. χ is a parameter. The transition between uniform and quadratic response occurs around $\chi = 1/4\pi D \sim 100$.

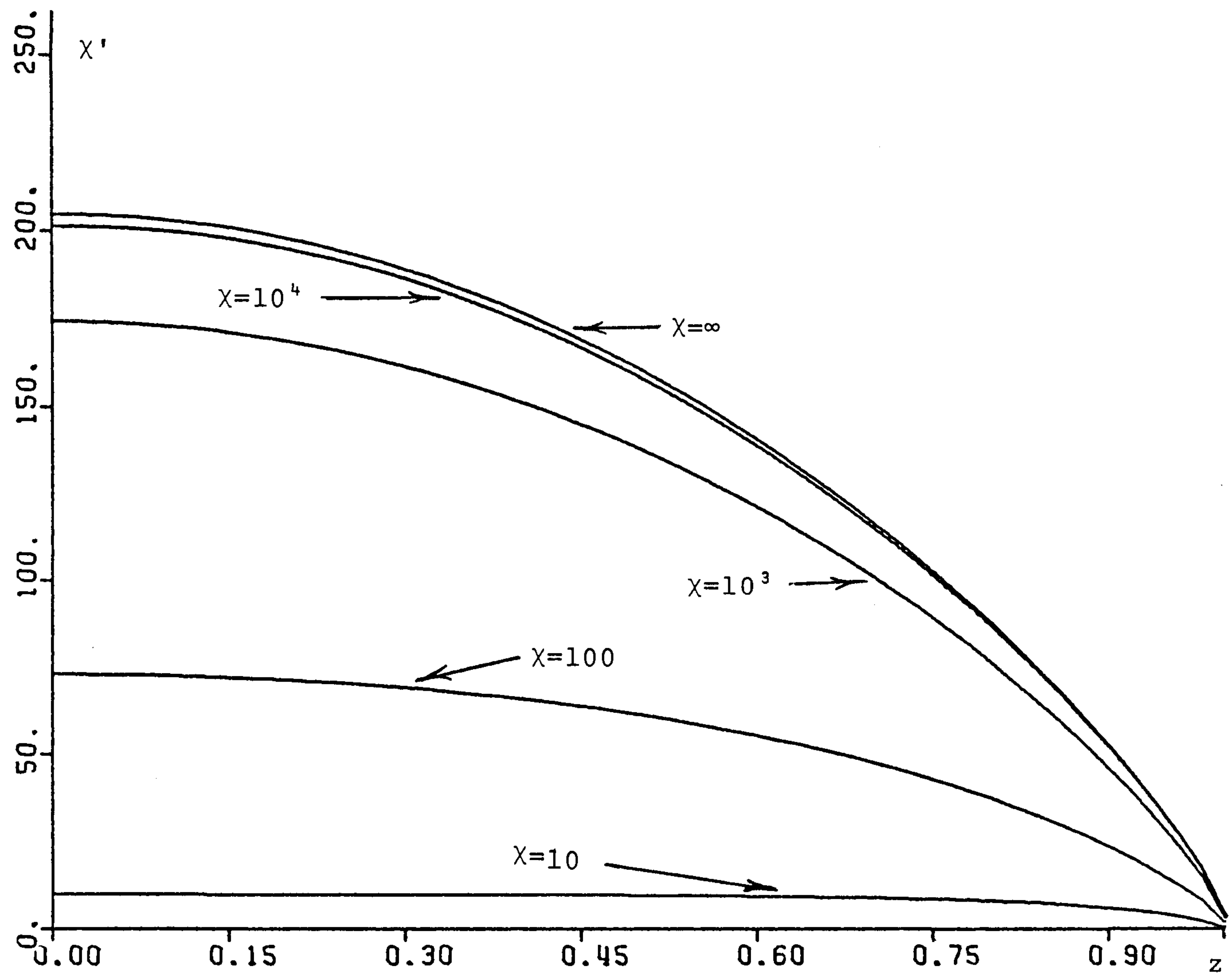

Fig. 5.2. Susceptibility $\chi'(z) = \langle M(z)\rangle/H_o$ calculated along a cylinder in homogeneous d.c. field. $\rho = .01$, χ is a parameter. χ' is a maximum when $\chi \to \infty$.

Magnetostatic Principles of Ferromagnetism, p. 56):

$$E \approx \iiint \frac{M^2}{2\chi}\, d\tau \ . \tag{5.14}$$

In Fig. 5.3 the susceptibility is plotted as a function of z for infinite susceptibility and various values of ρ. By inspection $\frac{\langle M(0)\rangle}{H_o} = \frac{1}{4\pi D_b}$ varies roughly as ρ^{-2}. This is to be expected from the results of Chapter 3 and the demagnetizing factor of an "equivalent" ellipsoid.

We develop formulas for the ballistic demagnetizing factor of a rectangular bar of infinite susceptibility. From (3.24) or (3.46) and (5.7a) the susceptibility for the 1-spring model is (all demagnetizing factors are ballistic)

$$\chi' = \frac{\langle M(0)\rangle}{H_o} = \frac{8}{3\gamma}\left(\frac{L}{d}\right)^2 = \frac{1}{4\pi D} \ . \tag{5.15}$$

We let $w = d/L$ for the bar and use γ_{4s} in (5.15):

$$D^{4s} = \frac{4}{\pi}\left(\frac{d}{L}\right)^2\left[\ln\frac{2L}{d} - \frac{5}{6} - \left(\frac{\pi + \ln 2}{4}\right)\right]$$

$$= \frac{4}{\pi}\, w^2\left[\ln\frac{1}{w} - 1.099\right] \ . \tag{5.16}$$

Using γ_c from the equivalent cylinder $\left(4w^2 = \pi\rho^2\right)$,

$$D^c = \frac{4}{\pi}\left(\frac{d}{L}\right)^2\left[\ln\frac{2\sqrt{\pi}L}{d} - \frac{7}{3}\right]$$

$$= \frac{4}{\pi}\, w^2\left[\ln\frac{1}{w} - 1.068\right] . \tag{5.17}$$

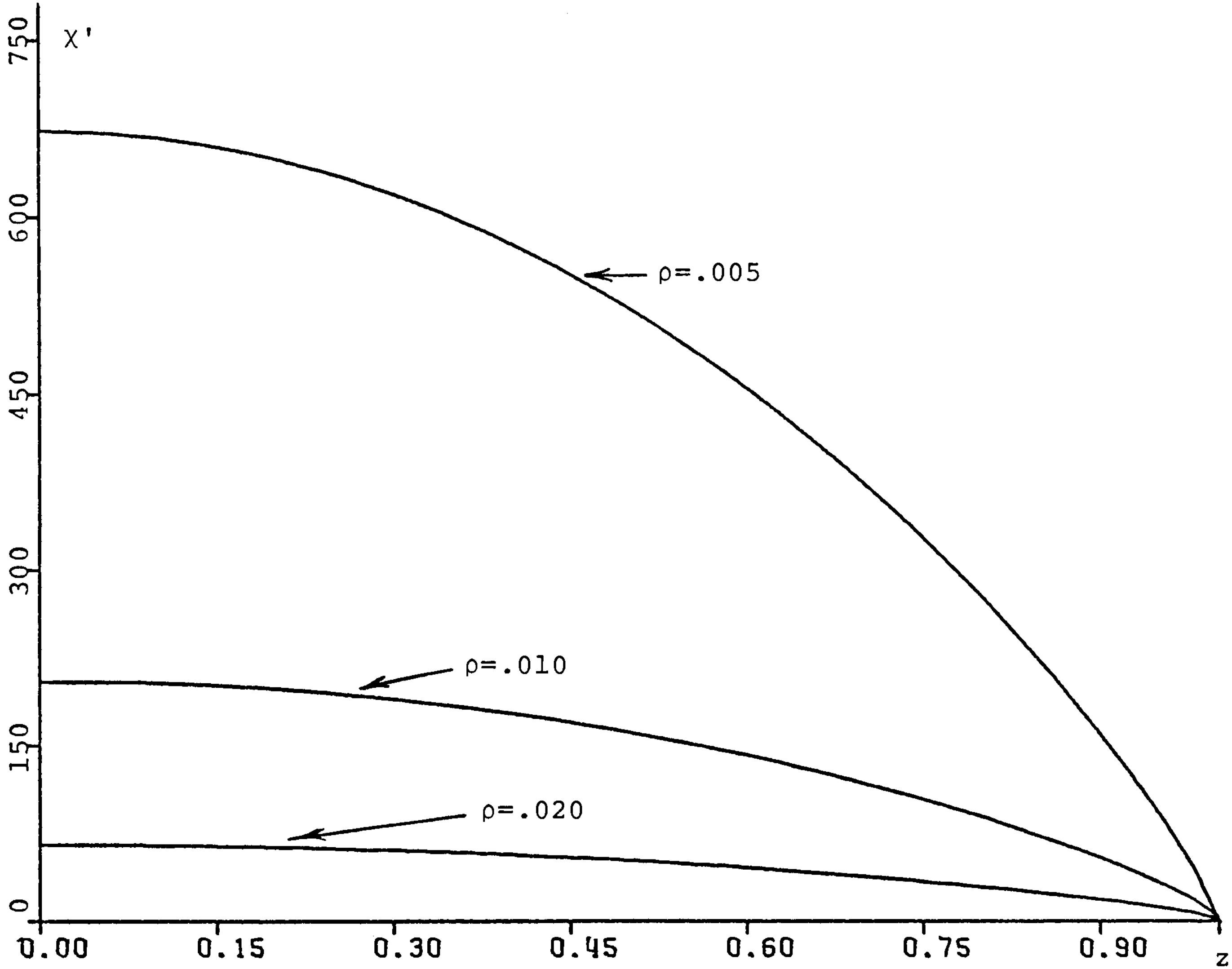

Fig. 5.3. Susceptibility $\chi'(z) = \langle M(z) \rangle / H_o$ calculated along a cylinder in homogeneous d.c. field. $\chi = \infty$, $\rho = 2r/L$ is a parameter.

These values agree within 1 percent. As we interpret from Tables 3.1 and 3.2, D^{4s} and D^{c} agree with the numerical calculation of this chapter to 3 percent.

The demagnetizing factor of an ellipsoid of rotation with axis ratio $\frac{b}{a}$ is (Os-45)

$$D^{ell} = \left(\frac{b}{a}\right)^2 \left[\ln \frac{2a}{b} - 1\right] \quad .$$

Defining "equivalent" in the same way as for the cylinder ($d^2 = \pi b^2$, $2a = L$, and $w^2 = \frac{d^2}{L^2} = \frac{\pi b^2}{4a^2}$),

$$D^{ell} = \frac{4}{\pi} \left(\frac{d}{L}\right)^2 \left[\ln \frac{\sqrt{\pi} L}{d} - 1\right]$$

$$= \frac{4}{\pi} w^2 \left[\ln \frac{1}{w} - .428\right] \quad . \tag{5.18}$$

D^{ell} differs from D^{c} by 15-25 percent.

We can compare our demagnetizing factors for cylindrical rods with those of Warmuth (Wa-37), who approximated the complicated expression of Stablein and Schlechtweg (St-35) by

$$D \cong .667\, \rho^{1.95} \left[\ln \frac{2}{\rho} - 1\right] \quad . \tag{5.19}$$

This agrees with Stablein's calculation at $\frac{1}{\rho} = 10$ and $\frac{1}{\rho} = 500$, but is nearly 4 percent too low for $\frac{1}{\rho} = 50$. Writing (5.17) in terms of ρ ,

$$D^{c}(\rho) = \rho^2 \left[\ln \frac{4}{\rho} - \frac{7}{3}\right] \quad . \tag{5.20}$$

T a b l e 5.1.

Comparison of Calculated Demagnetizing Factors of Infinite Susceptibility Rods.

$\frac{1}{\rho} = \frac{L}{2r}$	D (m=25)	D (m=50)	D (m=100)	D^{C}	D* Warmuth
10	.0153	.0151	.0150	.0136	.0151 (.0151)
20	.00540	.00535	.00532	.00512	.00518
30	.00286	.00281	.00280	.00273	.00272
40	.00182	.00176	.00175	.00171	.00170
50	.00128	.00122	.00121	.00119	.00118 (.00122)
60	.000956	.000902	.000892	.000874	.000866
70	.000743	.000700	.000687	.000674	.000667
80	.000594	.000561	.000548	.000537	.000533
90	.000486	.000462	.000448	.000439	.000435
100	.000404	.000389	.000374	.000366	.000368 (.000372)

* Values in parenthesis are those calculated by Stäblein and Schlechtweg.

In Table 5.1 we give the demagnetizing factors calculated numerically and by (5.19) and (5.20). Figures in parenthesis are from the calculation of Stablein and Schlechtweg, and the numerical calculation values remarkably converge toward them as the grid is made finer. Above $\frac{1}{\rho} = 20$ agreement between (5.19) and (5.20) is within 1 percent. This is interesting because of the relatively large disagreement of (5.19) with Stablein's calculation. We suspect the "true" value to lie above (5.19) and probably between (5.20) and the numerical calculation value for m = 100.

In Fig. 5.4 the susceptibilities from the numerical calculation (for m = 25, 50, 100) are compared with the experimentally measured values. This is related to Fig. 2.4 where the susceptibility is multiplied by d/L. The equivalent cylinder is defined in the usual way. The susceptibility is seen to converge fairly rapidly as m increases, convergence being slowest for long cylinders. The true susceptibility is probably larger than that calculated for m = 100.

Combining the $M_z(z)$ calculated from the charge density with $M_r(z)$ calculated from $M_z(z)$ using (5.10) permits us to give the schematic representation of the magnetization of the cylindrical rod shown in Fig. 5.5a. Comparison with Fig. 7.1 shows a resemblance to the magnetization in the y-z plane of the actual whisker when viewed from the bottom (but not the top!). The self-consistency condition can be visualized schematically in Fig. 5.5b. The correct $\vec{M}$ arising from a field $\vec{H}_o$ is such that the field $\vec{H}'$ (coming from the poles due to $\vec{M}$), when added

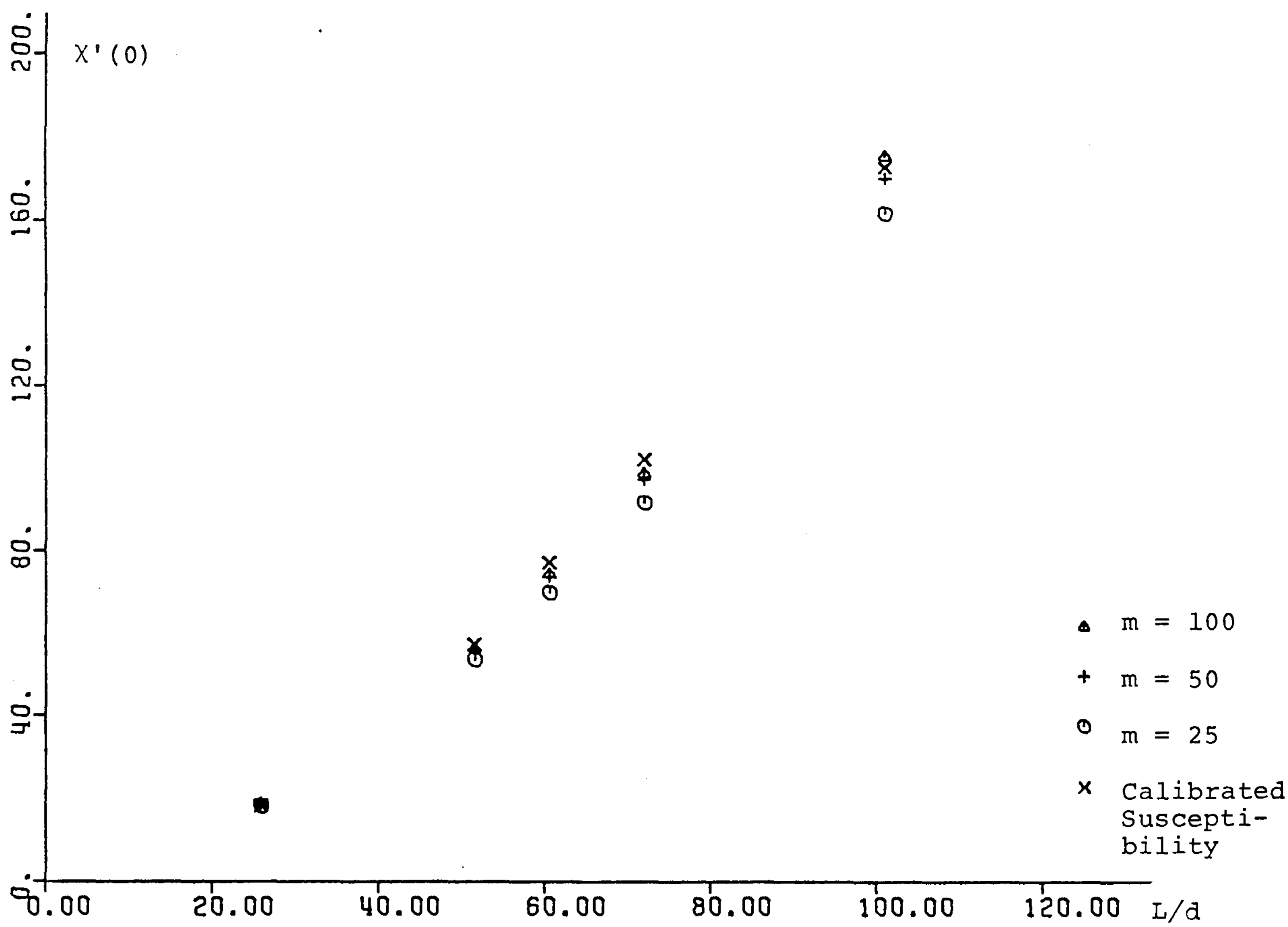

Fig. 5.4. Susceptibility at the center of the whisker for five different lengths. Theoretical points are for $\chi = \infty$; experimental points are from absolute calibration measurements. There are no adjustable parameters.

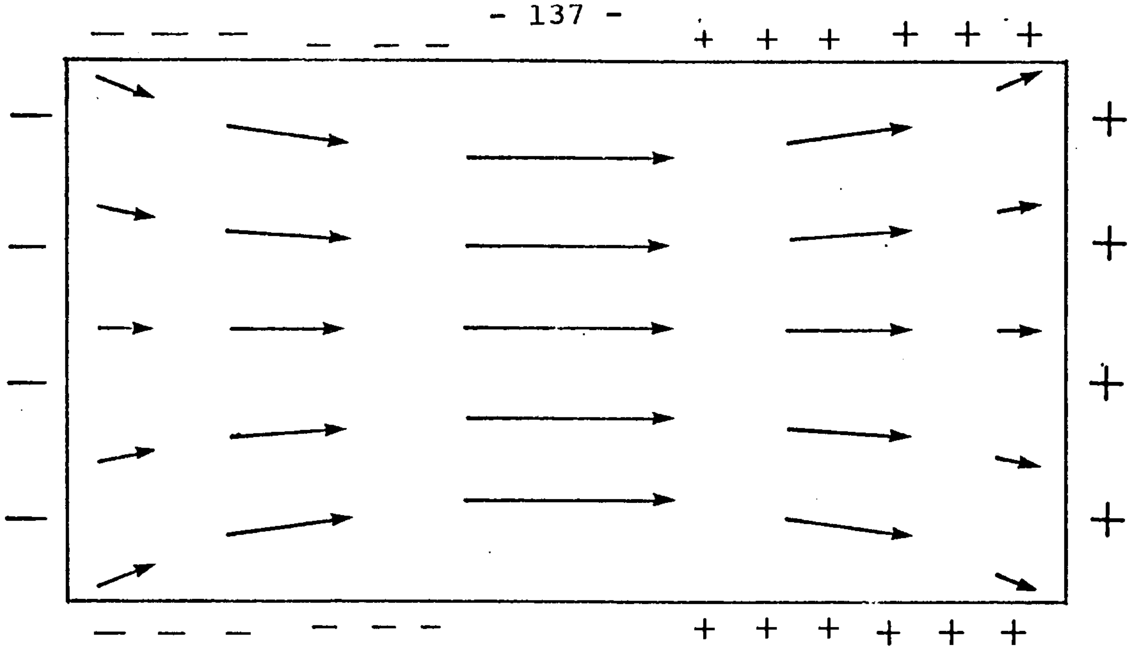

(a)

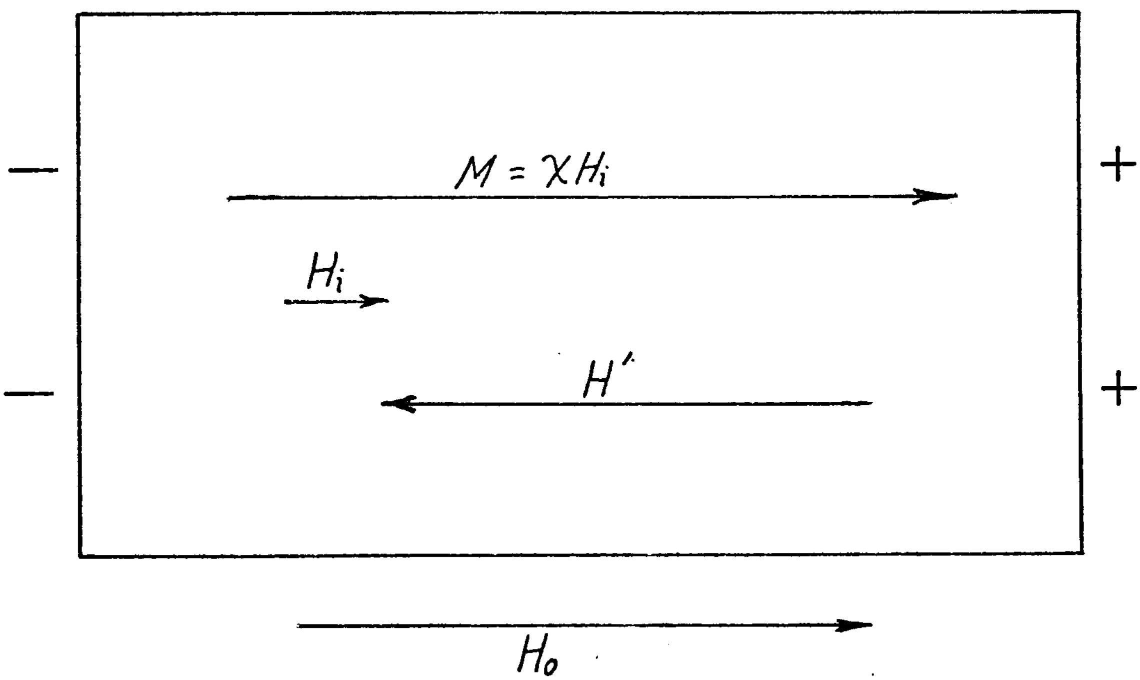

(b)

Fig. 5.5. (a) Magnetization and poles of infinite susceptibility bar in homogeneous field. Both length and direction of $\vec{M}$ change to make $\vec{\nabla} \cdot \vec{M} = 0$ everywhere inside. (b) Schematic illustration of self-consistency for finite χ. Relation between $\vec{M}$ and $\vec{H}'$ depends on bar shape and χ; relation between $\vec{M}$ and $\vec{H}_i$ depends only on χ.

to $\vec{H}_o$, gives an $\vec{H}_i$ which is identical to $\vec{M}/\chi$. For $\chi = \infty$, $\vec{H}'$ simply cancels $\vec{H}_o$ everywhere.

5.2.2 Local Driving Results

The field

$$H_o(z) = H_o \frac{1}{[1+\left(\frac{z}{r_c}\right)^2]^{3/2}} \hat{z}$$

is applied by a driving coil of radius r_c at $z = 0$, where $H_o\hat{z}$ is the field at the center of the coil. The resulting magnetization for $\chi = \infty$ is given in Fig. 5.6 for different coil radii and $\rho = .01$. [For a given r_c the $M(z)/M(0)$ curve is found to be quite independent of ρ.] This response is sensitive to r_c, since for $r_c < 3r$ (r is the cylinder radius) the magnetization is concave upward near the center. For $r_c = 3r$ the magnetization is linear over nearly the whole bar, and as $r_c \to \infty$ the magnetization goes to the homogeneous driving result.

The experimentally determined magnetization was slightly concave (Fig. 2.5) and the choice of $r_c = 2r$, a reasonable approximation to the experimental arrangement, fits it fairly well. Note from (3.12) that a local field model could only give a concave upward curvature where the applied field was locally reversed.

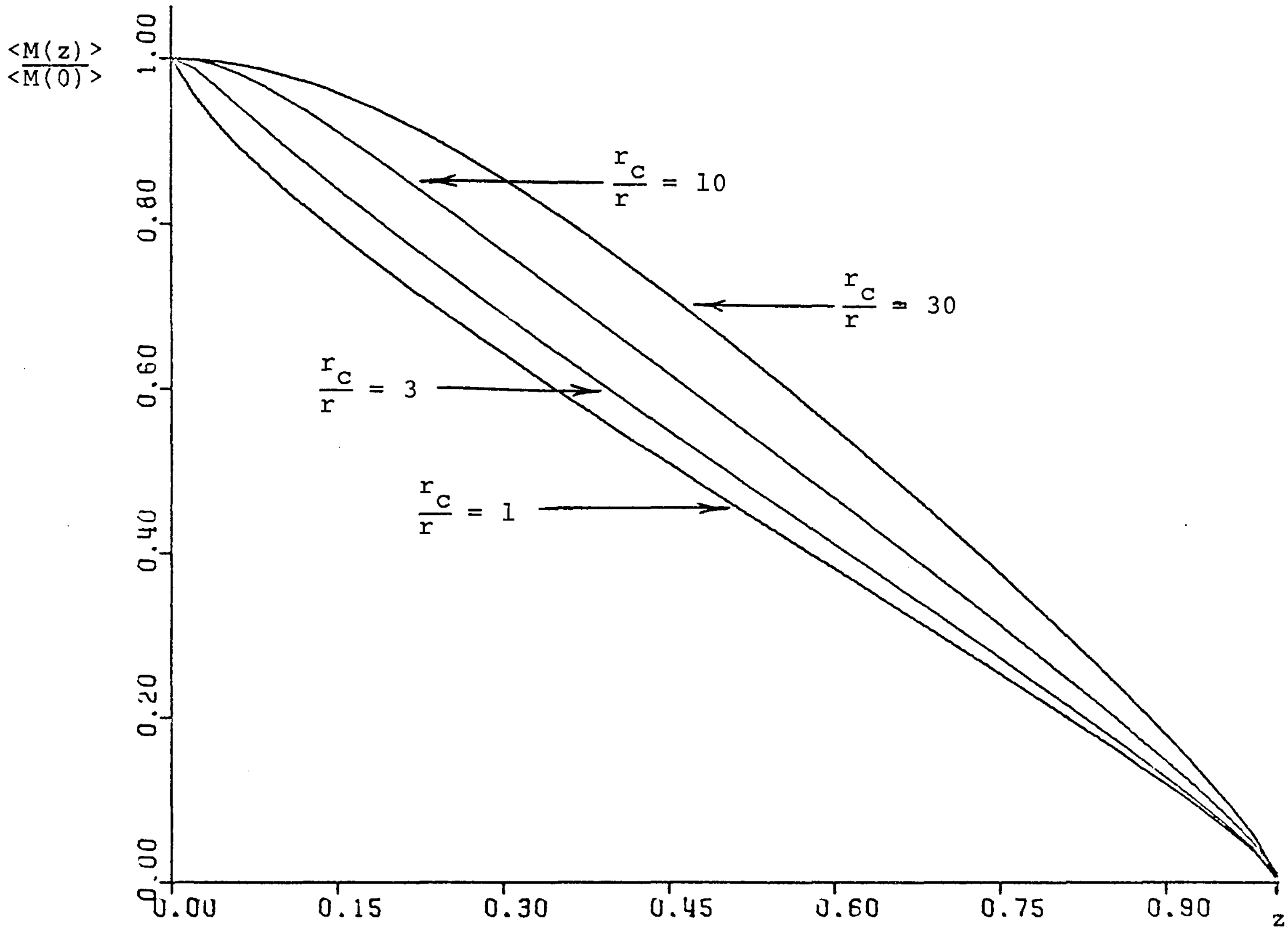

Fig. 5.6. Calculated normalized magnetization along a cylinder in local driving, for $\chi = \infty$ and $\rho = .01$. The driving coil radius r_c is a parameter.

CHAPTER 6

DISCUSSION

In this chapter we discuss and extend some of our previous results. Sec. 6.1 gives a more general discussion of the charge distribution in single crystals, which leads to a criterion for the use of demagnetizing factors in ferromagnetic samples. In Sec. 6.2 a rough treatment is presented of the magnetization curling pattern which results from competition between magnetostatic and exchange energies in the absence of anisotropy. The pattern is expected to be relatively temperature independent up to T_c. Sec. 6.3 compares the local model with the correct micromagnetic theory and extends the former to finite intrinsic susceptibility. Finally, Sec. 6.4 gives three broad areas into which our results should be extended.

6.1 Charge Distribution in Iron Single Crystals

We first show that the fraction of volume charge in a long whisker is of order $\left(\frac{d}{L}\right)^2$ or less, and then discuss more general domain configuration for single crystals. A criterion is established for the use of demagnetizing factors based on the intrinsic susceptibility, and a connection is made between χ and H_A for perfect single crystals.

6.1.1 Volume Charge in Long Crystals

The micromagnetic equations can be used in differential form to show that to good approximation there is no volume charge in the whisker. Equations (1.19) can be written

$$\frac{\partial U}{\partial x} + (H_A + H_o + H'_z)\frac{M_x}{M_s} = 0$$

$$\frac{\partial U}{\partial y} + (H_A + H_o + H'_z)\frac{M_y}{M_s} = 0 \quad . \tag{6.1}$$

Differentiating and using the fact that

$$\vec{H}_A >> \vec{H}_{i_z} = \vec{H}_o + \vec{H}'_z$$

we get

$$\frac{\partial^2 U}{\partial x^2} + 4\pi R \frac{\partial M_x}{\partial x} + \alpha \frac{\partial H'_z}{\partial x} = 0 \tag{6.2}$$

$$\frac{\partial^2 U}{\partial y^2} + 4\pi R \frac{\partial M_y}{\partial y} + \beta \frac{\partial H'_z}{\partial y} = 0 \quad ,$$

where $R = H_A/4\pi M_s$.

For long whiskers (and, in general, specimens with the z-dimension much larger than the other two),

$$\alpha \frac{\partial H'_z}{\partial x} << \frac{H_A}{M_s} \frac{\partial M_x}{\partial x} \tag{6.3}$$

$$\frac{\partial M_z}{\partial z} << \frac{\partial M_x}{\partial x} \sim \frac{\partial M_y}{\partial y} \tag{6.4}$$

and

$$\frac{\partial H'_z}{\partial z} \ll \frac{\partial H'_x}{\partial x} \sim \frac{\partial H'_y}{\partial y} . \tag{6.5}$$

Eqn. (6.3) follows from $\vec{H}$ being irrotational:

$$\frac{\partial H'_z}{\partial x} = \frac{\partial H'_x}{\partial z} ,$$

whence

$$\frac{\alpha \frac{\partial H'_x}{\partial z}}{\frac{H_A}{M_s} \frac{\partial M_x}{\partial x}} \sim \frac{\alpha \cdot \alpha H_{A/L}}{H_A \, \alpha/d} = \alpha \frac{d}{L} \ll 1.$$

Because M_z differs from M_s to order α^2 ,

$$\frac{\frac{\partial M_z}{\partial z}}{\frac{\partial M_x}{\partial x}} \sim \frac{\alpha^2 \, M_s/L}{\alpha \, M_s/d} = \alpha \frac{d}{L} \ll 1. \tag{6.4}$$

When $\alpha \approx \frac{d}{L}$, the whisker is saturated at the center, so in general

$$\langle M \rangle_{z=0} \sim M_s \, \alpha \frac{L}{d} .$$

Since $D \sim (\frac{d}{L})^2$,

$$|H'_z| \sim 4\pi D \langle M \rangle_{z=0} \sim 4\pi \frac{d}{L} M_s \alpha ,$$

and (6.5) follows:

$$\frac{\frac{\partial H'_z}{\partial z}}{\frac{\partial H'_x}{\partial x}} \sim \frac{4\pi \frac{d}{L} M_s \alpha/L}{H_A \ \alpha/d} = \frac{4\pi M_s}{H_A} \left(\frac{d}{L}\right)^2 << 1.$$

We first consider the initial magnetization (the limit of arbitrarily small α). Adding eqns (6.2) and then using (6.3, 6.4, 6.5) to eliminate quantities higher than order α on the RHS,

$$\nabla^2 U = -4\pi R\, \vec{\nabla}\cdot\vec{M} + \frac{\partial^2 U}{\partial z^2} + 4\pi R \frac{\partial M_z}{\partial z} - \alpha\left(\frac{\partial H'_z}{\partial x} + \frac{\partial H'_z}{\partial y}\right) \quad (6.6a)$$

$$\cong -4\pi R\, \vec{\nabla}\cdot\vec{M} - \frac{\partial H'_z}{\partial z} . \quad (6.6b)$$

Since $\frac{\partial H'_z}{\partial z} << \frac{\partial H'_x}{\partial x}$, one is tempted to ignore this term in (6.6). However, we are really comparing $\frac{\partial H'_z}{\partial z}$ with $\frac{\partial H'_x}{\partial x} + \frac{\partial H'_y}{\partial y}$ (or with $\frac{\partial M_x}{\partial x} + \frac{\partial M_y}{\partial y}$), and as we saw in Chapter 4,

$\frac{\partial H'_x}{\partial x} \approx -\frac{\partial H'_y}{\partial y}$. Thus, this term must be considered. Comparing (6.6b) with (1.16),

$$\frac{\partial H'_z}{\partial z} = -4\pi(1+R)\,\vec{\nabla}\cdot\vec{M} = 4\pi(1+R)\,\rho. \qquad (6.7)$$

If $\vec{\nabla}\cdot\vec{M} = 0$, then H'_z = constant ($= -H_o$) as expected from the infinite susceptibility analogy (Sec. 4.3.2) of the electric field in an ideal conductor. From (6.7) we calculate the volume charge Q_V and compare it to the total charge Q_T in a region of length Δz. In terms of the slope of the wall θ,

$$Q_T = 2\, M_s \theta d\, \Delta z \qquad (6.8a)$$

and

$$|Q_V| = |\rho|\, d^2\, \Delta z = \frac{d^2 \Delta z}{4\pi(1+R)} \left| \frac{\partial H'_z}{\partial z} \right|. \qquad (6.8b)$$

A dimensional argument is adequate. $|H'_z| \leq H_0$ with the equality holding only for infinite susceptibility. But H'_z can vary at most from zero to H_o in a distance $\frac{L}{2}$. In a typical part of the whisker, we then expect

$$\left| \frac{\partial H'_z}{\partial z} \right| \lesssim \frac{1}{L} \left[4\pi \left(\frac{d}{L} \right) M_s\, \theta \right],$$

and from (6.8a,b)

$$\frac{Q_V}{Q_T} \lesssim \left(\frac{d}{L} \right)^2. \qquad (6.9)$$

The restriction to initial magnetization is not necessary. Returning to (6.6a) and considering a finite bowing angle θ, we find (omitting numerical factors)

$$\frac{Q_V}{Q_T} \lesssim \left| -\left(\frac{d}{L}\right)^2 + R\frac{d}{L}\ \Theta \right| .$$

Now because $\Theta \lesssim \frac{d}{L}$,

$$\frac{Q_V}{Q_T} \lesssim \left(\frac{d}{L}\right)^2$$

for any wall displacement in the linear χ' region.

6.1.2 Wall and Surface Charge

We can indicate the generality of the previous results for wall and surface charge by considering two simple variations on the Landau configuration. The first variation is a long thick iron crystal with N parallel 180° walls of width d running along its length. In the absence of an applied field we expect no net magnetization. When a field is applied we expect that the walls will bow and the tie points will be displaced. For an arbitrary segment of the whisker the N walls make angles θ_i with the long axis. This segment of the crystal will have the same net charge per unit length,

$$2\ M_s d \sum_{i=1}^{N} \theta_i \quad ,$$

as an equivalent one in the Landau configuration with wall angle

$$\Theta = \sum_{i=1}^{N} \Theta_i \quad ,$$

by the argument of Fig. 3.1.

Micromagnetic self-consistency at the i^{th} wall requires the charge/unit length on the wall to be $\frac{2R}{1 + R} M_s \Theta_i d$. It follows that $\frac{R}{1 + R}$ (=2.3 percent at room temperature) of the total charge is on the 180° walls, independent of N or the spacing between walls.

Another variation on the Landau structure is the diamond domain (Fig. 6.1a) which has been observed in whiskers (Sc-57, Co-58, De-58b, Fo-61, Ha-70) and platelets (Ge-66). In a magnetic field this configuration appears as in Fig. 6.1b. The slope of the 180° walls (which are curved, as in the magnetized Landau structure) is small. If the 90° walls of the diamond domain make 45° angles with the whisker axis and the magnetization is along the easy axis everywhere, there will be no poles on the 90° walls. This is the zeroth order approximation to the magnetization (in the same sense that a uniform magnetization within the domains in the magnetized Landau structure is zeroth order). It is a simple exercise to see that in this approximation the existence of the diamond has no effect on the average magnetization in the cross-section.

If we now let the zeroth order magnetization relax under the influence of the demagnetizing fields which arise from the charge on sloping 180° walls, in addition to the charge mainly going to the surfaces we expect the 90° walls to become slightly charged ($\sim$2 percent again). These walls should bend slightly to increase the volume of the domains parallel

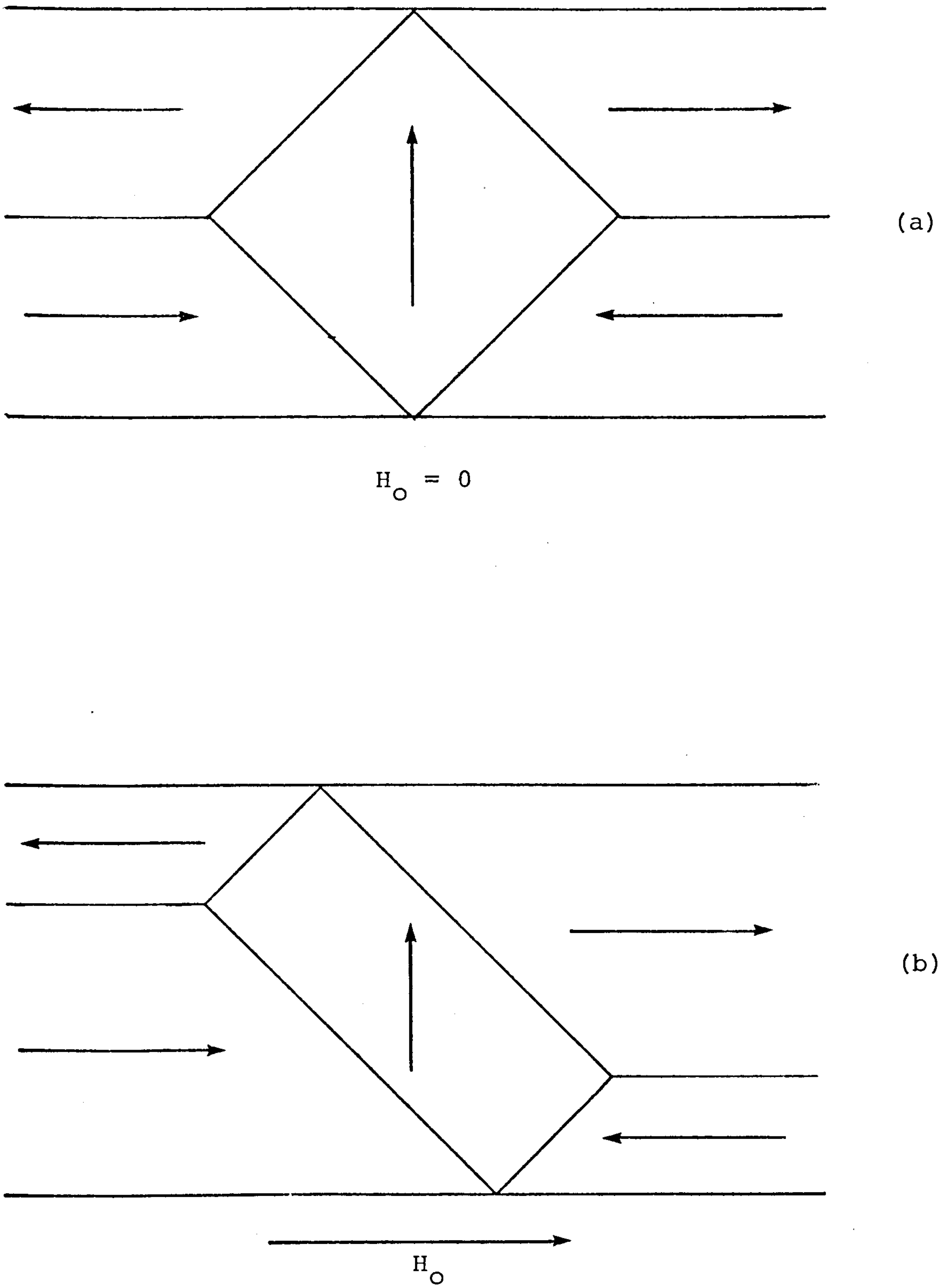

Fig. 6.1. Diamond domain in (a) unmagnetized and (b) magnetized whisker. Magnetization is shown in zeroth order approximation (uniform within the domains).

to H_o and decrease the antiparallel domains. The volume charge of the diamond domain should still be negligible. In this case, the $\frac{\partial M_y}{\partial y}$ is cancelled by the $\frac{\partial M_z}{\partial z}$ of the large transverse magnetization. (In the Landau configuration it was cancelled by the $\frac{\partial M_x}{\partial x}$ of the longitudinal magnetization).

In general we expect the existence of diamonds (or any other domain structure) should not affect the measured susceptibility in any appreciable way. The demagnetizing energies should be independent of the domain structure and the pole distribution should not be significantly different from that of the magnetized Landau configuration, as long as saturation is not reached anywhere along the length.

6.1.3 Use of the Demagnetizing Factor

That most of the charge will be on the surface of magnetized iron single crystals is apparently not generally appreciated. Gemperle et al (Ge-69) state that the poles in single-crystal platelets are on the domain walls. Most authors only draw arrows parallel to the easy axes, indicating uniform magnetization within domains. But Neél (Ne-44a,b) long ago appreciated the true situation.

Because the poles are on the surface, the demagnetizing fields can be found from the model of Chapter 5 with large χ. For good single crystals (with the exception of the picture frame) χ is much greater than $\frac{1}{4\pi D}$ for the dimensions which have been grown. In our experiments $\chi = \infty$ within experimental accuracy.

Theoretically, we can convert a non-zero H_A to a finite intrinsic susceptibility $\chi(H_A)$ through

$$\frac{1}{\chi'_{theo}} - \frac{1}{\chi(H_A)} = 4\pi D. \qquad (6.10)$$

χ'_{theo} isthe expected measured susceptibility when the increase in stiffness due to anisotropy is considered, and is found from (4.24):

$$\frac{\frac{1}{4\pi D} - \chi'_{theo}}{\frac{1}{4\pi D}} \sim .01. \qquad (6.11)$$

Then

$$\chi(H_A) \sim \frac{100}{4\pi D} \sim 10^4, \qquad (6.12)$$

which is strongly shape (length) dependent. To measure this it would be necessary to have absolute χ' measurements to better than 1 percent. Besides anisotropy, any imperfections and inhomogeneities would cause χ to decrease. In good whiskers the major contribution to this "intrinsic" susceptibility is probably from anisotropy. Williams et al (Wi-49) measured the intrinsic susceptibility of Fe (.03Si) picture frame crystals to be $\sim 10^6$, which is expected from the increase in wall energy alone. The whiskers should be at least as good as alloy crystals.

For soft polycrystalline ferromagnets the demagnetizing factor has the same use, but one must be careful to use the infinite χ model only for specimens with $\chi \gg \frac{1}{4\pi D}$. Without any assumptions about the M vs. H_i curve for such samples, we know that for large enough D most of the poles will be on the surface, because for those shapes the sample is responding as if $\chi = \infty$. The energy is entirely magnetostatic. In the low susceptibility $\chi \ll \frac{1}{4\pi D}$ limit the demagnetizing energy from the external surface charge is small, and the response of the sample is determined by the internal magnetization processes.

6.2 Curling Pattern for $H_A = 0$; Estimate of Wall Thickness

At temperatures near but below T_c the anisotropy is small. The ground state of a whisker at these temperatures is probably a curling pattern with a 180° wall separating two regions of opposite magnetization. The thickness of this wall is determined from the competition between exchange (which favors a thick wall) and magnetostatic energy (which favors a thin wall because of the poles at the surface). We will see that this competition results in a wall of thickness t ~ 1000 Å which is twice the room temperature Bloch wall thickness in the usual calculation (Chikazumi, Physics of Magnetism, p. 188).

We expect a Bloch-type wall everywhere except near its intersection with the surface, where the wall should be Néel-type to avoid large demagnetizing fields. La Bonte's result (La-69) for the 180° wall in thin films (but with uniaxial anisotropy in the plane of the film) was of this form. The wall should thicken somewhat away from the crystal surface.

A rough value for the wall thickness t near the surface is found by assuming that the wall is Bloch-type even at the surface, and that the resulting charge density at the surface is M_s for the entire wall thickness. This will lead to an overestimate of the demagnetizing energy. The magnetostatic energy of two parallel strips of charge density M_s, width t, and length L, a distance d apart is

$$U_d \approx 2\, M_s^2(T)\, L t^2 \left[\ln \frac{2L}{t} + \frac{1}{2} \right] , \qquad (6.13)$$

where we assume

$$\frac{t}{L} \ll 1 \quad \text{and} \quad \frac{t}{d} \ll 1. \tag{6.14}$$

The latter assumption will be verified (6.17) and means the interaction energy between the two charge strips is neglected compared to the self-energy of each strip.

The exchange energy at temperature T is

$$U_{ex} = NJ\psi^2 \left[\frac{M_s(T)}{M_s(0)}\right]^2 \tag{6.15}$$

where

$$N = \frac{Ltd}{a^3}$$

is the number of atoms in the wall and

$$\psi = \pi \frac{a}{t}$$

is the angle between adjacent spins. The term in brackets in (6.15) accounts for the decrease with rising temperature in the expectation value of the Heisenberg Hamiltonian $(\langle\vec{S}_i\rangle \cdot \langle\vec{S}_j\rangle)$. This decrease is due to thermal fluctuations of the magnetization. Then

$$U_{ex} = \frac{J\pi^2 Ld}{at} \left[\frac{M_s(T)}{M_s(0)}\right]^2 \tag{6.16}$$

and variation of t to minimize $U_d + U_{ex}$ gives

$$t^3 = \frac{\pi^2}{4 \ln\left[\frac{2L}{t} + \frac{1}{2}\right]} F \frac{d}{a}, \tag{6.17}$$

where $F = J/M_s^2(0)$ is given in Table 1.1. Note that since both the demagnetizing and exchange energies have the same temperature dependence ($M_s^2(T)$), the wall thickness is independent of temperature. The wall thickness is virtually independent of L and only weakly dependent on d. For the whiskers studied, $t \sim 1000$ Å $<<$ d, which is an <u>under</u>estimate of t because we <u>over</u>estimated the magnetostatic energy. This value is temperature independent, so the 180° wall exists right up to T_c.

6.3 Local Model Revisited

6.3.1 Critique

The demagnetizing fields in the local model are far from correct. We have already seen that for a typical whisker $L/d \sim 50$) the longitudinal demagnetizing field from the local model is only about one-half the true demagnetizing field, and points in different directions on each side of the wall. In reality, the longitudinal field arising from charge on the wall is small. Most of the demagnetizing field actually comes from charge on the surface. The internal field is very small for a whisker of high susceptibility ($\chi >> \frac{1}{4\pi D}$) because the demagnetizing field cancels H_o everywhere to good approximation.

The demagnetizing energy (3.10) can also be seen to be incorrect.* If the crystal thickness in the direction perpendicular to the wall were d', then

$$E_d \propto d' \int \sigma_w^2 \, dz.$$

Because the surfaces are in fact uncharged, d' can only affect the self-energy of the end charge and the interaction energy of the end and wall charge. The former is a constant and the latter depends only linearly on σ_w. Hence (3.10) is clearly wrong. In view of all the incorrect assumptions of the local model, how can it predict <u>anything</u> correctly?

---

* W.F. Brown, Jr., private communication.

Consider the demagnetizing energy in the local model:

$$E_d = - \tfrac{1}{2}\int \vec{M}\cdot\vec{H}'\, d\tau \,. \qquad (6.18)$$

$\vec{M}\cdot\vec{H}' = - M_s\,|\vec{H}'|$ only depends on $\vec{H}'$, and M_s can be taken out of the integral:

$$E_d = \tfrac{1}{2}\, M_s \int |H_z'|\, d\tau. \qquad (6.19)$$

The dependence of E_d on H_o comes only from H_z', since

$$H_z' \sim 2\pi\,\sigma_w\,\Theta = 4\pi M_s\,\Theta^2, \qquad (6.20)$$

where upon variation of the wall to minimize the total energy, it is found that

$$\Theta \propto x_1 \propto \frac{H_o}{M_s}\,. \qquad (6.21)$$

x_1 is the deflection at the center of the wall. The result is that

$$E_d \propto H_o^{\,2}\,, \qquad \text{(independent of } M_s) \qquad (6.22)$$

and in addition the wall shape is accurately predicted.

The true situation (for $\chi=\infty$) is that $H' = H_o$ can be taken out of the integral and

$$E_d = - \tfrac{1}{2}\int \vec{M}\cdot\vec{H}'\, d\tau = \tfrac{1}{2}\,\vec{H}_o\cdot\int \vec{M}\, d\tau = -\tfrac{1}{2}\, E_m \,. \qquad (6.23)$$

If the wall shape is independent of H_o, then

$$\left| \int \vec{M} \, d\tau \right| \quad \propto \quad x_1 \, . \tag{6.24}$$

To show the measured susceptibility is linear ($x_1 \propto H_o$), use the model of Chapter 5. When $\chi = \infty$,

$$H_o = 4\pi \, DM$$

where D is independent of M and H_o. Then

$$\int \vec{M} \, d\tau \propto \vec{H}_o \tag{6.25}$$

and again $E_d \propto H_o^2$.

Thus although the local model results for both the demagnetizing field (6.20) and the dependence of the demagnetizing energy in terms of this field (6.19) are incorrect, the errors cancel. The experimentally verifiable predictions that the demagnetizing energy should vary as H_o^2 (or as x_1^2) and should be independent of M_s are correct.

In his ripple theory Hoffmann approximated the non-local demagnetizing field by a local field proportional to the second derivative of the magnetization (Ho- 68a, b). This introduces errors (Br-70) but is presumably a fair approximation when the variations in the magnetization are rapid enough.

The approximation in the local model is of the same form, but no such justification can be made. In fact, the only justification for developing and using this model is that it also gives reasonably accurate descriptions of complicated phenomena such as the susceptibility at high frequency, when both the demagnetizing field and the field from eddy-currents are non-local (He-72).

6.3.2 Extension to Finite Susceptibility

The local model can be extended to include the effects of finite intrinsic susceptibility. We consider a long whisker and use the equivalence

$$< M_z > d^2 \equiv M_s \, x \, d, \tag{6.26}$$

where x is the displacement of the wall. Then

$$\frac{d<M_z>}{dz} = \frac{M_s}{d} \frac{dx}{dz} ,$$

and (3.12) can be written

$$H' = - H_0 , \tag{6.27a}$$

where

$$H' = 2\pi d^2 \frac{d^2<M_z>}{dz^2} . \tag{6.27b}$$

The numerical constant in (6.27b) is wrong. Using (3.38c) we can correct it to

$$H' = P \frac{d^2 \langle M_z \rangle}{dz^2}, \tag{6.28a}$$

where

$$P = 4 \left[\ln \frac{2L}{d} - \frac{5}{6} - \left(\frac{\pi + \ln 2}{4} \right) \right] d^2. \tag{6.28b}$$

This is a very good approximation to the demagnetizing field when H_o is uniform.

Now consider an "equivalent" bar (of square or circular cross-section) with an intrinsic susceptibility χ. Using (5.9) and (6.28a), we get the magnetization equation

$$P \frac{d^2 \langle M_z \rangle}{dz^2} = - H_o + \frac{\langle M_z \rangle}{\chi}. \tag{6.29}$$

The following special cases are of interest:

(i) H_o uniform, $\chi \to \infty$. The solution is the quadratic wall.

(ii) H_o uniform, $\chi \to C$. $H' \to 0$ faster than $\frac{\langle M_z \rangle}{\chi}$, which then equals H_o. (uniform magnetization).

(iii) $H_o = 0$. Then

$$< M_z (z)> = < M_z (0)>e^{- z/\ell} \tag{6.30}$$

where $\ell = \sqrt{P \chi}$ is a characteristic length of the material. The numerical value of P in (6.28b) may not be correct for non-uniform H_o . For a non-linear material with $\chi(M)$,

$$<M_z (z)> = <M_z (0)>\exp\left[-\int_o^z \frac{dz'}{\sqrt{P \chi (M (z'))}}\right].$$

The general solution for H_o uniform and χ constant is

$$< M_z (z)> = \chi H_o \left[1 - \frac{\cosh (z/\ell)}{\cosh (z/2\ell)}\right] \tag{6.31}$$

This magnetization is similar to that found numerically in Chapter 5 (Fig. 5.2).

Equation 6.29 must be considered phenomenological at this time. It can be used to predict effects of stray fields (e.g. from magnetic tape heads) on magnetic materials, and because of its simplicity might be useful near T_c where the susceptibility is finite.

6.4 Extensions of the Thesis

There are three obvious extensions of this work. The first is to the a.c. response of iron whiskers. The non-local equations for both the demagnetizing fields and the fields of the eddy-currents have not yet been worked out. Once this is done, accurate numerical calculations should be possible.

Second, the work should be extended to high temperature. Of most interest is the behavior around T_c. Experiments on iron whiskers near T_c are in progress (Ar-72a), but the role of dipole fields (from fluctuations in the magnetization) in the ferromagnetic phase transition has not been quantitatively worked out (Ar-72b, Ar-72c). Although the micromagnetic equations have been generalized to variable M_s (Mi-70), to date there is no simple theory of the behavior near T_c which incorporates an equation of state.

Third, the concepts developed for the magnetization of single crystals should help in the understanding of technical magnetization in polycrystalline ferromagnets of large grain size.

CHAPTER 7

SUMMARY

The micromagnetic equations have been solved in differential form to show that the volume charge in a long ferromagnetic single crystal is negligible, even for large anisotropy. These equations have been used in integral form to find the magnetization in the long domains of an iron whisker in the Landau configuration. The whisker is illustrated greatly foreshortened in Fig. 6.2. The important features are

(i) the 180° wall bows nearly quadratically,

(ii) the tie points are deflected to increase the magnetization,

(iii) the magnetization is non-uniform in the domains, being nearly parallel to the wall at the wall, and less curved at the surface, and

(iv) the magnetization changes within the domain so as to create virtually no volume charge and put all but 2.3 percent of the charge on the surfaces.

Facts (i) and (ii) were in essence known from photographs showing the response to an applied field of 180° walls in thin iron platelets. This thesis gives a theoretical basis

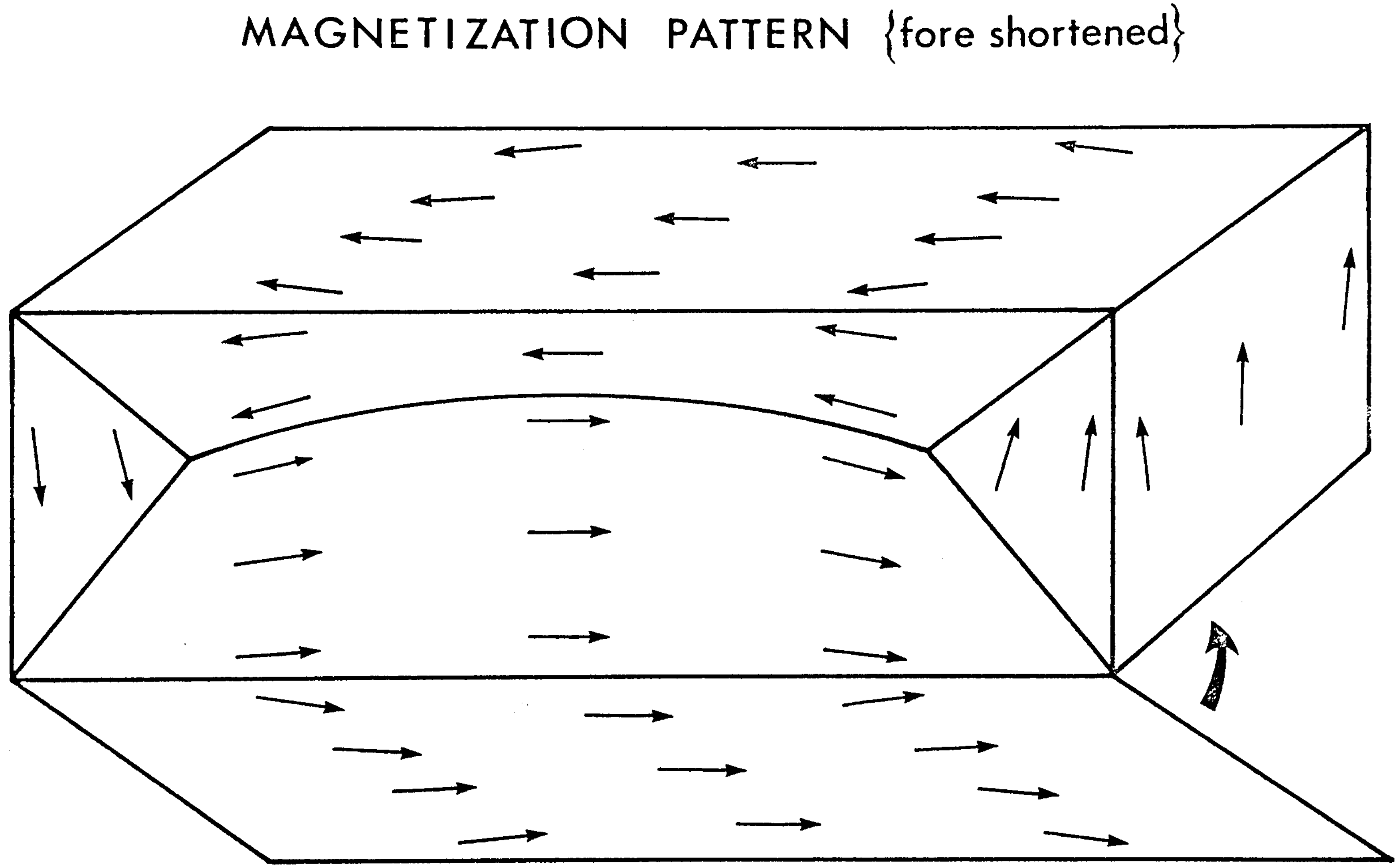

Fig. 7.1. Foreshortened representation of magnetization in whisker in homogeneous applied field. Note that $\vec{\nabla}\cdot\vec{M} = 0$ within all domains.

for (i). The features of the magnetization distribution in the long domains, (iii) and (iv), were not previously understood. We have also shown that (iv) is a general result, independent of the actual domain structure, for iron single crystals.

APPENDIX 1

EVALUATION OF DEMAGNETIZING ENERGIES

A. Interaction energy of lines of charge representing quadratic magnetization

The integral we need is

$$I(s) = \int_{-L/2}^{L/2} zdz \int_{-L/2}^{L/2} z'dz' \frac{1}{[(z-z')^2+s^2]^{\frac{1}{2}}} .$$

Let $z = \frac{L}{2}\bar{z}$, $z' = \frac{L}{2}\bar{z}'$, and $s = \frac{L}{2}\bar{s}$, and remove the bars from the variables of integration. Then

$$I(\bar{s}) = \left(\frac{L}{2}\right)^3 \int_{-1}^{1} zdz \int_{-1}^{1} z'dz \frac{1}{[(z-z')^2+\bar{s}^2]^{\frac{1}{2}}} .$$

With a change of variables the z' integral becomes

$$\int_{-1}^{1} z'dz' \frac{1}{[(z-z')^2+\bar{s}^2]^{\frac{1}{2}}} = \left[z \ln\left(z'+\sqrt{z'^2+\bar{s}^2}\right) - \sqrt{z'^2+\bar{s}^2}\right]\Bigg|_{z_-}^{z_+} ,$$

where $z_+ = z+1$ and $z_- = z-1$. We get

$$\frac{I(s)}{\left(\frac{L}{2}\right)^3} = I_1 + I_2 + I_3 + I_4$$

$$= \int_{-1}^{1} zdz \left[z \ln\left(z_+ + \sqrt{z_+^2+\bar{s}^2}\right)\right.$$

$$\left. -z \ln\left(z_- + \sqrt{z_-^2+\bar{s}^2}\right) - \sqrt{z_+^2+\bar{s}^2} + \sqrt{z_-^2+\bar{s}^2}\right] .$$

It is easy to see that $I_3 = I_4$, and a change of variables gives

$$I_3 = -\int_0^2 (z-1)\sqrt{z^2+\bar{s}^2}\, dz$$

$$= \left[\frac{z\sqrt{z^2+\bar{s}^2}}{2} + \frac{\bar{s}^2}{2}\ln\left(z+\sqrt{z^2+\bar{s}^2}\right) - \frac{(z^2+\bar{s}^2)^{3/2}}{3}\right]\Bigg|_0^2$$

For long whiskers, $\bar{s} << 1$, and

$$I_3 \approx -\frac{2}{3}\,.$$

With similar changes of variables,

$$I_1 = \int_0^2 (z-1)^2 \ln\left(z+\sqrt{z^2+\bar{s}^2}\right)dz$$

and

$$I_2 = \int_{-2}^0 (z+1)^2 \ln\left(z+\sqrt{z^2+\bar{s}^2}\right)dz$$

$$\underset{(z \to -z)}{=} \int_0^2 (z-1)^2 \ln\left(-z+\sqrt{z^2+\bar{s}^2}\right)dz.$$

Using Dwight (625., 625.1, 625.2) and equivalent integrals for $-z$, and setting $r = \sqrt{z^2+\bar{s}^2}$, we find

$$I_1 + I_2 = \Bigg\{\left[\frac{z^3}{3}\ln\left(\frac{z+r}{-z+r}\right) - \frac{2r^3}{9} + \frac{2\bar{s}^2 r}{3}\right]$$

$$-2\left[\left(\frac{z^2}{2} + \frac{\bar{s}^2}{4}\right)\ln\left(\frac{z+r}{-z+r}\right) - \frac{zr}{2}\right]$$

$$+ \left[z\ln\left(\frac{z+r}{-z+r}\right) - 2r\right]\Bigg\}\Bigg|_0^2 .$$

Again for $s << 1$,

$$I_1 + I_2 \approx \frac{4}{3}\left[\ln\frac{4}{s} - \frac{4}{3}\right]$$

and finally,

$$I(s) = \frac{4}{3}\left(\frac{L}{2}\right)^3\left[\ln\frac{2L}{s} - \frac{7}{3}\right]. \tag{A1.1}$$

B. <u>Energy for charges in whisker and on an equivalent cylinder</u>

Case (i): Charges on the wall.

From (3.37), the demagnetizing energy is

$$E_w = \frac{2L}{3}\sigma_0^2\frac{1}{2}\int_0^d dy\int_0^d dy'\left(\ln\frac{2L}{|y-y'|} - \frac{7}{3}\right).$$

To avoid infinities, integrate requiring $y \geq y'$:

$$\int_0^d dy\int_0^d dy' \ln|y-y'| = 2\int_0^d dy\int_0^y dy' \ln(y-y')$$

$$= 2\int_0^d (y\ln y - y)dy = d^2(\ln d - \tfrac{3}{2}),$$

using

$$\lim_{y\to 0}(y\ln y) = 0.$$

Then

$$E_w = \frac{L}{3}\sigma_0^2 d^2\left[\ln\frac{2L}{d} - \frac{5}{6}\right] = \tfrac{1}{2}\gamma_w\frac{M_s^2 d^2}{L}x_1^2$$

where

$$\gamma_w \equiv \frac{128}{3}\left[\ln\frac{2L}{d} - \frac{5}{6}\right]. \tag{A1.2}$$

Case (ii): Charges on two parallel surfaces.

We put half the charge on each surface.

Then

$$E_{2s} = 2 \cdot \frac{L}{3}\left(\frac{\sigma_0}{2}\right)^2 d^2\left[\ln\frac{2L}{d} - \frac{5}{6}\right] + E_1^{int}$$

where

$$E_1^{int} = \frac{2L}{3}\left(\frac{\sigma_0}{2}\right)^2 \int_0^d dy \int_0^d dy'\left[\ln\frac{2L}{\sqrt{(y-y')^2+d^2}} - \frac{7}{3}\right].$$

Using Dwight (623, 623.1, 525),

$$\int_0^d dy \int_0^d dy' \ln\left[(y-y')^2+d^2\right]$$

$$= 2\int_0^d dy\left[y \ln(y^2+d^2) - 2y+2d \tan^{-1}\frac{y}{d}\right]$$

$$= 2d^2\left[\ln d + \frac{\pi}{2} - \frac{3}{2}\right].$$

Thus

$$E_1^{int} = \frac{L}{6}\sigma_0^2 d^2\left[\ln\frac{2L}{d} - \frac{5}{6} - \frac{\pi}{2}\right] \tag{A1.3}$$

and

$$E_s = \frac{E_W}{2} + E_1^{int} = \frac{L}{3}\sigma_0^2 d^2\left[\ln\frac{2L}{d} - \frac{5}{6} - \frac{\pi}{4}\right]$$

$$= \tfrac{1}{2}\,\gamma_{2s}\frac{M_s{}^2 d^2}{L} x_1^2 ,$$

where

$$\gamma_{2s} \equiv \frac{128}{3}\left[\ln\frac{2L}{d} - \frac{5}{6} - \frac{\pi}{4}\right]. \tag{A1.4}$$

Case (iii): Charges on all four surfaces.

Put one quarter of the charge on each surface.

$$E_{4s} = 4 \cdot \frac{L}{3}\left(\frac{\sigma_0}{4}\right)^2 d^2 \left[\ln \frac{2L}{d} - \frac{5}{6}\right]$$
$$+ 2 \cdot \frac{L}{6}\left(\frac{\sigma_0}{2}\right)^2 d^2 \left[\ln \frac{2L}{d} - \frac{5}{6} - \frac{\pi}{2}\right]$$
$$+ 4 E_2^{int}$$

where

$$E_2^{int} = \frac{2L}{3} \left(\frac{\sigma_0}{4}\right)^2 \int_0^d dx \int_0^d dy \left[\ln \frac{2L}{\sqrt{x^2+y^2}} - \frac{7}{3}\right].$$

Now,

$$\int_0^d dx \int_0^d dy \ \ln(x^2+y^2) = \int_0^d dx \left[d \ln(x^2+d^2) - 2d + 2x \tan^{-1} \frac{d}{x}\right].$$

The first two terms give

$$d^2 \left[\ln 2d^2 - 4 + \frac{\pi}{2}\right].$$

The third becomes, letting $u = \frac{d}{x}$ and using Dwight (526.3),

$$2d^2 \int_1^\infty \frac{1}{u^3} \tan^{-1} u \, du = d^2 .$$

We get

$$E_2^{int} = \frac{2L}{3}\left(\frac{\sigma_0}{4}\right)^2 d^2 \left[\ln \frac{2L}{d} - \frac{5}{6} - \frac{\pi}{4} - \tfrac{1}{2} \ln 2\right] \tag{A1.5}$$

and

$$E_{4s} = \frac{L}{3} \sigma_0^2 \ d^2 \left[\ln \frac{2L}{d} - \frac{5}{6} - \left(\frac{\pi + \ln 2}{4}\right)\right]$$
$$= \tfrac{1}{2} \gamma_{4s} \frac{M_s{}^2 d^2}{L} x_1^2 ,$$

where

$$\gamma_{4s} \equiv \frac{128}{3} \left[\ln \frac{2L}{d} - \frac{5}{6} - \left(\frac{\pi + \ln 2}{4}\right)\right]. \tag{A1.6}$$

Case (iv): Charge on the surface of a cylinder.

We distribute the charge on the surface of a cylinder of area $\pi r^2 = d^2$. The charge/unit length is

$$\rho_\ell = \sigma(z)\ 2\pi r = \sigma_0 d\ \frac{z}{L/2}\ .$$

This gives

$$\sigma(z) = \sigma_0^C\ \frac{z}{L/2}\ ,$$

where

$$\sigma_0^C = \frac{\sigma_0 d}{2\pi r} = \frac{\sigma_0}{2\sqrt{\pi}}\ .$$

The demagnetizing self-energy (Fig. A1.1) is

$$E_C = \tfrac{1}{2} \cdot \frac{2L}{3}\int_0^{2\pi} r d\phi \cdot \int_0^{2\pi} r d\phi'\ \sigma_0^{C^2}\left[\ln \frac{2L}{s(\phi'-\phi)} - \frac{7}{3}\right]. \qquad \text{(A1.7)}$$

Because of cylindrical symmetry the ϕ' integration is independent of ϕ; we take $\phi = 0$. Then

$$E_C = \frac{2\pi r^2 L}{3} \cdot \sigma_0^{C^2}\int_0^{2\pi}\left[\ln\left(\frac{L}{r \sin \frac{\phi'}{2}}\right) - \frac{7}{3}\right] d\phi'\ .$$

From Dwight (630.1),

$$\int_0^{\pi} \ln\ (\sin\theta)\ d\theta = -\pi \ln 2.$$

Thus,

$$E_C = \frac{4\pi^2 L r^2 \sigma_0^{C^2}}{3} \cdot \left[\ln \frac{2L}{r} - \frac{7}{3}\right] = \tfrac{1}{2}\ \gamma_C\ \frac{{M_S}^2 d^2}{L}\ x_1^2\ ,$$

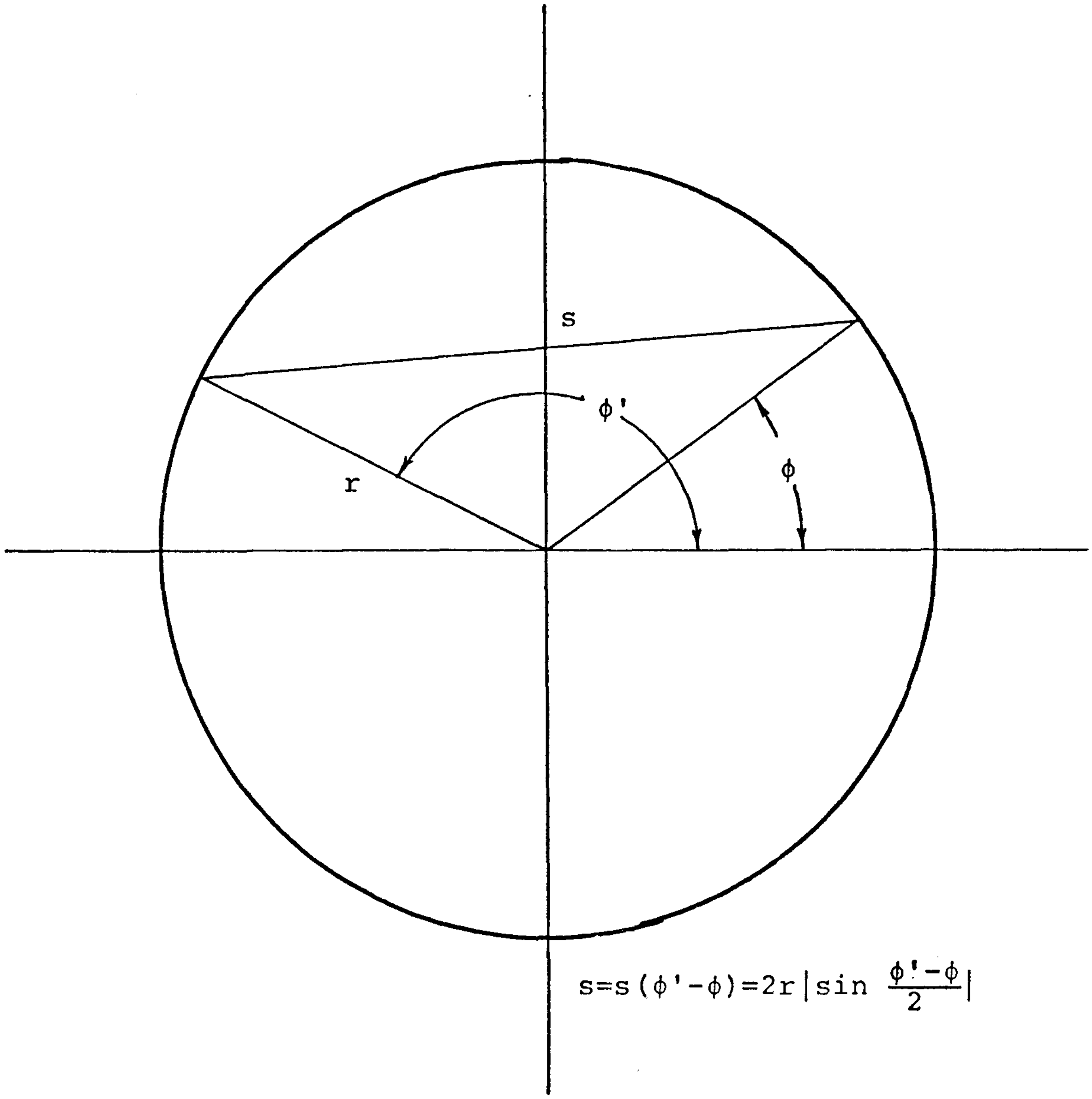

Fig. A1.1 Definition of integration variables for potential of cylindrical charge distribution.

where

$$\gamma_c \equiv \frac{128}{3}\left[\ln\frac{2\sqrt{\pi}L}{d} - \frac{7}{3}\right] . \tag{A1.8}$$

C. <u>Interaction and Self-Energy for Linear Magnetization</u>

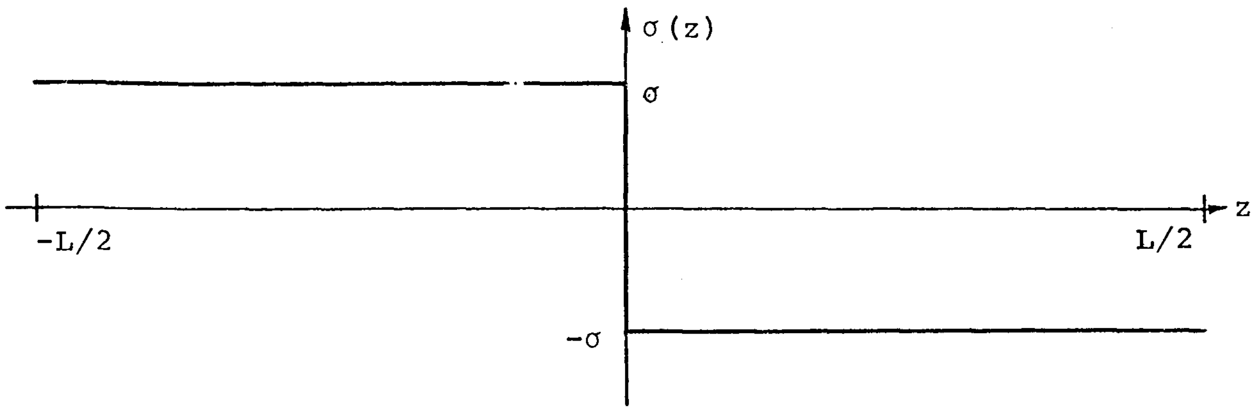

We first find the interaction energy of two strips of charge of width dy and dy', of charge density

$$\sigma(z) = \begin{cases} \sigma & -\frac{L}{2} \le z < 0 \\ -\sigma & 0 < z \le L/2 \end{cases}$$

and separated a distance s:

$$d^2E = dydy'\sigma^2\left[\left(\int_{-L/2}^{0} dz - \int_{0}^{L/2} dz\right)\left(\int_{-L/2}^{0} dz' - \int_{0}^{L/2} dz'\right)\frac{1}{\sqrt{(z-z')^2+s^2}}\right] .$$

Rewrite this as

$$d^2E = L\sigma^2 dydy'(I_1 + I_2),$$

where

$$I_1(\bar{s}) = \int_0^1 dz \int_0^1 dz' \frac{1}{\sqrt{(z-z')^2+\bar{s}^2}} ,$$

$$I_2(s) = -\int_0^1 dz \int_0^1 dz' \frac{1}{\sqrt{(z+z')^2+\bar{s}^2}} ,$$

and

$$\bar{s} = \frac{s}{L/2} .$$

I_1 comes from repulsion of charges on the same side of $z = 0$; I_2 comes from attraction of charges on opposite sides of $z = 0$. This is indicated schematically below:

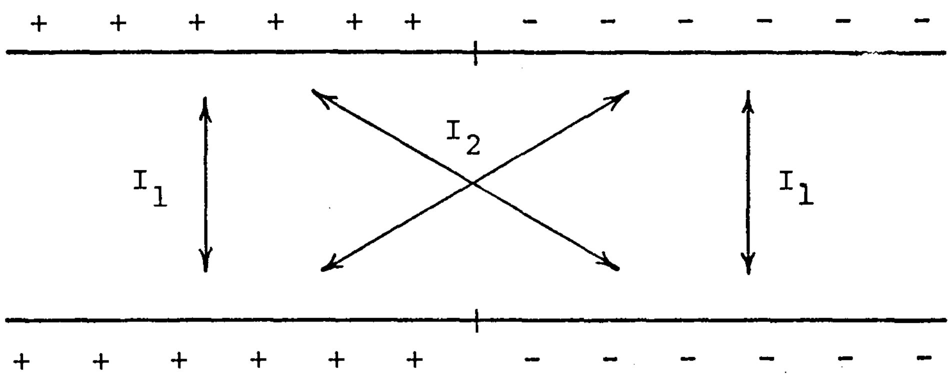

By inspection, $|I_1| > |I_2|$, so $d^2E > 0$. (For a general longitudinal magnetization, the I_1 type integral causes like charges to spread out, and the I_2 integral attempts to bring opposite charges together at $z = 0$. The actual magnetization is a compromise which minimizes $I_1 + I_2 + E_m$, where E_m is the magnetizing energy

$$E_m \propto -H_o \int_{-L/2}^{L/2} z'\sigma(z')dz').$$

To first order in $\bar{s}$,

$$I_1(\bar{s}) = 2\left(\ln \frac{2}{\bar{s}} - 1 + \bar{s}\right) ,$$

$$I_2(\bar{s}) = \bar{s} - 2 \ln 2 ,$$

and

$$d^2E = L\sigma^2 dy dy' \left[2 \ln \frac{L}{s} + \frac{6}{L} s - 2 - 2 \ln 2\right].$$

As in Appendix 1B, put the charge on the surface of a cylinder of area $\pi r^2 = d^2$. The charge/unit length is to be the same. By the corresponding argument of (3.36),

$$2\pi r\ \sigma = \frac{4M_s x_1}{L} d.$$

As in Fig. A1.1, $s = 2r|\sin \phi/2|$ and

$$E^L = \tfrac{1}{2} L\sigma^2 \cdot 2\pi r^2 \int_0^{2\pi} d\phi' \left[2 \ln \frac{L}{s} + \frac{6}{L} s - 2 - 2 \ln 2\right]$$

$$= \tfrac{1}{2} \gamma_c^L \frac{M_s{}^2 d^2}{L} x_1^2 ,$$

where

$$\gamma_c^L \equiv 32 \left[\ln \frac{\sqrt{\pi} L}{2d} - 1 + \frac{12d}{\pi^{3/2} L}\right] . \tag{A1.9}$$

APPENDIX 2

TWO PARAMETER ANALYTICAL SOLUTION TO THE TRANSVERSE MAGNETIZATION

The charges and fields of interest are indicated in this transverse view:

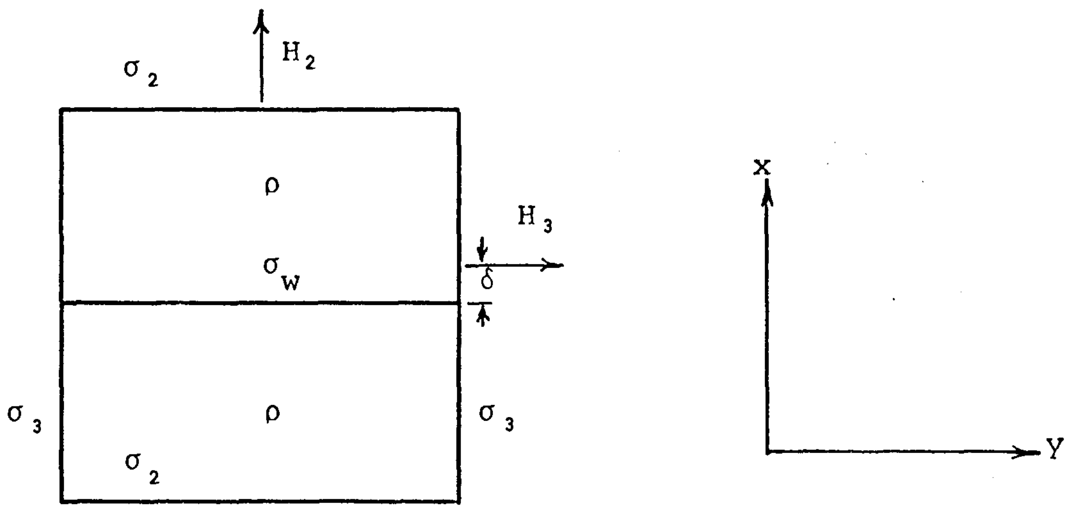

Define the fields at a point (x,y) due to an infinite strip of width d with charge density σ as shown:

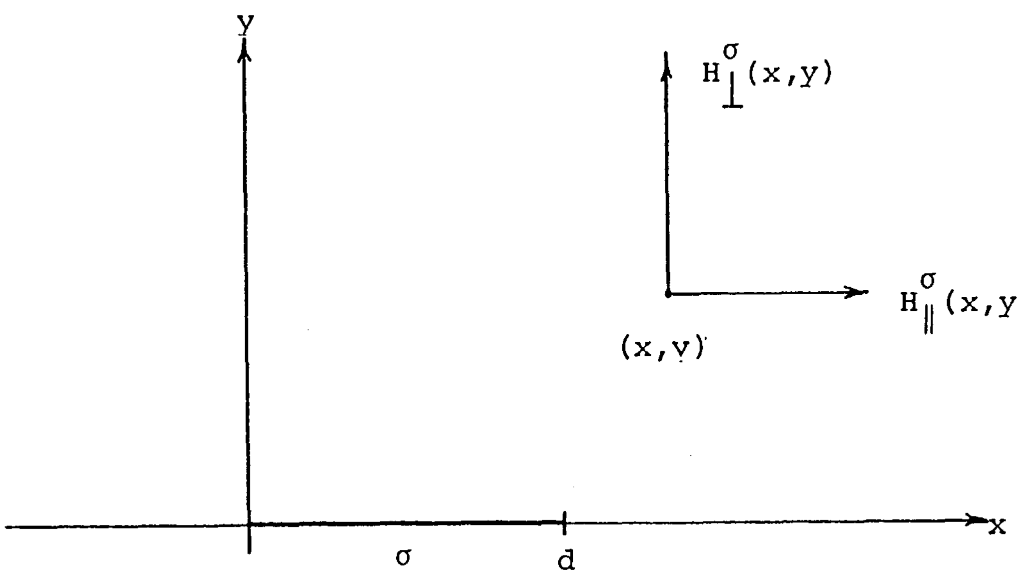

Then

$$H_{\perp}^{\sigma}(x,y) = \int_0^d dx' \int_{-\infty}^{\infty} dz' \frac{\sigma y}{[z'^2 + y^2 + (x - x')^2]^{3/2}}$$

$$= 2\sigma y \int_0^d dx' \frac{1}{(x - x')^2 + y^2} .$$

Redefining in terms of dimensionless variables

$$\bar{x} = \frac{x}{d} \quad \text{and} \quad \bar{y} = \frac{y}{d} ,$$

$$H_{\perp}^{\sigma}(\bar{x},\bar{y}) = 2\sigma \left[\tan^{-1} \frac{\bar{x}}{\bar{y}} - \tan^{-1} \frac{\bar{x} - 1}{\bar{y}}\right] . \qquad \text{(A2.1)}$$

Also,

$$H_{\parallel}^{\sigma}(x,y) = \int_0^d dx' \int_{-\infty}^{\infty} dz' \frac{\sigma\ (x - x')}{[z'^2 + y^2 + (x - x')^2]^{3/2}}$$

so

$$H_{\parallel}^{\sigma}\ (\bar{x},\bar{y}) = \sigma \ln \frac{\bar{x}^2 + y^2}{(\bar{x} - 1)^2 + \bar{y}^2} . \qquad \text{(A2.2)}$$

Define the field at (x,y) due to an infinite square bar of side d with charge density ρ as $H_{\perp}^{\rho}\ (x,y)$:

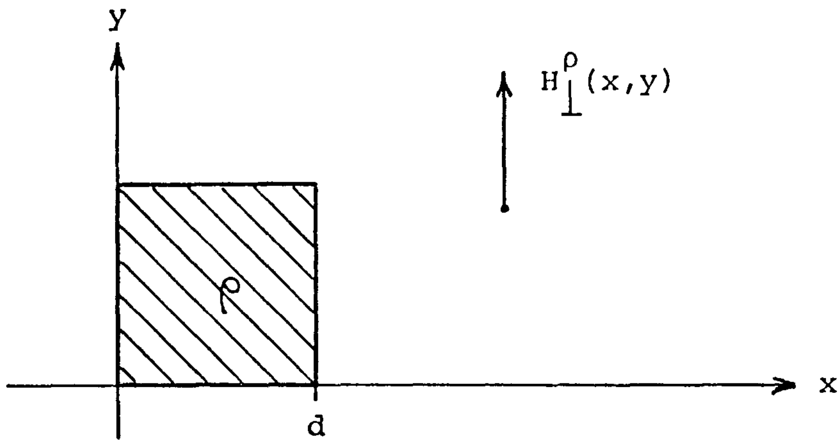

$$H_\perp^{\rho}(x,y) = \int_0^d dx' \int_0^d dy' \int_{-\infty}^{\infty} dz' \, \frac{\rho\,(y-y')}{[z'^2 + (y-y')^2 + (x-x')^2]^{3/2}}$$

or

$$H_\perp^{\rho}(\bar{x},\bar{y}) = \rho d \left[\bar{x} \ln \frac{\bar{x}^2+\bar{y}^2}{\bar{x}^2+(\bar{y}-1)^2} - (\bar{x}-1) \ln \frac{(\bar{x}-1)^2+\bar{y}^2}{(\bar{x}-1)^2+(\bar{y}-1)^2} \right.$$

$$\left. + 2\bar{y}\left(\tan^{-1}\frac{\bar{x}}{\bar{y}} - \tan^{-1}\frac{\bar{x}-1}{\bar{y}}\right) - 2(\bar{y}-1)\left(\tan^{-1}\frac{\bar{x}}{\bar{y}-1} - \tan^{-1}\frac{\bar{x}-1}{\bar{y}-1}\right)\right]. \quad (A2.3)$$

With these definitions,

$$\vec{H}_2 = \left[-2\pi\sigma_2 + 2H_\parallel^{\sigma_3}(1,\tfrac{1}{2}) + H_\perp^{\sigma_2}(\tfrac{1}{2},1) + H_\perp^{\rho}(\tfrac{1}{2},1) + H_\perp^{\sigma_W}(\tfrac{1}{2},\tfrac{1}{2})\right]\hat{x}$$

$$\vec{H}_3 = \left[-2\pi\sigma_3 + 2H_\parallel^{\sigma_2}(1,\tfrac{1}{2}) + H_\perp^{\sigma_3}(\tfrac{1}{2},1) + H_\perp^{\rho}(\tfrac{1}{2},1) + H_\parallel^{\sigma_W}(1,\delta)\right]\hat{y} \,. \quad (A2.4)$$

We take $H_\parallel^{\sigma_W}(1,\delta)$ because of the logarithmic divergence as $\delta \to 0$. From (A2.1, A2.2, A2.3),

$$H_{\parallel}^{\sigma}(1,\tfrac{1}{2}) = \sigma \ln 5$$

$$H_{\perp}^{\sigma}(\tfrac{1}{2},1) = 4\,\sigma \tan^{-1}\tfrac{1}{2}$$

$$H_{\perp}^{\rho}(\tfrac{1}{2},1) = \rho d\,[\,\ln 5 + 4\tan^{-1}\tfrac{1}{2}\,]$$

$$H_{\perp}^{\sigma}(\tfrac{1}{2},\tfrac{1}{2}) = 4\,\sigma \tan^{-1} 1 = \sigma\pi$$

$$H_{\parallel}^{\sigma}(1,\delta) = -2\sigma \ln \delta \;(\delta \ll 1)\;. \qquad \text{(A2.5)}$$

The self-consistency conditions are

$$\frac{H_2}{M_s\theta} = \frac{H_A\phi_2}{M_s\theta} = 4\pi R\Phi_2$$

$$\frac{H_3}{M_s\theta} = 4\pi R\Phi_3\;, \qquad \text{(A2.6)}$$

using

$$\Phi_1 = \frac{\phi_1}{\theta},\; R = \frac{H_A}{4\pi M_s},\; \text{and}\; \phi = \frac{H}{H_A}\; \text{(small angles)}.$$

Then using (4.1), (A2.4), (A2.5) and the definitions

$$A_1 = 2\pi$$

$$A_2 = 2\ln 5$$

$$A_3 = 4\tan^{-1}\tfrac{1}{2}$$

$$A_4 = 2\ln 5 + 8\tan^{-1}\tfrac{1}{2}$$

$$A_5 = 4\ln\delta,$$

equations (A2.6) become

$$4\pi R\Phi_2 = -A_1\Phi_2 + A_2\Phi_3 + A_3\Phi_2 + A_4(\Phi_1-\Phi_2-\Phi_3) + A_1(1-\Phi_1)$$

$$4\pi R\Phi_3 = -A_1\Phi_3 + A_2\Phi_2 + A_3\Phi_3 + A_4(\Phi_1-\Phi_2-\Phi_3) + A_5(1-\Phi_1).$$

These two equations are solved for Φ_2 and Φ_3 (Φ_1 is given by (4.2)), and the results are in Table 4.1.

APPENDIX 3

SOLUTION OF THE TRANSVERSE MICROMAGNETIC PROBLEM

The whisker has reflection symmetry about both the xz and yz planes when the wall is at $x = 0$, so the charge densities at the four points shown below are equal:

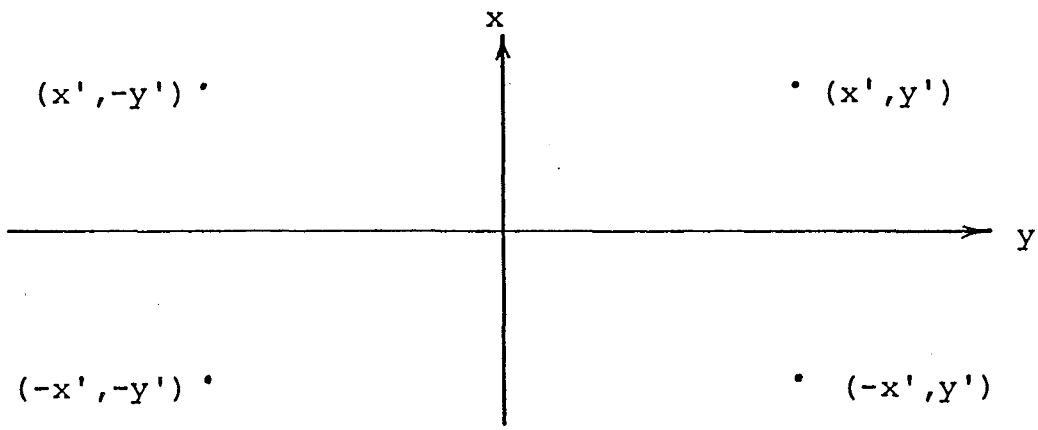

We use this to rewrite the first term in (4.3a) for the x-demagnetizing field at (x,y) due to volume charges throughout the whisker as

$$\frac{H_x'(x,y)}{M_s\theta} = \int_0^{L/2} dx' \int_0^{L/2} dy' \Big[K_x(x-x',\ y-y') + K_x(x-x',\ y+y')$$

$$+ K_x(x+x',\ y-y') + K_x(x+x',\ y+y')\Big] \times$$

$$\left[-\ \frac{\partial \Phi_x(x',y')}{\partial x'} - \frac{\partial \Phi_y(x',y')}{\partial y'}\right] . \qquad \text{(A3.1)}$$

We divide all variables by L/2 to make them dimensionless. This changes only the limits of integration because equations (4.3) are already dimensionless.

An m × m grid is set up for numerical evaluation of this field, as described in the text:

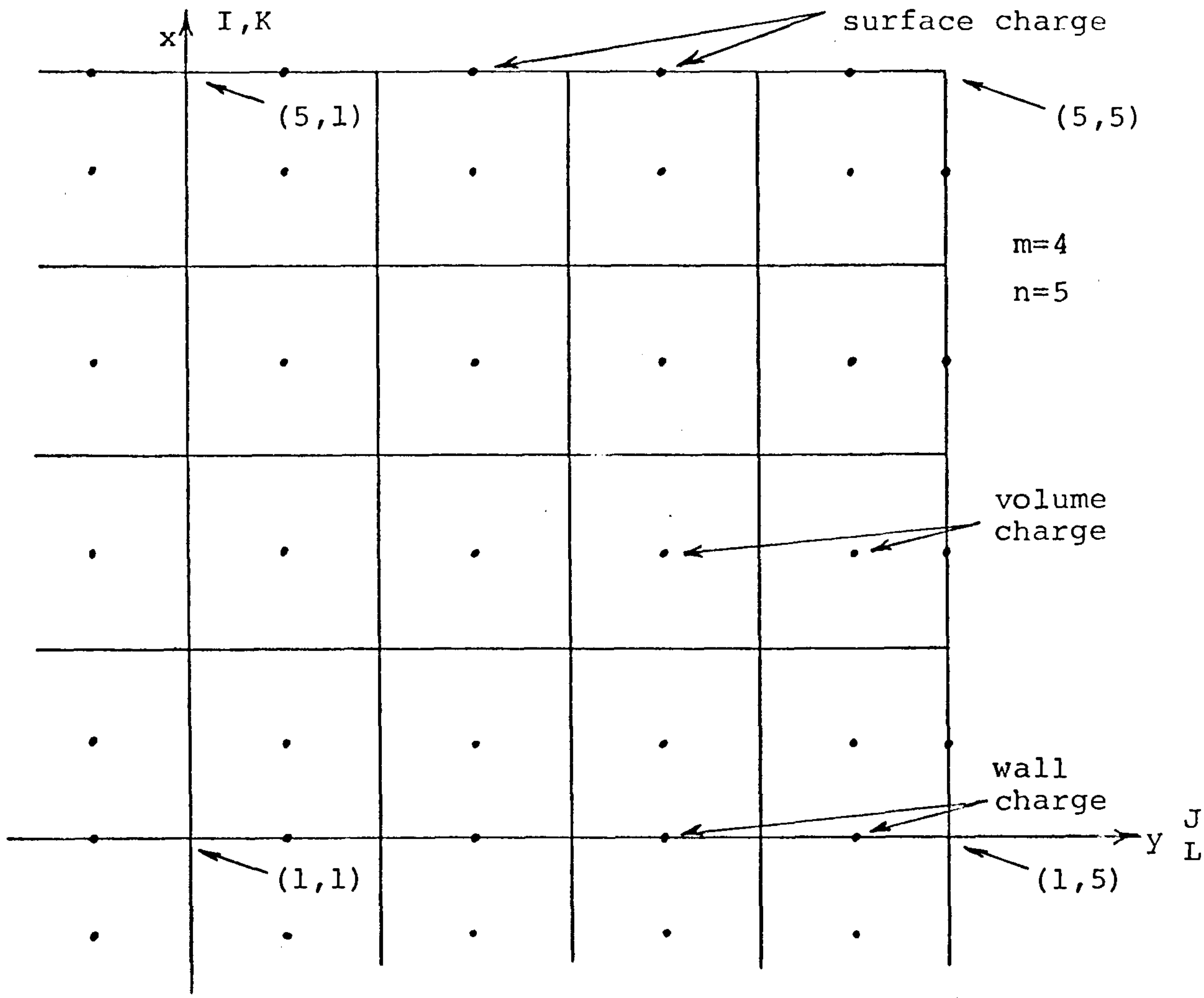

The field is evaluated at grid intersections

$$x = \frac{I-1}{m} \quad , \qquad I = 1, \ldots m+1 = n$$

$$y = \frac{J-1}{m} \quad , \qquad J = 1, \ldots n \; .$$

The volume charge is placed at the center of each grid square, at

$$x' = \frac{K-.5}{m} \qquad K = 1, \ldots m$$

$$y' = \frac{L-.5}{m} \qquad L = 1, \ldots m .$$

It is calculated by a linear interpolation:

$$-\frac{\partial \Phi_x}{\partial x'}\left(\frac{K-.5}{m}, \frac{L-.5}{m}\right) = -\frac{m}{2}\Big[\Phi_x(K+1, L+1)+\Phi_x(K+1, L)$$

$$-\Phi_x(K, L+1) - \Phi_x(K, L)\Big], \qquad K, L = 1, \ldots m$$

and

$$-\frac{\partial \Phi_y}{\partial y'}\left(\frac{K-.5}{m}, \frac{L-.5}{m}\right) = -\frac{m}{2}\Big[\Phi_y(K+1, L+1)+\Phi_y(K, L+1)$$

$$-\Phi_y(K+1, L) - \Phi_y(K, L)\Big], \qquad K, L = 1, \ldots m .$$

When the dimensionless integrals are converted to sums, all factors of m must cancel. The RHS of the (I,J) th equation of (A3.1) becomes finally

$$-\sum_{K=1}^{m}\sum_{L=1}^{m}\Big[K_x(I-K-.5, J-L-.5) + K_x(I-K-.5, J+L-1.5)$$

$$+ K_x(I+K-1.5, J+L-.5) + K_x(I+K-1.5, J+L-1.5)\Big] \times$$

$$\tfrac{1}{2}\Big[\Phi_x(K+1, L+1) + \Phi_x(K+1, L) - \Phi_x(K, L+1)$$

$$- \Phi_x(K, L) + \Phi_y(K+1, L+1) + \Phi_y(K, L+1)$$

$$- \Phi_y(K+1, L) - \Phi_y(K, L)\Big] . \tag{A3.2}$$

As before, for any numbers Δx and Δy,

$$K_x(\Delta x,\ \Delta y) = \frac{2\Delta x}{(\Delta x)^2+(\Delta y)^2}$$

and

$$K_y(\Delta x,\ \Delta y) = \frac{2\Delta y}{(\Delta x)^2+(\Delta y)^2}\ .$$

There are n^2 of these x-fields (at grid intersections) and n^2 similar equations for the y-fields where K_x is replaced by K_y.

The second term in (4.3a) gives the x-field at (x,y) due to charges on the wall; we rewrite it as

$$2\int_0^1 dy'\left[K_x(x,\ y-y') + K_x(x,\ y+y')\right] \times \left[1-\Phi_x(0,y')\right]$$

$$= 2\sum_{L=1}^{m}\left[K_x(I-1,\ J-L-.5) + K_x(I-1,\ J+L-1.5)\right]\times$$

$$\left[1-\tfrac{1}{2}(\Phi_x(1,\ L+1) + \Phi_x(1,L))\right], \qquad \text{(A3.3)}$$

where the charges are put at $(x',\ y') = (0,\ \frac{L-.5}{m})$. The magnitude of the wall or surface charge density in the center of a grid line is taken to be the average of the values at the ends of that line.

Similarly, the x-fields due to charge on surfaces parallel and perpendicular to the wall are, respectively,

$$\sum_{L=1}^{m}\left[K_x(I-1-m,\ J-L-.5) + K_x(I-1-m,\ J+L-1.5)\right.$$

$$\left. + K_x(I-1+m,\ J-L-.5) + K_x(I-1+m,\ J+L-1.5)\right]\times$$

$$\tfrac{1}{2}\left[\Phi_x(n,\ L+1) + \Phi_x(n,L)\right] \qquad \text{(A3.4)}$$

and

$$\sum_{K=1}^{m} \left[K_x(I-K-.5,\ J-1-m) + K_x(I+K-1.5,\ J-1-m)\right.$$

$$\left. + K_x(I-K-.5,\ J-1+m) + K_x(I+K-1.5,\ J-1+m)\right] \times$$

$$\tfrac{1}{2}\left[\Phi_y(K+1,n) + \Phi_y(K,n)\right]. \qquad (A3.5)$$

This procedure gives a good approximation to the fields at all points <u>except</u> for the perpendicular field at the wall or surface due to charges on that surface. The charges are concentrated in lines on this surface and give no perpendicular fields at the field points on the same surface. So at the wall, we add to the x-field

$$2\pi\sigma(L) = M_s\theta \cdot 4\pi\left[1-\Phi_x(1,L)\right], \qquad L = 1, \ldots.\ n.$$

Similar additions are made for the surface fields.

The $2n^2$ unknown angles are taken to be a vector $\underset{\sim}{\Phi}$ where

$$\Phi\left[(K-1)n + L\right] = \Phi_x(K,L)$$

$$\Phi\left[n^2+(K-1)n + L\right] = \Phi_y(K,L)$$

Equations (4.3) are replaced by

$$4\pi R\underset{\approx}{I}\underset{\sim}{\Phi} = \underset{\approx}{C}\underset{\sim}{\Phi} - \underset{\sim}{P}$$

where $\underset{\approx}{I}$ is the identity matrix, $\underset{\approx}{C}$ is a $2n^2 \times 2n^2$ matrix, and $\underset{\sim}{P}$ is a vector. In $C(A,B)$, the variable A indexes the equation (field point) and B indexes the source.

$$M_s\theta\ C(A,B)\Phi(B)$$

is the demagnetizing field at A due to sources (both volume and surface) near B and proportional to $\Phi(B)$. The equations are inhomogeneous, and the vector $P(A)$ essentially gives the field at A due to the term in the wall charge proportional to θ.

The contribution to $C(A,B)$ from volume charges is found in (A3.2), from wall charges in (A3.3), and from surface charges in (A3.4). The x-fields are found for $A = 1, \ldots n^2$; the y-fields for $A = n^2 + 1, \ldots 2n^2$, where again K_x is replaced by K_y. The Fortran G program follows. 242 simultaneous equations were solved ($m = 10$) for the transverse magnetization.

```
      IMPLICIT REAL*8 (A-H,O-Z)
      DIMENSION PHI(242),C(242,242)
      DIMENSION RHOX(10,10),RHOY(10,10),RHO(10,10)
      DIMENSION SIGW(10),SIGT(10),SIGS(10)
  220 FORMAT('0',(10F12.7))
  230 FORMAT('0',(11F11.6))
      M=10
      R=5.D2/1.7D3
      WRITE(6,15)R
   15 FORMAT('1','ANISOTROPY FIELD/MAGNETIZATION=',F20.6)
      RM=M
      N=M+1
      NS=N*N
      NS1=NS+1
      NST=2*N*N
      ZERO=0.D0
      HALF=.5D0
      ONE=1.D0
      THALF=1.5D0
      TWO=2.D0
      FOUR=4.D0
      PI=3.1415926535D0
      TWOPI=TWO*PI
      FOURPI=FOUR*PI
      DO 6 I=1,NST
      DO 5 J=1,NST
      C(I,J)=ZERO
    5 CONTINUE
    6 CONTINUE
      DO 110 I=1,N
      DO 100 J=1,N
      IA=N*(I-1)+J
      DO 20 K=1,M
      DO 10 L=1,M
      DA=I-K-HALF
      DAS=DA*DA
      DB=J-L-HALF
      DBS=DB*DB
      DC=I+K-THALF
      DCS=DC*DC
      DD=J+L-THALF
      DDS=DD*DD
      F=DA/(DAS+DBS)+DA/(DAS+DDS)+DC/(DCS+DBS)+DC/(DCS+DDS)
      FA=DB/(DAS+DBS)+DD/(DAS+DDS)+DB/(DCS+DBS)+DD/(DCS+DDS)
      IBA=K*N+L+1
      IBB=K*N+L
      IBC=(K-1)*N+L+1
      IBD=(K-1)*N+L
      C(IA,IBA)=C(IA,IBA)-F
      C(IA,IBB)=C(IA,IBB)-F
      C(IA,IBC)=C(IA,IBC)+F
      C(IA,IBD)=C(IA,IBD)+F
```

```
      C(IA,NS+IBA)=C(IA,NS+IBA)-F
      C(IA,NS+IBB)=C(IA,NS+IBB)+F
      C(IA,NS+IBC)=C(IA,NS+IBC)-F
      C(IA,NS+IBD)=C(IA,NS+IBD)+F
      C(NS+IA,IBA)=C(NS+IA,IBA)-FA
      C(NS+IA,IBB)=C(NS+IA,IBB)-FA
      C(NS+IA,IBC)=C(NS+IA,IBC)+FA
      C(NS+IA,IBD)=C(NS+IA,IBD)+FA
      C(NS+IA,NS+IBA)=C(NS+IA,NS+IBA)-FA
      C(NS+IA,NS+IBB)=C(NS+IA,NS+IBB)+FA
      C(NS+IA,NS+IBC)=C(NS+IA,NS+IBC)-FA
      C(NS+IA,NS+IBD)=C(NS+IA,NS+IBD)+FA
   10 CONTINUE
   20 CONTINUE
      PHI(IA)=ZERO
      PHI(NS+IA)=ZERO
      DO 30 L=1,M
      DA=I-1
      DAS=DA*DA
      DB=J-L-HALF
      DBS=DB*DB
      DC=J+L-THALF
      DCS=DC*DC
      F=DA/(DAS+DBS)+DA/(DAS+DCS)
      PHI(IA)=PHI(IA)-FOUR*F
      C(IA,L+1)=C(IA,L+1)-TWO*F
      C(IA,L)=C(IA,L)-TWO*F
      FA=DB/(DAS+DBS)+DC/(DAS+DCS)
      PHI(NS+IA)=PHI(NS+IA)-FOUR*FA
      C(NS+IA,L+1)=C(NS+IA,L+1)-TWO*FA
      C(NS+IA,L)=C(NS+IA,L)-TWO*FA
   30 CONTINUE
      DO 40 L=1,M
      DA=I-1-M
      DAS=DA*DA
      DB=J-L-HALF
      DBS=DB*DB
      DC=I-1+M
      DCS=DC*DC
      DD=J+L-THALF
      DDS=DD*DD
      F=DA/(DAS+DBS)+DA/(DAS+DDS)+DC/(DCS+DBS)+DC/(DCS+DDS)
      IBA=N*M+L+1
      IBB=N*M+L
      C(IA,IBA)=C(IA,IBA)+F
      C(IA,IBB)=C(IA,IBB)+F
      FA=DB/(DAS+DBS)+DD/(DAS+DDS)+DB/(DCS+DBS)+DD/(DCS+DDS)
      C(NS+IA,IBA)=C(NS+IA,IBA)+FA
      C(NS+IA,IBB)=C(NS+IA,IBB)+FA
   40 CONTINUE
      DO 50 K=1,M
      DA=I-K-HALF
```

```
      DAS=DA*DA
      DB=J-1-M
      DBS=DB*DB
      DC=I+K-THALF
      DCS=DC*DC
      DD=J-1+M
      DDS=DD*DD
      F=DA/(DAS+DBS)+DC/(DCS+DBS)+DA/(DAS+DDS)+DC/(DCS+DDS)
      IBA=NS+K*N+N
      IBB=NS+(K-1)*N+N
      C(IA,IBA)=C(IA,IBA)+F
      C(IA,IBB)=C(IA,IBB)+F
      FA=DB/(DAS+DBS)+DB/(DCS+DBS)+DD/(DAS+DDS)+DD/(DCS+DDS)
      C(NS+IA,IBA)=C(NS+IA,IBA)+FA
      C(NS+IA,IBB)=C(NS+IA,IBB)+FA
   50 CONTINUE
  100 CONTINUE
  110 CONTINUE
      DO 120 L=1,M
      PHI(L)=PHI(L)-FOURPI
      C(L,L)=C(L,L)-FOURPI
  120 CONTINUE
      PHI(N)=PHI(N)-FOURPI
      C(N,N)=C(N,N)-FOURPI
      DO 130 L=1,M
      IA=N*M+L
      C(IA,IA)=C(IA,IA)-TWOPI
  130 CONTINUE
      C(NS,NS)=C(NS,NS)-TWOPI
      DO 140 K=1,M
      IA=NS+K*N
      C(IA,IA)=C(IA,IA)-TWOPI
  140 CONTINUE
      C(NST,NST)=C(NST,NST)-TWOPI
      DO 150 I=1,NST
  150 C(I,I)=C(I,I)-R
      CALL DSIMEQ(NST,C,PHI,NST)
      WRITE(6,35)
   35 FORMAT('0',10X,'X AND Y ANGLES')
      WRITE(6,230)(PHI(I),I=1,NS)
      WRITE(6,230)(PHI(I),I=NS1,NST)
      RHOAV=ZERO
      DO 170 K=1,M
      DO 160 L=1,M
      IBA=K*N+L+1
      IBB=K*N+L
      IBC=(K-1)*N+L+1
      IBD=(K-1)*N+L
      RHOX(K,L)=-(RM/TWO)*(PHI(IBA)+PHI(IBB)-PHI(IBC)-PHI(IBD))
      RHOY(K,L)=-(RM/TWO)*(PHI(NS+IBA)+PHI(NS+IBC)
     1-PHI(NS+IBB)-PHI(NS+IBD))
      RHO(K,L)=RHOX(K,L)+RHOY(K,L)
```

```
      RHOAV=RHOAV+RHO(K,L)
  160 CONTINUE
  170 CONTINUE
      RHOAV=RHOAV/(RM*RM)
      WRITE(6,36)
   36 FORMAT(///10X,'VOLUME CHARGE DENSITIES: X,Y,TOTAL')
      WRITE(6,220)((RHOX(K,L),L=1,M),K=1,M)
      WRITE(6,220)((RHOY(K,L),L=1,M),K=1,M)
      WRITE(6,220)((RHO(K,L),L=1,M),K=1,M)
      WRITE(6,25)RHOAV
   25 FORMAT('0','AVERAGE VOLUME DENSITY=',F16.8)
      SIGWAV=ZERO
      DO 180 L=1,M
      SIGW(L)=ONE-HALF*(PHI(L+1)+PHI(L))
      SIGWAV=SIGWAV+SIGW(L)/RM
  180 CONTINUE
      SIGTAV=ZERO
      DO 190 L=1,M
      IBA=N*M+L+1
      IBB=N*M+L
      SIGT(L)=HALF*(PHI(IBA)+PHI(IBB))
      SIGTAV=SIGTAV+SIGT(L)/RM
  190 CONTINUE
      SIGSAV=ZERO
      DO 200 K=1,M
      IBA=NS+(K+1)*N
      IBB=NS+K*N
      SIGS(K)=HALF*(PHI(IBA)+PHI(IBB))
      SIGSAV=SIGSAV+SIGS(K)/RM
  200 CONTINUE
      WRITE(6,220)SIGW
      WRITE(6,26)SIGWAV
   26 FORMAT(1X,'AVERAGE WALL CHARGE=',F16.8)
      WRITE(6,220)SIGT
      WRITE(6,27)SIGTAV
   27 FORMAT(1X,'AVERAGE TOP SURFACE CHARGE=',F16.8)
      WRITE(6,220)SIGS
      WRITE(6,28)SIGSAV
   28 FORMAT(1X,'AVERAGE SIDE SURFACE CHARGE=',F16.8)
      END
```

APPENDIX 4

CALCULATION OF SURFACE CHARGE ASSUMING $\vec{\nabla}\cdot\vec{M} = 0$

```
      IMPLICIT REAL*8 (A-H,O-Z)
      DIMENSION PHI(202),C(202,202),SIGT(100),SIGS(100)
  310 FORMAT(/(10F12.7))
  320 FORMAT(/(10F12.7))
      M=100
      DO 400 IR=1,5
      RIR=IR
      R=5.D2/1.7D3
      R=R*(1.D1**(RIR-3.D0))
      N=M+1
      N1=N+1
      NT=2*N
      NTMI=NT-1
      RM=M
      MMI= M-1
      ZERO=0.D0
      ONE=1.D0
      THALF=1.5D0
      HALF=.5D0
      TWO=2.D0
      PI=3.1415926535D0
      TWOPI=TWO*PI
      FOUR=4.D0
      FOURPI=FOUR*PI
      PHIW=ONE/(ONE+R/FOURPI)
      SIGW=TWO*(ONE-PHIW)
      WRITE(6,5)R
    5 FORMAT('1','ANISOTROPY FIELD/MAGNETIZATION=',F20.8)
      DO 10 I=1,NT
      PHI(I)=ZERO
      DO 10 J=1,NT
   10 C(I,J)=ZERO
      DO 100 J=1,N
      DO 30 L=1,M
      DA=M
      DAS=DA*DA
      DB=J-L-HALF
      DBS=DB*DB
      DC=J+L-THALF
      DCS=DC*DC
      F=TWO*DA/(DAS+DBS)+TWO*DA/(DAS+DCS)
      PHI(J)=PHI(J)-SIGW*F
   30 CONTINUE
      DO 40 L=1,M
      DA=TWO*RM
      DAS=DA*DA
      DB=J-L-HALF
      DBS=DB *DB
```

```
      DC=J+L-THALF
      DCS=DC*DC
      F=DA/(DAS+DBS)+DA/(DAS+DCS)
      C(J,L+1)=C(J,L+1)+F
      C(J,L) = C(J,L)+F
   40 CONTINUE
      DO 50 K=1,M
      DA=M-K+HALF
      DAS=DA*DA
      DB=J-1-M
      DBS=DB*DB
      DC=M+K-HALF
      DCS=DC*DC
      DD=J-1+M
      DDS=DD*DD
      F=DA/(DAS+DBS)+DC/(DCS+DBS)+DA/(DAS+DDS)+DC/(DCS+DDS)
      C(J,N+K+1)=C(J,N+K+1)+F
      C(J,N+K)=C(J,N+K)+F
   50 CONTINUE
  100 CONTINUE
      DO 200 I=1,N
      DO 110 L=1,M
      DA=I-1
      DAS=DA*DA
      DB=M-L+HALF
      DBS=DB*DB
      DC=M+L-HALF
      DCS=DC*DC
      F=TWO*DB/(DAS+DBS)+TWO*DC/(DAS+DCS)
      PHI(N+I)=PHI(N+I)-SIGW*F
  110 CONTINUE
      DO 120 L=1,M
      DA=I-1-M
      DAS=DA*DA
      DB=M-L+HALF
      DBS=DB*DB
      DC=I-1+M
      DCS=DC*DC
      DD=M+L-HALF
      DDS=DD*DD
      F=DB/(DAS+DBS)+DD/(DAS+DDS)+DB/(DCS+DBS)+DD/(DCS+DDS)
      C(N+I,L+1)=C(N+I,L+1)+F
      C(N+I,L)=C(N+I,L)+F
  120 CONTINUE
      DO 130 K=1,M
      DA=I-K-HALF
      DAS=DA*DA
      DB=TWO*RM
      DBS=DB*DB
      DC=I+K-THALF
      DCS=DC*DC
      F=DB/(DAS+DBS)+DB/(DCS+DBS)
      C(N+I,N+K+1)=C(N+I,N+K+1)+F
      C(N+I,N+K)=C(N+I,N+K)+F
```

```
130 CONTINUE
200 CONTINUE
    DO 210 I=1,NT
210 C(I,I)=C(I,I)-TWOPI
    DO 217 I=1,NT
217 C(I,I)=C(I,I)-R
    NEQ=1
    WRITE(6,45)NEQ
 45 FORMAT('0','EQUATION REPLACED IS',I10)
    PHI(NEQ)=RM*PHIW
    C(NEQ,1)=HALF
    C(NEQ,N)=HALF
    C(NEQ,N+1)=HALF
    C(NEQ,NT)=HALF
    DO 15 I=1,MMI
    C(NEQ,I+1)=ONE
    C(NEQ,N+I+1)=ONE
 15 CONTINUE
    CALL DSIMEQ(NT,C,PHI,NT)
    WRITE(6,310)(PHI(I),I=1,N)
    WRITE(6,310)(PHI(I),I=N1,NT)
    SIGTAV=ZERO
    SIGSAV=ZERO
    DO 220 I=1,M
    SIGT(I)=HALF*(PHI(I+1)+PHI(I))
    SIGTAV=SIGTAV+SIGT(I)/RM
    SIGS(I)=HALF*(PHI(N+I+1)+PHI(N+I))
    SIGSAV=SIGSAV+SIGS(I)/RM
220 CONTINUE
    SIGT(1)=SIGT(2)
    WRITE(6,320)SIGT
    WRITE(6,17)SIGTAV
 17 FORMAT(1X,'FRACTION OF CHARGE ON TOP=',F20.7)
    WRITE(6,320)SIGS
    WRITE(6,18)SIGSAV
 18 FORMAT(1X,'FRACTION OF CHARGE ON SIDE=',F20.7)
    SIGW=HALF*SIGW
    WRITE(6,19)SIGW
 19 FORMAT('0','FRACTION OF CHARGE ON WALL=',F20.7)
400 CONTINUE
    STOP
    END
```

APPENDIX 5

CALCULATION OF LONGITUDINAL MAGNETIZATION

```
      IMPLICIT REAL*8 (A-H,O-Z)
      DIMENSION A(101,101),AMAG(101),AMAGN(101),AK(200),AL(200)
      DIMENSION B(101,101),F(101),G(101),SIGMA(101),HDEM(101)
      DIMENSION ADEM(101,101),HINT(101),BMAG(101)
      DIMENSION CMAGN(101),Z(101),ZSQ(101),ERROR(101)
      M=100
      L=M/10
      DO 400 K=1,5
      READ(5,450)R
  450 FORMAT(F6.5)
      FOURPI=4.D0*3.1415926535D0
      CHI=1.D20
      W=2.D0
      H=1.D0
C     CHI IS INTRINSIC SUSCEPTIBILITY
C     W IS RATIO OF COIL TO CYLINDER RADIUS
C     H IS APPLIED FIELD
      LP=L+1
      ML=M-L
      LMI=L-1
      MMI=M-1
      MTWO=2*M
      RM=M
      RW=R*W
      N=M+1
      RN=N
      ZERO=0.D0
      TWO=2.D0
      TWOPI=TWO*3.1415926535D0
      CHIME=TWO/(R*RM*CHI)
      WRITE(6,17)R,CHI
   17 FORMAT('1',' RHO=',F9.5,5X,'CHI=',D12.3)
C     FIND FIELDS FROM END CHARGES
      DO 100 I=1,N
      AIM=I-1
      AIM=AIM/RM
      SIGMA(I)=-H
      I1=M-I+1
      I2=M+I-1
      R1=I1
      R2=I2
      R3=(R1*R1+RM*RM*R*R)**.5D0
      R4=(R2*R2+RM*RM*R*R)**.5D0
      ADEM(I,N)=-TWOPI*(TWO-R1/R3-R2/R4)
      A(I,N)=ADEM(I,N)-1.D0/CHI
      B(I,N)=A(I,N)
  100 CONTINUE
```

```
C     FIND FIELDS FROM SIDE CHARGES
      DO 110 I=1,MTWO
      R1=I-M-.5D0
      R2=I-.5D0
      R3=(R1*R1+RM*RM*R*R)**1.5D0
      R4=(R2*R2+RM*RM*R*R)**1.5D0
      AK(I)=RM*R1/R3
      AL(I)=-RM*R2/R4
  110 CONTINUE
      DO 120 I=1,N
      DO 130 J=1,M
      MP=I-J+M
      MQ=I+J-1
      ADEM(I,J)=TWOPI*R*(AK(MP)+AL(MQ))
      A(I,J)=ADEM(I,J)
      B(I,J)=A(I,J)
  130 CONTINUE
  120 CONTINUE
      DO 105 I=1,M
      DO 107 J=1,M
      A(I,J)=ADEM(I,J)-CHIME
      B(I,J)=A(I,J)
  107 CONTINUE
  105 CONTINUE
      CALL DSIMEQ(N,A,SIGMA,N)
      WRITE(6,70)
   70 FORMAT('0',' Z          SIGMA(Z)           SIG. SLOPE        DEV
     1IATION')
      AZ=.5D0/RM
      WRITE(6,75)AZ,SIGMA(1)
   75 FORMAT(F6.3,F14.7)
C     FIND SECOND DERIVATIVE OF MAG. AND DEVIATION FROM CONSTANCY
      ENDSPR=ZERO
      DO 170 I=2,M
      AZ=I-.5D0
      AZ=AZ/RM
      SI=SIGMA(2)-SIGMA(1)
      SLOPE=(SIGMA(I)-SIGMA(I-1))/SI
      ALIN=RM*AZ*SI
      DEVAB=SIGMA(I)-ALIN
      DEV=DEVAB/ALIN
      ENDSPR=ENDSPR+DEVAB
      WRITE(6,76)AZ,SIGMA(I),SLOPE,DEV
   76 FORMAT(F6.3,F15.7,2D16.7)
  170 CONTINUE
      WRITE(6,85)SIGMA(N)
   85 FORMAT(' SIGMA(END)=',F14.7)
C     FIND MAGNETIZATION AND DEMAGNETIZING FACTORS
      AMAG(N)=SIGMA(N)
      DO 225 I=1,M
      AMAG(N-I)=AMAG(N+1-I)+(TWO/(R*RM))*SIGMA(N-I)
  225 CONTINUE
```

```
      DTWO=ZERO
      DO 227 I=1,N
      AMAGN(I)=AMAG(I)/AMAG(1)
      DTWO=DTWO+AMAG(I)
  227 CONTINUE
C     DO LEAST SQUARE FIT OF PARABOLA TO MAGNETIZATION
      S1=ZERO
      S2=ZERO
      S3=ZERO
      S4=ZERO
      S5=ZERO
C     OMIT LAST M/10 POINTS FROM FIT
      NFUDG=LP
      NRED=N-NFUDG
      RNRED=NRED
      DO 300 I=1,NRED
      Z(I)=I-1
      Z(I)=Z(I)/RM
      ZSQ(I)=Z(I)*Z(I)
      S1=S1+AMAGN(I)
      S2=S2+ZSQ(I)
      S3=S3+ZSQ(I)*ZSQ(I)
      S4=S4+ZSQ(I)*AMAGN(I)
  300 CONTINUE
      COB=(S4-S1*S2/RNRED)/(S2*S2/RNRED-S3)
      COA=(S1+COB*S2)/RNRED
      DO 305 I=1,NRED
      CMAGN(I)=COA-COB*ZSQ(I)
      ERROR(I)=AMAGN(I)-CMAGN(I)
      S5=S5+ERROR(I)*ERROR(I)
  305 CONTINUE
      NR=NRED+1
      DO 310 I=NR,N
      Z(I)=I-1
      Z(I)=Z(I)/RM
      ZSQ(I)=Z(I)*Z(I)
      CMAGN(I)=COA-COB*ZSQ(I)
      ERROR(I)=AMAGN(I)-CMAGN(I)
  310 CONTINUE
      RMSD=(S5/RNRED)**.5D0
      WRITE(6,224)
  224 FORMAT('0',' Z',10X,'M(Z)',16X,'M(Z)/M(0)',11X,
     2'CALC.M(Z)/M(0)',6X,'ERROR')
      DO 320 I=1,N
      WRITE(6,228)Z(I),AMAG(I),AMAGN(I),CMAGN(I),ERROR(I)
  228 FORMAT(F7.3,4F20.12)
  320 CONTINUE
      WRITE(6,230)COA,COB
  230 FORMAT('0','NORM.MAG(Z)=',F16.12,'-',F16.12,'Z*Z')
      WRITE(6,232)RMSD,NRED
```

```
  232 FORMAT('0','RMS DEVIATION=',D12.5,20X,'NO. OF PTS USED=',I3)
      DONE=(H/AMAG(1)-1.D0/CHI)/FOURPI
      DTWO=((H*RN)/DTWO-1.D0/CHI)/FOURPI
      WRITE(6,25)DONE
   25 FORMAT('0','BALLISTIC DEMAGNETIZING FACTOR=',D16.8)
      WRITE(6,26)DTWO
   26 FORMAT('0','MAGNETOMETRIC DEMAGNETIZING FACTOR=',D16.8)
      XYZ=AMAG(1)*R/1.13D0
      WRITE(6,620)XYZ
  620 FORMAT('0','M(0)*RHO/H(APPLIED)=',F18.8)
C     CHECK SELF-CONSISTENCY: FIND INTERNAL AND DEMAG. FIELDS
      WRITE(6,60)
   60 FORMAT('0','Z',15X,'H(END)',15X,'H(SIDES)',14X,'H(TOTAL)'
     2,14X,'H(INT)',15X,'M(Z)')
      DO 200 I=1,N
      AZ=I-1
      AZ=AZ/RM
      F(I)=ZERO
      G(I)=ADEM(I,N)*SIGMA(N)
      DO 210 J=1,M
      F(I)=F(I)+ADEM(I,J)*SIGMA(J)
  210 CONTINUE
      HDEM(I)=F(I)+G(I)
      HINT(I)=H+HDEM(I)
      BMAG(I)=CHI*HINT(I)
      WRITE(6,65)AZ,G(I),F(I),HDEM(I),HINT(I),BMAG(I)
   65 FORMAT(F7.4,5F20.13)
  200 CONTINUE
  400 CONTINUE
      END
```

REFERENCES

BOOKS

W.F. Brown, Jr., "Magnetostatic Principles in Ferromagnetism", 1962, North-Holland Publishing Co., Amsterdam, Holland.

W.F. Brown, Jr., "Micromagnetics", 1963, Interscience Pubs. (John Wiley and Sons, Inc., N.Y.).

S. Chikazumi, "Physics of Magnetism", 1964, John Wiley and Sons, Inc., N.Y.

H.B. Dwight, "Tables of Integrals and Other Mathematical Data", 1961, The MacMillan Co., N.Y.

REVIEW ARTICLES

Ah-62R A. Aharoni, "Theoretical Search for Domain Nucleation", Rev. Mod. Phys. 34, 227 (1962).

Ah-66R A. Aharoni, "Magnetization Curling", Phys. Stat. Sol. 16, 3 (1966).

Ah-71aR A. Aharoni, "Applications of Micromagnetics", CRC Critical Reviews in Solid State Sci. (1971).

Ah-71bR A. Aharoni, "Domain Walls and Micromagnetics", J. Phys. Paris, Suppl. C1, 32, 966 (1971).

Br-59R W.F. Brown, Jr., "Micromagnetics, Domains, and Resonance", J. Appl. Phys. 30, 62S (1959).

Br-70R W.F. Brown, Jr., "Micromagnetism", Recent Advances in Engineering Science, Vol. 5, Gordon and Breach Science Publishers, Inc., London (1970).

Ki-49R C. Kittel, "Physical Theory of Ferromagnetic Domains", Rev. Mod. Phys. 21, 541 (1949).

Ki-56R C. Kittel and J.K. Galt, "Ferromagnetic Domain Theory", Solid State Physics, 3, ed. F. Seitz and D. Turnbull, Academic Press, N.Y. (1956).

Sh -63R S. Shtrikman and D. Treves, "Micromagnetics", in Magnetism, 3, ed. G. Rado and H. Suhl, Academic Press, N.Y. (1963).

PAPERS

Ah -58 A. Aharoni and S. Shtrikman, "Magnetization Curve of the Infinite Cylinder", Phys. Rev. 109, 1522 (1958).

Ah -59 A. Aharoni, "Some Recent Developments in Micromagnetics at the Weizmann Institute of Science", J. Appl. Phys. 30, 70S (1959).

Ah-67 A. Aharoni, "Two-Dimensional Model for a Domain Wall", J. Appl. Phys. 38, 3196 (1967).

Ah -68 A. Aharoni, "Remarks on the Application of Micromagnetics to a Boundless Plate", IEEE Trans. Mag. 4, 720 (1968).

Ah -72 A. Aharoni, "Two-Dimensional Approximation to Bloch Walls in Magnetic Films", Phil. Mag. 25, 993 (1972).

Ar-71 A.S. Arrott, B. Heinrich, and D.S. Bloomberg, "Magnetization Processes and Eddy Currents in Iron Whiskers", AIP Conf. Proc. 5, 897 (1971).

Ar-72a A.S. Arrott, B. Heinrich, and D.S. Bloomberg, "Domain Configurations, Bloch Walls, and Magnetization Processes in Iron Whiskers from D.C. to 200 kHz. Theory and Experiment II", AIP Conf. Proc. (to be published).

Ar -72b A.S. Arrott, B. Heinrich, and J.E. Noakes, "The Role of Dipole-Dipole Interactions in the Critical Behaviour of Ferromagnetic Materials", AIP Conf. Proc. (to be published).

Ar-72c A.S. Arrott and J.E. Noakes (to be published).

Bo -42 R.M. Bozorth and D.M. Chapin, "Demagnetizing Factors of Rods", J. Appl. Physics 13, 320 (1942).

Br -40 W.F. Brown, Jr., "Theory of the Approach to Magnetic Saturation", Phys. Rev. 58, 736 (1940).

Br-57 W.F. Brown, Jr., "Criterion for Uniform Magnetization", Phys. Rev. 105, 1479 (1957).

Br -59 W.F. Brown, Jr., "Micromagnetics: Successor to Domain Theory?", J. Phys. Rad., 20, 101 (1959).

Br-60 W.F. Brown, Jr., "Single-Domain Particles: New Uses of Old Theorems", Am. J. Phys. 28, 542 (1960).

Br-61 W.F. Brown, Jr., "Rigorous Calculation of the Nucleation Field in a Ferromagnetic Film or Plate", Phys. Rev. 124, 1348 (1961).

Br-62 W.F. Brown, Jr., "Nucleation Fields of an Infinitely Long Square Ferromagnetic Prism", J. Appl. Phys. 33, 3026 (1962).

Br-64 W.F. Brown, Jr., "Some Magnetostatic and Micromagnetic Properties of the Infinite Rectangular Bar", J. Appl. Phys. 35, 2102 (1964).

Br-68 W.F. Brown, Jr., "The Fundamental Theorem of Fine-Ferromagnetic-Particle Theory", J. Appl. Phys. 39, 993 (1968).

Br-69 W.F. Brown, Jr., "The Fundamental Theorem of the Theory of Fine Ferromagnetic Particles", Annals N.Y. Acad. Sci. 147, 461 (1969).

Br-70 W.F. Brown, Jr., "A Critical Assessment of Hoffmann's Linear Theory of Ripple", IEEE Trans. Mag. 6, 121 (1970).

Co-57 R.V. Coleman and G. G. Scott, "Magnetic Domain Patterns on Single-Crystal Iron Whiskers", Phys. Rev. 107, 1276 (1957).

Co-58 R.V. Coleman and G.G. Scott, "Magnetic Domain Patterns on Iron Whiskers", J. Appl. Phys. 29, 526 (1958).

Co-72 J.A. Copeland, "Magnetization of Small Permalloy Circuit Elements", J. Appl. Phys. 43, 1905 (1972).

De-58a R.W. DeBlois and C.D. Graham, Jr., "Domain Observations on Iron Whiskers", J.Appl. Phys. 29, 528 (1958).

De-58b R.W. DeBlois and C.D. Graham, Jr., "Domain Observations on Iron Whiskers", J. Appl. Phys. 29, 931 (1958).

Fo-61 C.A. Fowler, Jr., E.M. Fryer and D. Treves, "Domain Structures in Iron Whiskers as Observed by the Kerr Method", J. Appl. Phys. 32, 296S (1961).

Fo-68 F. Forlani, N. Minnaja, and G. Sacchi, "Application of Micromagnetics to a Boundless Plate", IEEE Trans. Mag. 4, 70 (1968).

Fr-57 E.H. Frei, S. Shtrikman and D. Treves, "Critical Size and Nucleation Field of Ideal Ferromagnetic Particles", Phys. Rev. 106, 446 (1957).

Ge-66 R. Gemperle, "The Ferromagnetic Domain Structure of Thin Single-Crystal Fe Platelets in an External Field", Phys. Stat. Sol. 14, 121 (1966).

Ge-69 R. Gemperle and J. Kaczér, "Charged 90° Walls in Iron Platelets", Phys. Stat. Sol. 34, 255 (1969).

Ha-70 W. Hagedorn and H.H. Mende, "Bereichsanordnung und Magnetisierungskurve von Eisenwhiskern unter Berücksichtigung des entmagnetisierenden Feldes", Z. Angew Physik, 30, 68 (1970).

He-72 B. Heinrich and A.S. Arrott, "Domain Configurations, Bloch Walls, and Magnetization Processes in Iron Whiskers from D.C. to 200 kHz. Theory and Experiment I", Can. J. Phys. 50, 710 (1972).

Ho-68a H.Hoffmann, "Basic Equations of Micromagnetism", J. Appl. Phys. 39, 873 (1968).

Ho-68b H. Hoffmann, "Theory of Magnetization Ripple", IEEE Trans. Mag. 4, 32 (1968).

Hu-69 A. Hubert, "Stray-Field-Free Magnetization Configurations", Phys. Stat. Sol. 32, 519 (1969)

Hu-70 A. Hubert, "Stray-Field-Free and Related Domain Wall Configurations in Thin Magnetic Films (II)", Phys. Stat. Sol. 38, 699 (1970).

Jo-65 R.I. Joseph and E. Schlömann, "Demagnetizing Field in Nonellipsoidal Bodies", J. Appl. Phys. 36, 1579 (1965).

Jo-66 R.I. Joseph, "Ballistic Demagnetizing Factor in Uniformly Magnetized Cylinders", J. Appl. Phys. 37, 4639 (1966).

Ko-70 D.J. Kozakoff and F.O. Simons, Jr., "Three-Dimensional Nonlinear Magnetic Field Boundary Value Problem and Its Numerical Solution", IEEE Trans. Mag. 6, 828 (1970).

La-1899 C.G. Lamb, "On the Distribution of Magnetic Induction in a Long Iron Bar", Phil. Mag., London 48, 262 (1899).

La-35 L.D. Landau and E. Lifshitz, "On the Theory of the Dispersion of Magnetic Permeability in Ferromagnetic Bodies", pp. 101-114, Collected Papers of L.D. Landau, Gordon and Breach, N.Y., 1965.

La-69 A.E. LaBonte, "Two-Dimensional Bloch-Type Domain Walls in Ferromagnetic Films", J. Appl. Phys. 40, 2450 (1969).

Mi-70 N. Minnaja, "Micromagnetics at High Temperature", Phys. Rev. B 1, 1151 (1970).

Mu-67 M.W. Muller, "Domain Formation in a Ferromagnetic Plate", J. Appl. Phys. 38, 2413 (1967).

Ne-44a L. Néel, "Les Lois de l'Aimantation et de la Subdivision en Domaines Élémentaires d'un Monocristal de Fer", J. Phys. Radium 5, 241 (1944).

Ne-44b L. Néel, "Les Louis de l'aimantation et de la Subdivision en Domaines Élémentaires d'un Monocristal de Fer", J. Phys. Radium 5, 265 (1944).

Ne-47 L. Neel, "Le Champ Coercitif d'une Poudre Ferromagnétique Cubique à Grains Anisotropes", Compt. Rend. 224, 1550 (1947).

Ok-65 T. Okoshi, "Demagnetizing Factors of Rods and Tubes Computed from Analog Measurements", J. Appl. Phys. 36, 2382 (1965).

Os-45 J.A. Osborn, "Demagnetizing Factors of the General Ellipsoid", Phys. Rev. 67, 351 (1945).

Sc-57 G.G. Scott and R.V. Coleman, "Domain Changes During Longitudinal Magnetization of Iron Whiskers", J. Appl. Phys. 28, 1512 (1957).

Si-70 F.O. Simons, Jr., D.J. Kozakoff, and R.C. Harden, "Nonlinear Magnetic Field Solutions Based on a Vector Magnetic Potential", IEEE Trans. Mag. 6, 519 (1970).

St-35 F. Stäblein and H. Schlechtweg, "Über den Entmagnetisierungsfaktor zylindrischer Stäbe", Zeits. f. Physik 95, 630 (1935).

St-48 E.C. Stoner and E.P. Wohlfarth, "A Mechanism of Magnetic Hysteresis in Heterogeneous Alloys", Phil. Trans. Roy. Soc. London A 240, 599 (1948).

St-69 C.H. Stapper, Jr., "Micromagnetic Solutions for Ferromagnetic Spheres", J. Appl. Phys. 40, 798 (1969).

Wa-36 K. Warmuth, "Die Bestimmung des ballistischen Entmagnetisierungsfaktors mit dem magnetischen Spannungsmesser an Stäben von quadratischem Querschnitt", Arch. f. Elektrotech. 30, 761 (1936).

Wa-37 K. Warmuth, "Zur Darstellung des ballistischen Entmagnetisierungsfaktors zylindrischer Stäbe", Arch. f. Elektrotech. 31, 124 (1937).

Wa-39 K. Warmuth, "Über den ballistischen Entmagnetisierungsfaktor zylindrischer Stäbe", Arch. f. Elektrotech. 33, 747 (1939).

Wi-49 H.J. Williams and W. Shockley, "A Simple Domain Structure in an Iron Crystal Showing a Direct Correlation with the Magnetization", Phys. Rev. 75, 178 (1949).